Development of photocatalytic and photothermal steam reforming of methane

WIRYA SARWANA

Contents

Preface

Global warming is one of the main issue human beings faced today caused by the greenhouse gases in the atmosphere and methane is one of them. Although methane presents in a small portion in the atmosphere, its global warming potential (GWP), which is per mol, is 28 times higher than CO_2. To limit its concentration in the atmosphere and consider it as a carbon and hydrogen source, converting it becomes a valuable chemical feedstock such as carbon monoxide and hydrogen is highly desired, and a high-temperature steam reforming of methane (SRM) becomes an established method to do it. However, some parts of methane are burned to gain the heat to maintain the SRM reaction which limits the product yield. Moreover, the large consumption of methane as a fossil resource additionally produces CO_2, contributing the global warming. Therefore, a new clean method with renewable energy is highly desired for performing the SRM reaction and one of the promising methods is utilizing solar energy to perform the SRM reaction i.e. photocatalytic SRM and photothermal SRM. Photocatalytic is a room-temperature catalytic reaction promoted by photocatalyst and photoenergy, and photothermal is a high-temperature reaction that utilized almost the entire spectrum energy of solar light (Vis/NIR) by converting them to heat energy and performing a typical thermal catalytic process. In the present study, the author devoted his interest to developing photocatalytic and photothermal steam reforming of methane reactions. The research work was conducted at the Graduate school of Human and Environmental Studies, Kyoto University, Japan under Prof. Hisao Yoshida's supervision.

The author would like to express his gratitude to Prof. Hisao Yoshida for his guidance, patience, insightful comment, and fruitful discussion about the study. Prof. Hisao Yoshida is one of the author's inspirations to be a good lecturer in the future. The author would like to express his gratitude also to Dr. Akira Yamamoto, Assistant Professor, Kyoto University for his kind help in many experiments and XAFS measurement, fruitful discussion, sincere discussion, and comment to improve the quality of the research.

The author is also thankful to Mr. Tsutomu Kiyomura at the Institute of Chemical Research, Kyoto University for the TEM observations and insightful comments.

The author would like to appreciate and thankful to Prof. Setsuhisa Tanabe and Prof. Toshihiro Nakamura at the Graduate School of Human and Environmental Studies, and Prof. Kentaro Teramura at the Graduate School of Engineering, Kyoto University for the

evaluation of the doctoral dissertation and their insightful comments to improve this dissertation.

The author also expresses his appreciation to Prof. Tomoko Yoshida at Osaka City University for fruitful discussions and kind suggestions at the conference.

The author is also thankful to Dr. Akihiko Anzai for his support from the beginning of this research, teaching and assisting in performing several measurements and sincere discussions during this study.

The author expresses his best regards to Ms. Yuri Bonnitcha, secretary at Hisao Yoshida Laboratory for her help in the official affairs during the whole period of the author's stay in the laboratory and for her kind support for settling down at the beginning of life in Kyoto together with Ms. Ishii Tomoko.

The author is also grateful to his colleagues Ms. Nishino Yuko for her collaborative works and kind discussions, to Mr. Shimpei Naniwa, Mr. Surya Pratap Singh, Mr. Daichi Takami, Mr. Hamada Salem El-Naggar, and Mr. Hiroki Yasumura for their friendship and discussions, and to all Hisao Yoshida laboratory members for providing a good environment for studying and research.

The author also thanks his Indonesian friends Mr. Muhammad Fauzi, Mr. Sani Soleman, Mr. Panggea and his family, Mr. Eko Heru and his family, and Mr. Ardi Imawan and his family for providing kind help during tough life in Kyoto and creating a kind friendship.

The author also would like to express sincere thanks to his dearest parents, Mr. Muhammad Dahlan and Mrs. Hayatunnupus, and his sisters, Mrs. Pebrina Dahayanti and Ms. Novi Fathiaturrahma, for their support and understanding during his study in Kyoto.

Finally, the author would like to express great thanks to his beloved wife, Mrs. Eki Ruskartina for her warm heart and patience in accompanying the author during his study in Kyoto, and her understanding and hardworking to raise their lovely children, Maryam Salsabila Nadhifa, Umar Hadziq Abdullah, and Kholid Hadziq Abdullah.

Wirya Sarwana,

Kyoto, Japan

29th January 2023

1. General Introduction

1.1. Methane Conversion via Steam Reforming of Methane

Methane (CH_4) is the simplest hydrocarbon abundantly found on our planet. It can be found in natural gas (70–90% by volume), biogas (50–70% by volume), and under the seafloor trapped in the frozen ice as methane hydrates.[1–3] Due to its abundance, methane is considered a vital carbon and hydrogen source for chemical reactions. In the atmosphere, methane is one of the greenhouse gas, and its global warming potential (GWP), which is per mol, is 28 times higher than CO_2.[4] Therefore, methane conversion is crucial in the current state.

Although methane is not easily converted due to the high C–H bond energy (439.3 kJ mol^{-1}) and less reactivity,[5] several methods have been developed for methane conversion. Some of them are steam reforming of methane (SRM, Table 1.1 entry 1), dry reforming of methane (DRM, Table 1.1, entry 2), methane pyrolysis (Table 1.1, entry 3), non-oxidative coupling of methane (NOCM, Table 1.1, entry 4), oxidative coupling of methane (OCM, Table 1.1, entry 5), partial oxidation of methane (Table 1.1, entry 6), and total oxidation of methane or catalytic combustion (Table 1.1, entry 7). Most methane has been utilized to get the heat energy for household appliances, the power for transportation or the electric power, all of which are produced by combustion with oxygen.[2,6] On the other hand, methane has been industrially used as a chemical feedstock by steam reforming of methane (SRM) to be converted into many valuable chemicals.

As shown in Table 1.1, SRM reaction is unfortunately a highly endothermic reaction that needs tremendous heat energy input. Conventionally, methane combustion supplies heat for the required energy[7,8] and increases the temperature of the reactor for the SRM reaction. Considering methane as the hydrogen source, utilizing some parts of methane as the heat source would lower the H_2 yield. Moreover, the large consumption of methane as a fossil resource additionally produces CO_2, contributing the global warming. Therefore, a new clean method with renewable energy is highly desired

for performing the SRM reaction.

Table 1.1 Change of Gibbs energy for several methane reactions

Entry	Reaction	Chemical reaction	$\Delta G°$/kJ mol $^{-1}$
1	Steam reforming of methane (SRM)	$CH_4 + H_2O \rightarrow CO + 3H_2$	142
2	Dry reforming of methane (DRM)	$CH_4 + CO_2 \rightarrow 2CO + 2H_2$	204
3	Pyrolysis	$CH_4 \rightarrow C + 2H_2$	50.7
4	Non-oxidative coupling of methane (NOCM)	$CH_4 \rightarrow ½\ C_2H_6 + ½\ H_2$	34.3
5	Oxidative coupling of methane (OCM)	$CH_4 + ¼\ O_2 \rightarrow ½\ C_2H_6 + ½\ H_2O$	−80
		$CH_4 + ½\ O_2 \rightarrow ½\ C_2H_4 + H_2O$	−144
6	Partial oxidation of methane	$CH_4 + ½\ O_2 \rightarrow CO + 2H_2$	−86.5
7	Total oxidation of methane	$CH_4 + 2O_2 \rightarrow CO_2 + 2H_2O$	−801

Solar energy is one of the promising alternative energies to perform SRM reactions because it is abundant, free, and environmentally friendly. There are several ways to utilize solar energy to perform SRM reactions such as photocatalytic steam reforming of methane (PSRM) and photothermal steam reforming of methane (PTSRM) systems although the products distribution is not the same. Photocatalysis is a chemical reaction promoted by photocatalysts and photoenergy, which can proceed even under thermodynamically unfavorable conditions i.e., at room temperature. The drawbacks of high temperature thermocatalytic SRM, such as deactivation of the catalyst due to coke formation or segregation of the metal catalyst, are expected to be avoided in the PSRM system. As PSRM can perform even at room temperature, the expense would be

reduced for the heat-resistant reactor and system. However, enhancing the quantum efficiency and product yields in the photocatalysis system is still challenging. In addition, although the conventional thermocatalytic SRM can produce H_2 and CO, the current PSRM provides H_2 and CO_2 instead of CO, where the change of the product selectivity is also a remaining task. Thus, much research to improve the PSRM is still in progress. In parallel, the photothermal steam reforming of methane (PTSRM) is also an effective way to utilize almost the entire spectrum energy of solar light (Vis/NIR) by converting them to heat energy and performing a typical thermal catalytic process as mentioned later.

1.2. Solar Utilization for Steam Reforming of Methane

1.2.1. Photocatalytic Steam Reforming of Methane

Photocatalytic steam reforming of methane (PSRM) is a reaction that converts CH_4 and H_2O directly to H_2 and CO_2, even under mild conditions by utilizing light energy, although it is endergonic. Figure 1.1 shows a schematic illustration of the PSRM reaction.

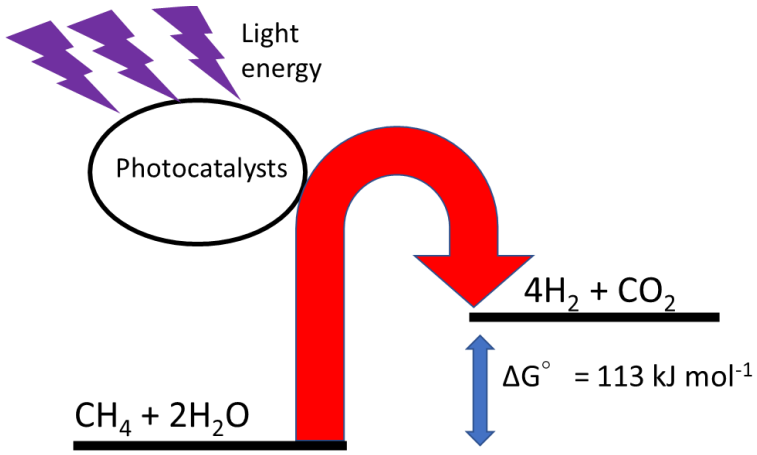

Figure 1.1 Schematic illustration of photocatalytic steam reforming of methane reaction

PSRM was firstly reported by Yoshida's group using Pt/TiO_2[9,10] (Table 1.2, entry 1) and a Pt-loaded La-doped $NaTaO_3$ photocatalyst ($Pt/NaTaO_3$:La).[9,11,12] The PSRM

mechanism over Pt/TiO_2 photocatalyst was proposed as shown in eq. 1 to eq. 6.[10] Briefly, as the UV light is absorbed by Pt/TiO_2 photocatalyst, the photocarriers, excited electrons and positive holes (h^+), are produced (eq. 1) in the photocatalyst. The holes on the TiO_2 surface of Pt/TiO_2 photocatalyst react with CH_4 and H_2O and produce $[CH_2O]_{n,ad}$, OH^-, and H^+ as intermediate species, where $[CH_2O]_{n,ad}$ express a surface intermediate matter consisting of CH_2O, and finally they give CO_2, H_2O and H^+ (eq. 2 – eq. 4) while on the deposited Pt nanoparticles, the two photoelectrons reduce two protons to form H_2 (eq. 5). In total, the PSRM is shown as eq. 6, where the carbon-containing product was CO_2 instead of CO.

$$Pt/TiO_2 + 8\ photons \rightarrow 8\ h^+ + 8e^- \quad (1)$$

$$CH_4 + H_2O + 4\ h^+ \rightarrow [CH_2O]_{n,ad} + 4H^+ \quad (2)$$

$$4H_2O \rightarrow 4OH^-_{ads} + 4H^+_{ads} \quad (3)$$

$$[CH_2O]_{n,ad} + 4OH^-_{ads} + 4\ h^+ \rightarrow CO_2 + 3H_2O \quad (4)$$

$$8H^+ + 8e^- \rightarrow 4H_2 \quad (5)$$

$$CH_4 + 2H_2O \rightarrow CO_2 + 4H_2 \quad (6)$$

After the first report of PSRM over Pt/TiO_2 and $Pt/NaTaO_3$:La photocatalysts, various photocatalysts have also been reported for the PSRM as shown in Table 1.2, such as $Pt/CaTiO_3$,[13,14] $Pt/\beta\text{-}Ga_2O_3$,[15–17] $Rh/K_2Ti_6O_{13}$,[18,19], La/TiO_2,[20] $Rh/Na_2Ti_6O_{13}$,[21] $Ag/SrTiO_3$,[22] and $Pt/CaTiO_3$:La.[23] Among these studies, it is demonstrated that doping with an appropriate amount of metal cations such as La^{3+} in $NaTaO_3$[11,12] and $CaTiO_3$[23] or Mg^{2+} or Zn^{2+} in Ga_2O_3[15,17] enhanced the photocatalytic activity in PSRM reaction. It was revealed that the dopants having a similar ionic radius and different valence compared to the photocatalyst's cation. i.e., La^{3+} with Na^+ and Mg^{2+} or Ca^{2+} with Ga^{3+} improved the n-or p-type properties of the semiconductor, respectively, without creating more defects in the crystal. It was also found that the morphology of the photocatalyst affected the photocatalytic activity. For example, the fine-structured crystal particles prepared by a flux method exhibited a higher H_2 production rate in PSRM than the

irregular shape particles prepared by a solid-state reaction over several photocatalysts such as $NaTaO_3$,[12] $Na_2Ti_6O_{13}$,[21] and $CaTiO_3$.[23] The loading metal on the photocatalyst and the loading method also affected the photocatalytic activity. Yoshida's group reported that the activity of $K_2Ti_6O_{13}$ photocatalyst in the PSRM reaction was enhanced drastically as Pt (loaded by either the impregnation or photodeposition method) or Rh (loaded by photodeposition method) was used as cocatalyst. The metal cocatalyst does not only enhance the activity but also changes even the product selectivity. The Rh cocatalyst loaded on the $K_2Ti_6O_{13}$ photocatalyst selectively produced H_2 and CO_2 in PSRM reaction while $Pt/K_2Ti_6O_{13}$ produced CO as a minor product along with the main products H_2 and CO_2.[19] On the other hand, Li and co-workers[24] reported that under UV light irradiation, an appropriate amount of Pt/TiO_2 photocatalyst produced H_2, CO_2, and C_2H_6, according to PSRM and photocatalytic NOCM (PNOCM) (Table 1.1, entry 4), where Pt cocatalyst provided active sites for H^+ reduction to H_2, and the TiO_2 surface provided methane radicals and successive coupling of two methyl radicals gave C_2H_6. Further, by utilizing Pt/Ga_2O_3 in flow gas-solid reaction system, Amano et al. improved the C_2H_6 selectivity up to 67% in PSRM.[25] These facts indicate that appropriate photocatalyst, metal cocatalyst, and reaction conditions would give specific products selectivity in PSRM.

Related to the PTSRM in the next session, the addition of thermal energy was found to be effective for enhancing the PSRM reaction. Elevation of temperature up to 334 K from 318 K (around room temperature) was effective in enhancing 10 % of photocatalytic activity over Pt loaded on Ga_2O_3 (Table 1.2, entry 5).[16] It was found that the thermal energy promoted the migration of the photoexcited electron from the inside of the photocatalyst crystal to the photocatalyst surface and the metal cocatalyst. On the other hand, Song et al. [26] reported that the PSRM activity of Rh/TiO_2 photocatalyst (Table 1.2, entry 13) in visible light was drastically enhanced as the temperature elevated to 573 K (not around room temperature), where the authors claimed that the thermal energy provided more efficient charge separation by promoting the migration of hot photoexcited electrons of Rh to the conduction band of TiO_2, resulting more $Rh^{\delta+}$ electron-deficient state at the surface and successively

activating the CH_4. By increasing the temperature up to 773 K, Han et al. demonstrated the enhancement of H_2 production rate in PSRM over Pt/Black TiO_2 photocatalyst under visible light irradiation and the quantum yield achieved almost 60 % (Table 1.2, entry 14).[27] These examples were investigated at high temperatures such as 573 K and 773 K. At such high temperature, we must consider the possibility that the precious metals such as Rh and Pt might act as conventional catalyst for SRM. This would be related the PTSRM systems mentioned in the next section.

Table 1.2 Representative reports on PSRM.

Entry	Photocatalyst used	Reaction condition	Product yields	Ref.
1	Pt(0.1)/TiO_2 Pt(0.1)/$NaTaO_3$:La(2)	300 W Xe lamp (UV=14 mW cm^{-1}), Fixed-bed flow reactor, Reactants: CH_4 (50%), H_2O (1.5%)	H_2 and CO_2 production rate was 0.76 and 0.18 µmol min^{-1} for Pt(0.1)/TiO_2 , and 1.5 and 0.39 µmol min^{-1} for Pt(0.1)/$NaTaO_3$:La	9
2	Pt(0.05)/$CaTiO_3$	300 W Xe lamp (230–280 nm = 14 mW cm^{-2} and 310–400 nm = 60 mW cm^{-1}), Fixed-bed flow reactor, Reactants: CH_4 (50%), H_2O (1.5%).	H_2 = 0.4 µmol min^{-1}	14
3	Pt(0.03)/$NaTaO_3$:La(2)	300 W Xe lamp (230–280 nm = 116 mW cm^{-2}), fixed-bed flow reactor,	H_2 and CO_2 production rate was 4.5 and 1.2 µmol min^{-1},	11

		1.0 g of catalyst, Reactants: CH_4 (50%), H_2O (1.5%).	respectively.	
4	Pt/In_2O_2(0.05)/β-Ga_2O_3:Mg(1)	300 W Xe lamp (230–280 nm = 14 mW cm^{-2} and 310–400 nm = 60 mW cm^{-2}), fixed-bed flow reactor, 0.8 g of catalyst, Reactants: CH_4 (50%), H_2O (1.5%).	H_2 production rate was 0.65 µmol min^{-1}	15
5	Pt(0.1)/ β-Ga_2O_3	300 W Xe lamp (230–280 nm = 14 mWcm^{-2} and 310–400 nm = 60 mW cm^{-2}), fixed-bed flow reactor, 0.8 g of catalyst, Reactants: CH_4 (50%), H_2O (1.5%).T=353 K	H_2 = ~0.67 µmol min^{-1}	16
6	Pt(0.05)/Ga_2O_3:Zn(HP, 0.5)	300 W Xe lamp (230–280 nm = 14 mWcm^{-2} and 310–400 nm = 60 mW cm^{-2}), fixed-bed flow reactor, 0.8 g of catalyst,	H_2 = 1.07 µmol min^{-1}	17

		Reactants: CH_4 (50%), H_2O (1.5%).		
7	Rh(0.03)/$K_2Ti_6O_{13}$ (prepared by a solid-state reaction)	300 W Xe lamp (254 ±10 nm = 14 mW cm^{-2} and 365 ±10 nm = 60 mW cm^{-1}), fixed-bed flow reactor, 0.8 g of catalyst, Reactants: CH_4 (50%), H_2O (1.5%).T=323 K	H_2 = 1.5 µmol min^{-1}	19
8	Pt(0.2)/$NaTaO_3$:La (1) (flux method)	300 W Xe lamp (254 ±10 nm = 14 mW cm^{-2}), fixed-bed flow reactor, 0.5 g of catalyst, Reactants: CH_4 (25%), H_2O (0.75%)	H_2 = 1.4 µmol min^{-1}	12
9	La(2.94)/TiO_2	300 W Hg lamp (252 nm = 150 mW cm^{-2}), fixed-bed flow reactor, 0.1 g of catalyst, Reactants: CH_4 (22.83%), H_2O (1.24%)	H_2 = 2.42 µmol min^{-1}	20
10	Rh(0.05)/$Na_2Ti_6O_{13}$	300 W Xe lamp (254 ±10 nm = 14	H_2 = 0.96 µmol min^{-1}	21

		mW cm^{-2}), fixed-bed flow reactor, 0.9 g of catalyst, Reactants: CH_4 (25%), H_2O (0.75%)		
11	Ag(0.5)/$SrTiO_3$	300 W Xe lamp, fixed-bed photoreactor, 0.1 g of catalyst, Reactants: CH_4 (1 mL), H_2O (10 mL)	H_2, CO, and CO_2 production rates was ~0.04, 0.007, and 0.02 µmol min^{-1}, respectively	22
12	Pt(0.5)/TiO_2	UV 4W/G4 T5 lamp (254 nm), flow reactor with inner-irradiation-type reaction vessel, 75 mg of catalyst, Reactants: CH_4 (10 mL min^{-1}), H_2O (75 mL). T=298 K	H_2, CO_2, C_2H_6, CO, and C_2H_4 production rate was 0.26, ~0.036, ~0.067, ~ 0.003 and ~ 0.003 µmol min^{-1}, respectively.	24
13	Pt/Ga_2O_3	40 W Hg lamp (254 nm = 33 or 15 mW cm^{-2}), flow gas-solid reactor, 50 mg of catalyst, Reactants: CH_4 (50%), H_2O (1.5%).T=298 K	H_2, CO_2, C_2H_6, and CO production rate was 3.05, 0.52, 0.58, and 0.07 µmol min^{-1}, respectively	25

14	Rh(2.0)/TiO_2	La-251 Xe lamp (420 < λ<800 nm = ~580 mW cm^{-2}), fixed-bed flow reactor, 20 mg of catalyst, Reactants: CH_4 (10%), H_2O (3%). T=573 K	H_2, CO, and CO_2 production rates was ~2.4, ~1.44, and ~0.02 µmol min^{-1}, respectively	26
15	Pt/Black TiO_2	Solar simulator AM 1.5 (λ> 420 nm), fixed-bed flow reactor, 15 mg of catalyst, Reactants flow: a water/CH_4 mixture gas (GHSV = 80 000 ml h^{-1} g^{-1}). T=773 K	H_2 and CO_2 production rates was ~46.67, and ~13.33 µmol min^{-1}, respectively	27

1.2.2. Photothermal Steam Reforming of Methane

Photothermal steam reforming of methane is similar to the traditional thermocatalytic SRM process (Table 1.1, entry 1), except concentrated solar light is used as the heat source rather than burning fossil fuel. This system typically consists of two main parts: a solar light collector/concentrator and a chemical reactor/reformer where the catalyst is put inside.[28] The reactor can be indirectly or directly heated by solar light.[29] Indirect heating system uses solar energy to heat the heat transfer fluid (HTF) such as molten salt or air and transfers the heat through a heat exchanger to the catalyst on which the reaction proceeds. On the other hand, direct heating is defined as the catalyst being directly heated by irradiation with concentrated light to promote the

reaction.

There are some reports about the indirectly heated system by concentrated solar light, and ASTERIX (Advanced Steam Reforming in Heat Exchanger) systems is an example of this system (Table 1.3, entry 1). In this system, the solar energy is collected and used for heating the air up to 1273 K.[30] The reaction proceeds as the reactants are flown into the reactor tube containing the packed catalyst bed while the hot air flew surrounding the reactor tube. It was reported that the CH_4 conversion was 91 % at 1073 K in steady state condition.[31] Yet, using air as HTF would lead to an uneconomic heat exchanger design to avoid the corrosion problem. Giaconia et al. proposed that the use of molten salt (mixture of $NaNO_3$/KNO_3) as HTF coupled with Pd membranes to enhance the H_2 production in indirectly heated solar SRM reaction at a lower temperature than conventional, i.e., < 823 K.[7,32,33] However, to maintain the stability of the molten salt, the PTSRM reaction in this system regulated to proceed under 823 K and as a consequence, CH_4 conversion was limited (Table 1.3, entry 2).

Oppositely, the direct heating system is relatively not restricted by the high-temperature reaction. For example, Berman et al. [34] reported that an Mn oxide-promoted Ru/Al_2O_3 catalyst (Table 1.3, entry 3) was used in a directly heated solar heating system and was stable for a long time reaction without catalyst deactivation at high temperature (506 h in 1373 K), where the Mn oxides improved the Ru dispersion and decreased the sintering rate of the catalyst. De Maria et al. reported that 10% Ni deposited on a 2–3 mm Al_2O_3 pellet was used as a catalyst for direct heating PTSRM and the CH_4 conversion achieved 80% of equilibrium at 1023 K (Table 1.3, entry 4).[35] Bo et al. reported that under concentrated solar light, the temperature of Ru/Al_2O_3 coated on SiC foam reached to1023 K and exhibited higher catalytic activity than Pd/Al_2O_3 and commercial ICI-46-6 catalyst (Ni-based)(Table 1.3, entry 5).[36]

Due to the stability problem of the catalyst in the high-temperature reaction, a low-temperature PTSRM reaction in a direct heating system has also been investigated. Li et al. reported that Ni metal supported on layered double hydroxide (LDH) nanosheets was active for H_2 production in PTSRM reaction under UV-Vis-NIR light (Table 1.3, entry

6). The LDH structure inhibited the coke formation and promoted the dispersion of metallic Ni.[37] Bimetallic metal catalyst also have been tested in a direct heating system. Wang et al. investigated the bimetal using a combination of Pd, Pt, Au, or Cu with Ni in a specific ratio and deposited on the LDH structure. It was found that bimetallic PdNi/LDH and PtNi/LDH were more active in PTSRM compared to single Ni/LDH. The existence of Pd enhanced the methane adsorption on the catalyst, thus enhancing the catalytic activity(Table 1.3, entry 7).[38]

Table 1.3 Representative reports of PTSRM reaction.

Entry	Catalyst	Type of heating	Reaction conditions	CH_4 conversion / Products yields	Ref.
1	Catalyst bed	Indirect	Light collector= solar tower, HTF = air, T_{max} = 1273 K, P =9.0 bars, T_{react} = 1073 K	H_2 = 51.0 %, CO = 10.4 %, CO_2 = 5.7 % CH_4 conv. = 91%	30,31
2	Ni-foam monolith	Indirect	Light collector = solar tower, HTF = solar salt ($NaNO_3$/KNO_3 mixture), T_{max} = 823 K, T_{react} = 817 K	CH_4 conv. = 60%	33
3	Ru/Al_2O_3 catalyst promoted with Mn oxides	Direct	T = 1373 K, catalyst = 20 mg, flow reactor, P=1 bar, S/C ratio = 2.1	CH_4 conv. = ~92%	34
4	Ni(10%)/Al_2O_3	Direct	Under solar light, T=1023 K, P = 1	H_2=73.7%, CO = 15.2%, CO_2 = 7.05%	35

			atm, S/C ratio=2.2		
5	Ru/Al_2O_3	Direct	Solar simulator (0.76-1.25 kW), T=1023 K, P = 1 atm, VHSV = 10,000 $cm^3 g_{cat}^{-1} h^{-1}$	CH_4 conv. = 90%	36
6	Ni/NiAl-12	Direct	300 W Xe lamp (UV-Vis-NIR), T= 671 K, P=0.14 MPa, catalyst =50 mg.	H_2 = 388.3 µmol g^{-1} min^{-1}	37
7	Pd/NiAl	Direct	300 W Xe lamp (UV-Vis = 1.77 W cm^{-1}), T = 573 K, P=0.2 MPa, catalyst = 20 mg.	H_2 = 82.9 mmol g^{-1} h^{-1}	38

Naturally, inhomogeneous temperature distribution would appear as the concentrated solar light heated the catalyst directly. The high-temperature zone would exist on the surface that obtained more intense focused light, and the low-temperature zone would be created on the surface that absorbed less light intensity. The temperature gradients are expected to affect the catalytic activity. Recently, Mao et al. reported that under light irradiation, the different temperature zone of Fe catalyst and $TiO_{2-x}H_y$ enhanced ammonia production beyond the equilibrium conversion in ammonia synthesis from nitrogen and hydrogen.[39] This would also be applicable to PTSRM.

1.3. Outline of the thesis

The present thesis focuses on developing photocatalytic and photothermal steam reforming of methane after this brief introduction presented here (Chapter 1).

In chapter 2, to obtain CO as a product in the room temperature PSRM, the lanthanum-doped sodium tantalate ($NaTaO_3$:La) prepared by a flux method were examined in different reaction conditions. It was found that the bare $NaTaO_3$:La photocatalyst produced H_2, CO, and CO_2 and the CO yield depended on the photocatalyst and the reaction conditions, such as light intensity, the flow rate of the reactants, and the methane/steam ratio. It was revealed that the photocatalytic water gas shift reaction, where CO was photocatalytically oxidized by H_2O to form H_2 and CO_2, took place as a successive reaction and decreased the CO yield in the PSRM system.

In chapter 3, to enhance the quantum efficiency and production rate of H_2, the rhodium-loaded potassium hexatitanate (Rh/$K_2Ti_6O_{13}$, Rh/KTO) prepared by a flux method was investigated in the PSRM reaction. Several parameters, such as the flux in the flux method, the flux concentration, the heating temperature, the holding time of the heating process, and the starting material, were varied to obtain the most active Rh/KTO photocatalyst. It was found that the fine Rh/KTO crystals with larger surface areas exhibited the highest H_2 production rate. Further, the granulated Rh/KTO sample was demonstrated to be more active than the powder one, suggesting interparticle transfer of photoexcited carriers proceeds due to the physical contact in the granule samples and enhanced photocatalytic activity.

In chapter 4, to investigate the inhomogeneous thermal distribution effect on the catalytic activity and product selectivity, various sizes of Ni nanoparticles on SiO_2 support, light power, and light spot size were examined in PTSRM reaction. It was found that the product selectivity obtained in the PTSRM system was different from that in a thermocatalytic SRM condition in the same CH_4 conversion due to successive reactions promoted in inhomogeneous thermal distribution conditions.

Finally, a general conclusion will be mentioned in chapter 5.

References

1 L. Yuliati and H. Yoshida, *Chem. Soc. Rev.*, 2008, **37**, 1592.

2 R. Horn and R. Schlögl, *Catal. Lett.*, 2015, **145**, 23–39.

3 C. D. Ruppel and J. D. Kessler, *Rev. Geophys.*, 2017, **55**, 126–168.

4 T. S. Foster K. Armour, W. Collins, J. L. Dufresne, D. Frame, D. J. Lunt, T. Mauritsen, M. D. Palmer, M. Watanabe, M. Wild, and H. Zhang, Cambridge University Press, Cambridge, United Kingdom and New York, NY, USA, 2021, pp. 923–1054.

5 P. Schwach, X. Pan and X. Bao, *Chem. Rev.*, 2017, **117**, 8497–8520.

6 J. Chen, H. Arandiyan, X. Gao and J. Li, *Catal. Surv. Asia*, 2015, **19**, 140–171.

7 A. Giaconia, M. de Falco, G. Caputo, R. Grena, P. Tarquini and L. Marrelli, *AIChE J.*, 2008, **54**, 1932–1944.

8 M. Tutar, C. E. Üstün, J. M. Campillo-Robles, R. Fuente, S. Cibrián, I. Arzua, A. Fernández and G. A. López, *Comput. Chem. Eng.*, 2021, **155**, 107504.

9 H. Yoshida, S. Kato, K. Hirao, J. Nishimoto and T. Hattori, *Chem. Lett.*, 2007, **36**, 430–431.

10 H. Yoshida, K. Hirao, J. Nishimoto, K. Shimura, S. Kato, H. Itoh and T. Hattori, *J. Phys. Chem. C*, 2008, **112**, 5542–5551.

11 K. Shimura, S. Kato, T. Yoshida, H. Itoh, T. Hattori and H. Yoshida, *J. Phys. Chem. C*, 2010, **114**, 3493–3503.

12 A. Yamamoto, S. Mizuba, Y. Saeki and H. Yoshida, *Appl. Catal. Gen.*, 2016, **521**, 125–132.

13 K. Shimura, H. Miyanaga and H. Yoshida, in *Studies in Surface Science and Catalysis*, eds. E. M. Gaigneaux, M. Devillers, S. Hermans, P. A. Jacobs, J. A. Martens and P. Ruiz, Elsevier, 2010, vol. 175, pp. 85–92.

14 K. Shimura and H. Yoshida, *Energy Environ. Sci.*, 2010, **3**, 615–617.

15 K. Shimura, T. Yoshida and H. Yoshida, *J. Phys. Chem. C*, 2010, **114**, 11466–11474.

16 K. Shimura, K. Maeda and H. Yoshida, *J. Phys. Chem. C*, 2011, **115**, 9041–9047.

17 K. Shimura and H. Yoshida, *Phys. Chem. Chem. Phys.*, 2012, **14**, 2678–2684.

18 K. Shimura, H. Kawai, T. Yoshida and H. Yoshida, *Chem. Commun.*, 2011, **47**, 8958–

8960.

19 K. Shimura, H. Kawai, T. Yoshida and H. Yoshida, *ACS Catal.*, 2012, **2**, 2126–2134.

20 B. V. Ayodele, A. A. Ghazali, M. Y. Mohd Yassin and S. Abdullah, *Int. J. Hydrog. Energy*, 2019, **44**, 20700–20710.

21 H. Yoshida, S. Mizuba and A. Yamamoto, *Catal. Today*, 2019, **334**, 30–36.

22 B. Tan, Y. Ye, Z. Huang, L. Ye, M. Ma and Y. Zhou, *Chin. Chem. Lett.*, 2020, **31**, 1530–1534.

23 A. Anzai, K. Fujiwara, A. Yamamoto and H. Yoshida, *Catal. Today*, 2020, **352**, 1–9.

24 L. Yu, Y. Shao and D. Li, *Appl. Catal. B Environ.*, 2017, **204**, 216–223.

25 F. Amano, C. Akamoto, M. Ishimaru, S. Inagaki and H. Yoshida, *Chem. Commun.*, 2020, **56**, 6348–6351.

26 H. Song, X. Meng, Z. Wang, Z. Wang, H. Chen, Y. Weng, F. Ichihara, M. Oshikiri, T. Kako and J. Ye, *ACS Catal.*, 2018, **8**, 7556–7565.

27 B. Han, W. Wei, M. Li, K. Sun and Y. H. Hu, *Chem. Commun.*, 2019, **55**, 7816–7819.

28 A. Steinfeld and A. Meier, in *Encyclopedia of Energy*, ed. C. J. Cleveland, Elsevier, New York, 2004, pp. 623–637.

29 E. J. Sheu, E. M. A. Mokheimer and A. F. Ghoniem, *Int. J. Hydrog. Energy*, 2015, **40**, 12929–12955.

30 M. Böhmer, U. Langnickel and M. Sanchez, *Sol. Energy Mater.*, 1991, **24**, 441–448.

31 M. Epstein, *SFERA Winter Sch. Switz. Zür.*

32 A. Giaconia, G. Iaquaniello, G. Caputo, B. Morico, A. Salladini, L. Turchetti, G. Monteleone, A. Giannini and E. Palo, *Int. J. Hydrog. Energy*, 2020, **45**, 33088–33101.

33 M. De Falco, G. Santoro, M. Capocelli, G. Caputo and A. Giaconia, *Int. J. Hydrog. Energy*, 2021, **46**, 10682–10696.

34 A. Berman, R. K. Karn and M. Epstein, *Green Chem.*, 2007, **9**, 626–631.

35 G. De Maria, C. A. Tiberio, L. D'Alessio, M. Piccirilli, E. Coffari and M. Paolucci, *Energy*, 1986, **11**, 805–810.

36 H. B. Do, J. T. Jang and G. Y. Han, *J. Sol. Energy Eng.*, 2012, **134**, 1–4.

37 T. Li, L. Tan, Y. Zhao and Y.-F. Song, *Chem. Eng. Sci.*, 2021, **245**, 116839.

38 P. Wang, X. Zhang, R. Shi, J. Zhao, Z. Yuan and T. Zhang, *Energy Fuels*, 2022, in press.

39 C. Mao, H. Li, H. Gu, J. Wang, Y. Zou, G. Qi, J. Xu, F. Deng, W. Shen, J. Li, S. Liu, J. Zhao and L. Zhang, *Chem*, 2019, **5**, 2702–2717.

2. Carbon monoxide formation as an intermediate product in photocatalytic steam reforming of methane with lanthanum-doped sodium tantalate

Abstract

Photocatalytic steam reforming of methane (PSRM) has been studied as an attractive method to produce hydrogen by utilizing photoenergy like solar energy around room temperature with metal-loaded photocatalysts, where methane and water are selectively converted to carbon dioxide and hydrogen. In the present study, the author examined to yield of the partially oxidized product, carbon monoxide (CO), in the PSRM system using a flow reactor around room temperature. It was found that some La-doped $NaTaO_3$ samples can produce carbon monoxide constantly in addition to hydrogen and carbon dioxide. Among the prepared samples, a La(2mol%)-doped $NaTaO_3$ photocatalyst without any cocatalyst gave the highest photocatalytic activity and the highest CO selectivity, such as 24%. The CO yield depended on the photocatalysts and the reaction conditions. Suitable reaction conditions for CO yield were high light intensity, higher flow rate, and moderately high methane/water ratio. Some additional reaction tests revealed that water gas shift (WGS) could take place as an undesired successive reaction, i.e., the produced carbon monoxide can successively react with water to form carbon dioxide, which would restrict the CO yield essentially.

2.1. Introduction

Methane (CH_4) is a ubiquitous substance obtained from underground and biomass. Considering it to be not a fuel but a carbon resource, the conversion of methane to other industrially valuable chemical compounds, such as carbon monoxide (CO) and hydrogen (H_2), is very attractive to be researched.[1–7] The mixture of CO and H_2 known as syngas could be catalytically obtained in steam reforming of methane (SRM, eq. 1). For the industrial production of hydrogen, successive water gas shift reaction of CO gives additional H_2 and CO_2 (WGS, eq.2) and the overall reaction gives hydrogen and CO_2 without CO production (eq. 3).

$$CH_4 + H_2O \rightarrow CO + 3\ H_2 \qquad \Delta G^{\circ}_{298K} = 142.1\ \mathrm{kJ\ mol^{-1}} \qquad (1)$$

$$CO + H_2O \rightarrow CO_2 + H_2 \qquad \Delta G^{\circ}_{298K} = -28.6\ \mathrm{kJ\ mol^{-1}} \qquad (2)$$

$$CH_4 + 2\ H_2O \rightarrow CO_2 + 4\ H_2 \qquad \Delta G^{\circ}_{298K} = 113.5\ \mathrm{kJ\ mol^{-1}} \qquad (3)$$

The highly endergonic reactions, except for the WGS, request a huge amount of energy consumption. Conventionally, methane combustion supplies heat for the required energy and thus, the reaction temperature increases, which represents several requirements such as inhibition of carbon deposition and an expensive heat-resistant reactor. Therefore, a new reaction system that can work at low temperatures is highly desirable for these endergonic reactions.

The photocatalytic reaction has shown a promising way to promote thermodynamically difficult reactions by utilizing solar light as photoenergy thus the reaction can occur even at room temperature. Photocatalytic steam reforming of methane (PSRM) can convert CH_4 and H_2O directly to H_2 and CO_2 (eq. 3) even under mild conditions, although it is endergonic.[8,9] This reaction was originally developed by Yoshida's group using a Pt-loaded TiO_2 (Pt/TiO_2) photocatalyst [10,11] and a Pt-loaded La-doped $NaTaO_3$ photocatalyst (Pt/$NaTaO_3$:La).[10,12,13] After that, various photocatalysts have also been reported for the PSRM such as Pt/$CaTiO_3$,[14,15] Pt/$CaTaO_3$:La,[16] Rh/$K_2Ti_6O_{13}$,[17,18] and Pt/β-Ga_2O_3.[19–21] These studies have focused only on hydrogen

production, where the observed molar ratio has been always H_2/CO_2=4 (eq. 3).

So far, photocatalytic conversion of methane and water has also been reported for the production of valuable chemicals such as methanol,[22–27] ethanol,[28] and aldehyde.[29] In the present study, the author attempted to change the selectivity of the PSRM to produce CO, which is one of the partially oxidized products from methane and very valuable as a chemical intermediate. In the previous study, it was found that the metal cocatalyst could change the product selectivity in PSRM. The Rh cocatalyst either loaded on $K_2Ti_6O_{13}$ or $NaTi_6O_{13}$ surface always gave H_2 and CO_2 selectively without any formation of CO.[18,30] In contrast, Pt loaded photocatalyst gave CO as a minor by-product with low selectivity such as 9–10% in $Pt/K_2Ti_6O_{13}$[18] and Pt/Ga_2O_3[31] photocatalysts. There has been, however, no report focusing the CO production in the PSRM.

Here, the author report the PSRM to produce CO by using a La-doped $NaTaO_3$ ($NaTaO_3$:La) photocatalyst without loading any cocatalysts, where the CO selectivity among the oxidative products reached to 24% for the first time. It is also revealed that the low CO selectivity is due to the successive oxidation to CO_2, in other words, CO is an intermediate product in the PSRM.

2.2. Experimental method

2.2.1. Catalyst preparation

Sodium tantalate ($NaTaO_3$, referred to as NTO) and lanthanum-doped sodium tantalate samples ($NaTaO_3$:La, referred to as NTO:La) were mainly prepared by a flux method. The starting materials, Na_2CO_3, Ta_2O_5 (Rare Metallic, 99.99%), and La_2O_3 (Kishida, 99.99%), were mixed together with a flux, NaCl (Kishida, 99.5%), in an alumina mortar for 15 min. The molar ratio for $NaTaO_3$:La was Na:Ta:La=100:100:*x*, where *x* was from 0 to 5, and the solute concentration in the molten mixture was 70%, i.e., the ratio was $NaTaO_3$:NaCl=70:30. The mixture was put in a platinum crucible and heated by using an electric muffle furnace, where the temperature was increased at 200 K h^{-1} from room temperature to 1273 K and hold for 5 h. It was cooled down at 100 K h^{-1} to 773 K

and naturally to ambient temperature in the furnace. The product obtained was washed with hot distilled water (353 K, 500 ml) for three times to remove the flux and then dried at 353 K overnight. These samples were referred to as NTO:La(*x*), where *x* is the amount of mol% La used as a dopant.

Another sample was prepared by a solid-state method in the same procedure mentioned above, only without using the NaCl flux. La-doping was 2 mol%. The starting materials were mixed, heated, and cooled, followed by washing in the same conditions as mentioned above. This sample was referred to as NTO:La(2)SS.

Some precious metals such as Au, Ag, Pd, and Pt and transition metals such as Ni, Cu, and Zn were loaded as cocatalysts on the NTO:La surface by an impregnation method. The precursor used for the loading process were $HAuCl_4 \cdot 6H_2O$, $AgNO_3$ (Kishida, 99.8%), $PdCl_2$ (Kishida, 99%), H_2PtCl_6 (Wako, 99.9%), $Ni(NO_3) \cdot 6H_2O$ (Wako, 99%), $Cu(NO_3)_2 \cdot 3H_2O$, and $Zn(NO_3)_2 \cdot 6H_2O$ (Nacalai Tesque, 99%). The NTO:La samples (2 g) were soaked and stirred in an aqueous solution of the precursor (100 ml; 0.05, 0.1 or 1 mM at 353 K until the water completely evaporated, and dried overnight in an oven at 353 K. Before using, metal loaded NTO:La was calcined at 673 K for 2 h. This was denoted as M(*y*)/NTO:La where *y* was wt% of metal cocatalyst. To investigate the role of La-doping, two additional La-loaded samples were also prepared. The precursor used for the loading process was $La(NO_3)_3.6H_2O$ (Nakalai Tesque, 99.9%). The La species of 0.3 wt% was loaded on the surface of the NTO and NTO:La(1) samples by the impregnation method, which were shown as La(0.3)/NTO and La(0.3)/NTO:La(1) samples.

Some photocatalysts such as Ga_2O_3 (Kojundo, 99.99%), ZnO (Kojundo, 99.99%), and TiO_2 (Ishihara Sangyo Kaisha, ST-01, 300 $m^2 g^{-1}$) were also employed for comparison. All of these photocatalysts were used as received without any pretreatment.

2.2.2. Characterization

X-ray diffraction (XRD) of the samples was recorded at room temperature using a Shimadzu Lab X XRD-6000. The radiation used was Cu Kα (40 kV, 30 mA). The crystallite size was determined by the Scherrer equation using full width at half maximum (FWHM) of the diffraction line at 2θ = 22.8° in the XRD pattern.

The images of scanning electron microscopy (SEM) were captured by a JEOL JSM-890. The diffuse reflectance (DR) UV-visible spectra were recorded by a JASCO V-670 equipped with an integrating sphere, where $BaSO_4$ was used as a reference. The band gap was estimated by using the Tauc plot.[32] The BET-specific surface area was measured by using adsorbed amount of N_2 on the sample surface at 77 K using a Quantachrome Monosorb MS-21.

2.2.3. Photocatalytic activity tests

Photocatalytic reaction tests for the PSRM were carried out using a fixed bed flow reactor, as shown in Figure 2.1.[13] The photocatalyst powder was pressed under 40 MPa for 1 min, which gave a pellet. The pellet obtained was crushed and sifted using 25-mesh and 50-mesh sieves. The remaining granules on the 50-mesh sieve were used for the reaction tests. The catalyst granules (1.2 g) were introduced inside a quartz reactor (60×20×1 mm^3), where the irradiated area of the photocatalyst was 6.0 cm^2. The feed gas mixture used for this reaction test consisted of typically CH_4 (25%) and H_2O (2.4 %) with argon as a carrier gas. The flow rate of the feed gas was 15 ml min^{-1}. A 300 W xenon lamp (PE300BUV) was used as a light source for photoirradiation without any optical filter. The light intensity was 165 mW cm^{-2} that was measured in the range of 254±10 nm in wavelength. The temperature of the reaction became 323 K due to the photoirradiation. The gas produced in the reaction was analyzed by on-line gas chromatography equipped with thermal conductivity detector (Shimadzu, GC-8A, TCD). The interval of sampling was ca. 30 min. Since the sensitivity of CO_2 in the

argon carrier gas was low, the experimental error for CO_2 determination was relatively large.

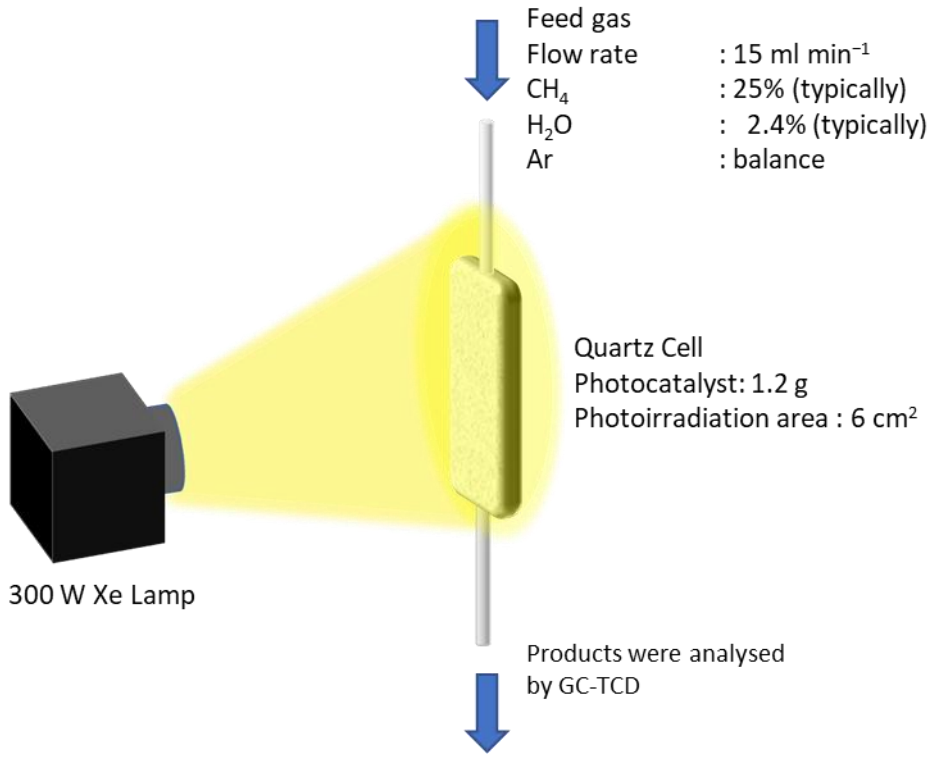

Figure 2.1 Scheme of the flow reactor employed in the photocatalytic reaction test for PSRM

2.3. Result and discussion

2.3.1. Characterization of photocatalysts

Figure 2.2 shows the SEM images of the non-doped NTO and various NTO:La samples prepared by the flux and solid-state reaction methods. The average particle sizes of these samples were estimated from these images and listed in Table 2.1. The non-doped NTO sample prepared by the flux method consisted of roundish cubic particles sized in the range of 0.2–2.5 µm (Figure 2.2a), where the average particle size was 0.8 µm (Table 2.1). The La-doped samples prepared by the flux method showed cubic crystals sized in the range of 0.04–1.0 µm (Figure 2.2b–e), which were much smaller than those of the non-doped NTO sample. This result confirmed that La-doping inhibited the crystal growth of $NaTaO_3$.[33–35] The NTO:La(1) sample showed the smallest

average particle size such as 0.21 µm. However, the NTO:La(5) sample with the higher La doping showed a little bit different morphology with a larger size, such as 0.55 µm (Figure 2.2e). As for the NTO:La(2)SS sample, the morphology of crystal was more roundish with somewhat irregular shapes (Figure 2.2f). These results also quite similar to the previous report.[13]

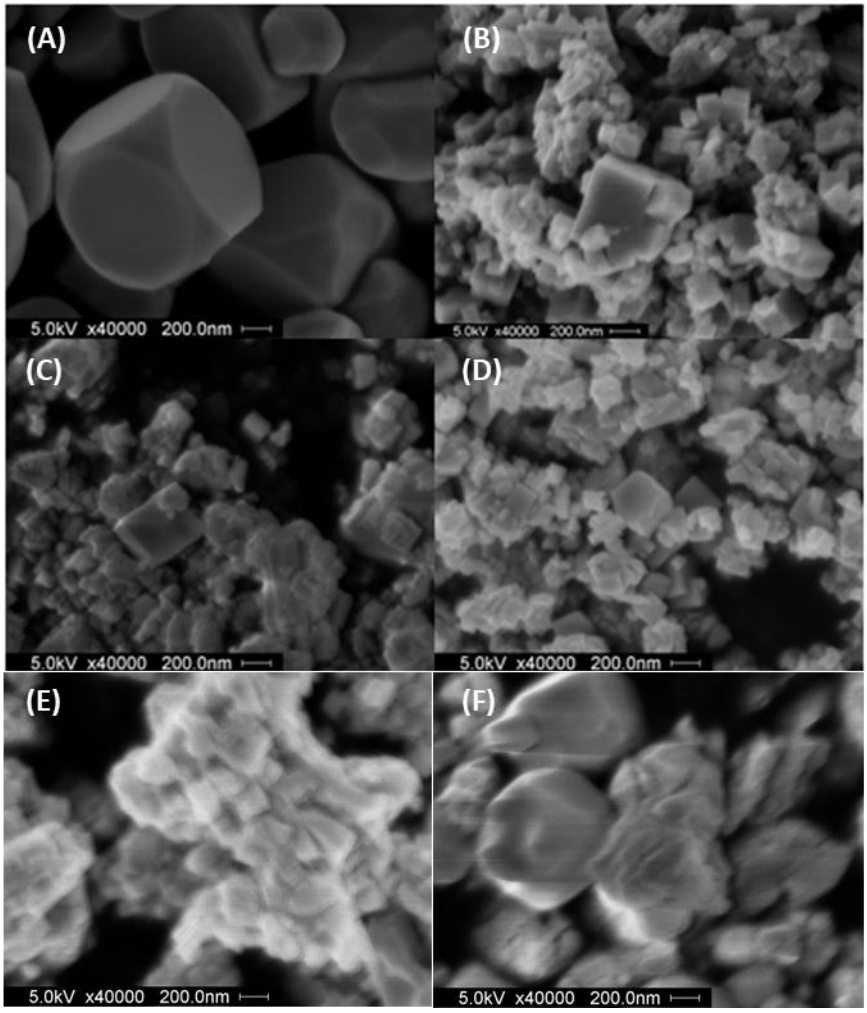

Figure 2.2 SEM images of the prepared samples: (a) non-doped NTO, (b) NTO:La(0.5), (c) NTO:La(1), (d) NTO:La(2), (e) NTO:La(5), and (f) NTO:La(2)SS.

Figure 2.3 shows XRD patterns of the non-doped NTO and various NTO:La samples. The diffraction lines of all the samples indicate the presence of the $NaTaO_3$ perovskite phase. No impurity phases related to La_2O_3 or La were detected, although it might be due to its low concentration of La dopant. The average crystallite size of each

sample was estimated and listed in Table 2.1. As shown, the more La dopant introduced into $NaTaO_3$, the smaller crystallite size was obtained. The NTO:La(2)SS sample had similar size of crystallites to the other NTO:La samples with low La doping such as the NTO:La(0.5) and NTO:La(1) samples. Note that the crystallites sizes determined by the XRD were much smaller than the particle size observed in the SEM images (Table 2.1). This means that the crystals observed in the SEM images were of not single crystals but polycrystals.[13,16] In the NTO:La(2) and NTO:La(5) samples, the crystallites size decreased with increasing La doping while the particle size increased. It is suggested that the larger amount of La ions enhanced aggregation of the particles of the smaller crystallites.

Table 2.1 Structural and optical properties of the prepared samples

Entry	Sample	La content[a] (mol%)	Average particle size[b] (μm)	Crystallite size[c] (nm)	$S_{BET\ powder}$[d] ($m^2\ g^{-1}$)	$S_{BET\ granule}$[e] ($m^2\ g^{-1}$)	Bandgap[e] (eV)
1	NTO	0.0	0.79	68	2.4	1.9	4.0
2	NTO:La(0.5)	0.3	0.29	50	5.3	5.4	4.1
3	NTO:La(1)	0.7	0.21	42	8.3	7.7	4.1
4	NTO:La(2)	1.7	0.25	35	7.5	7.4	4.1
5	NTO:La(5)	4.8	0.55	27	5.6	5.5	4.1
6	NTO:La(2)SS	1.5	0.41	43	4.1	3.9	4.1

[a] The actual La dopant measured by XRF. [b] Estimated from SEM images. [c] Average crystallite size calculated from a line width in XRD pattern. [d] Specific surface area of the powder sample measured by a BET method. [e] Specific surface area of the granule samples measured by a BET method. [f] Band gap estimated by Tauc plot from the DR UV-vis spectra.

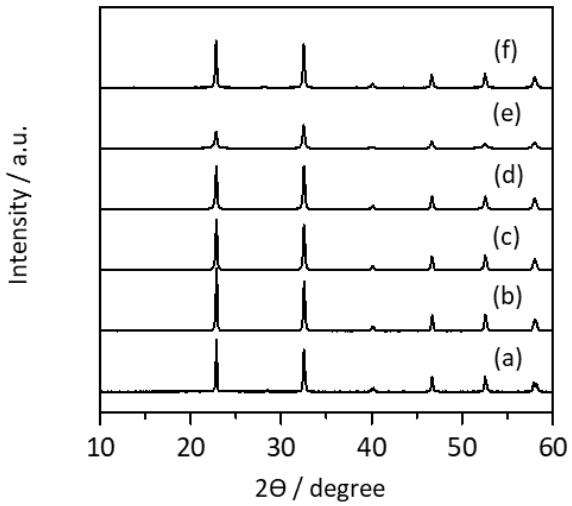

Figure 2.3 X-ray diffraction patterns of the samples, (a) non-doped NTO, (b) NTO:La(0.5), (c) NTO:La(1), (d) NTO:La(2), (e) NTO:La(5), and (f) NTO:La(2)SS.

The BET specific surface area of various samples were also listed in Table 2.1. As shown, the NTO:La(1) sample has the highest specific surface area compared to the other samples, supporting that doped lanthanum cations inhibit the crystal growth thus increase the specific surface area. The increase of specific surface area was consistent with the increasing La-doping amount in the range of 0–1 mol%. However, in the case of the NTO:La(2) and NTO:La(5) samples, the specific surface area were decreased with incresing the La doping, suggesting the aggregation of the particles decreased the specific surface area. Simply stated, the surface area should be inversely proportional to the particle size. Thus, the author estimated the relationship between the specific surface area and the average particle size based on the values of the samples with 0–1% La (Table 2.1) and confirmed an inversely proportional correlation (Figure 2.4). Such correlation was not obtained between the specific surface area and the crystallites size. This means that the BET specific surface area reflects the surface area of the polycrystal particles observed in the SEM images, not the crystallites size. It was found that the specific surface area for the NTO:La(2) and NTO:La(5) samples was higher than the expected correlation, suggesting that the aggregation provides interspaces between the

particles as a certain pore structure in the NTO:La(5) sample. Sun et al reported that higher Sr doping amount in $NaTaO_3$ samples were could decrease the surface area.[36]

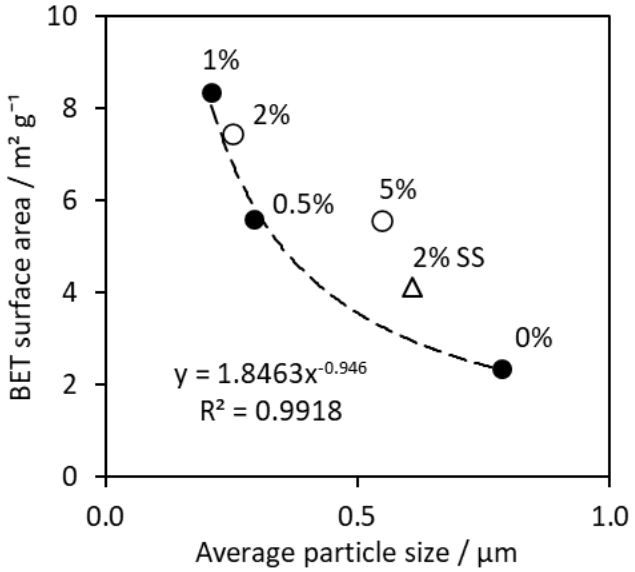

Figure 2.4 Relationship between particle size and BET surface area of the bare NTO and NTO:La samples prepared by a flux method. The symbols are the actual data. The dashed line was the curve expected from the values for the NTO:La samples with 0–1% of La doping.

The DR UV-visible spectra of the samples are shown in Figure 2.5. The bandgap of each sample was calculated by using Tauc Plot and listed in Table 2.1. These results suggest that La doping can enlarge the bandgap of $NaTaO_3$, which is consistent with the previous repor.[13]

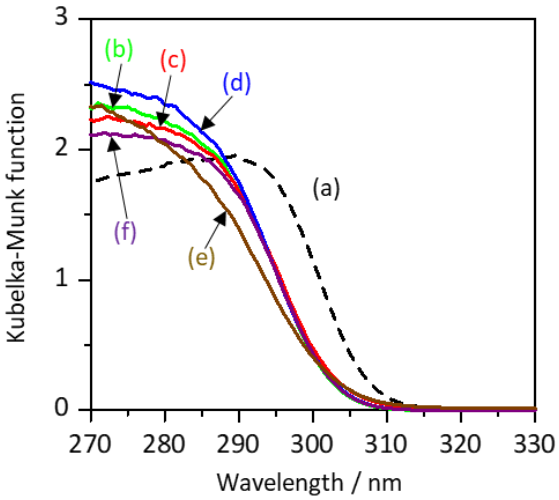

Figure 2.5 DR UV-Vis Spectra of the samples, (a) non-doped NTO, (b) NTO:La(0.5), (c) NTO:La(1), (d) NTO:La(2), (e) NTO:La(5), and (f) NTO:La(2)SS.

2.3.2. Photocatalytic activity test

Figure 2.6 shows the time course of the product formation rates in the photocatalytic reaction test for the PSRM with the NTO:La(2) sample in the flow of feed gas (25% CH_4, 2.4% H_2O and 72.6% Ar) at the atmospheric pressure at room temperature. Although the production rates of H_2 and CO_2 decreased slightly for the initial 4 hours, the production rate of H_2 and CO_2 became constant to be 21 and 4 µmol h^{-1}, respectively. It was found that CO was also produced in the addition of H_2 and CO_2. The CO production rate was constant from the start to be 1 µmol h^{-1}. Other gaseous oxidation product such as ethane was not detected by online GC-TCD. The product formation rates and the product selectivity were constant and the reaction continuously proceeded for a long time, at least for 20 hours. The ratio of photoexited electrons and holes that were consumed for the products formation, $R(e^-/h^+)$, was estimated from the formation rates of H_2, CO_2, and CO, which are R_{H2}, R_{CO2}, and R_{CO}, respectively, according to eq. 4. As shown in Figure 2.2, this ratio was almost unity, $R(e^-/h^+)=1$,

meaning that the products should be almost limited to H_2, CO_2, and CO. Based on these results, the CO selectivity among the oxidative products, S_{CO}(%), can be calculated according to eq. 5 and the CO selectivity was as high as 24% with the NTO:La(2) photocatalyst. The apparent quantum efficiency AQE(%) was estimated to be 0.12%, which was defined as the ratio of photon number used for the H_2 formation to the number of the incident photons that can be absorbed by the photocatalyst. No products were obtained in dark conditions or without employing a photocatalyst. These facts obviously indicate that the reaction takes place photocatalytically.

$$R(e^-/h^+)=R_{H2}/(3\times R_{CO} + 4\times R_{CO2}) \quad (4)$$

$$S_{CO}(\%)=100\times R_{CO}/(R_{CO}+R_{CO2}) \quad (5)$$

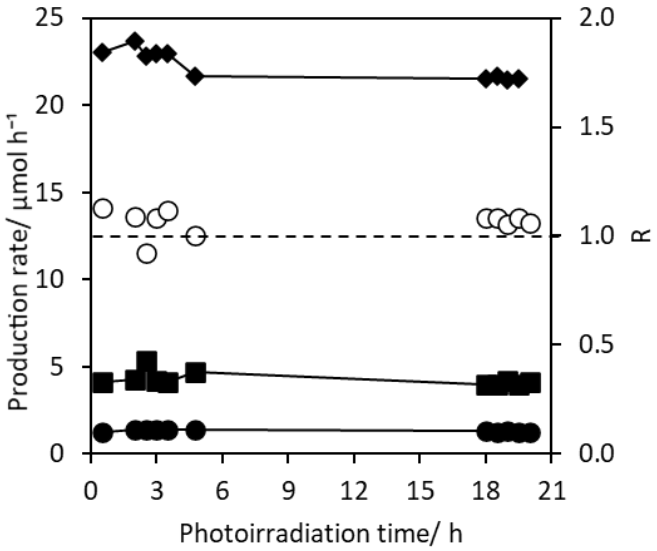

Figure 2.6 Time course of the production rate of H_2 (diamonds), CO_2 (squares), and CO (black circles) and $R(e^-/h^+)$ (white circles) that is the consumed electron/hole ratio calculated from the production rates. The NTO:La(2) photocatalyst (1.2 g) was used in a flow of the gas mixture (25% CH_4, 72.6% Ar, and 2.4% steam) at the flow rate of 15 ml min^{-1} under photoirradiation. The light intensity used was 165 mW cm^{-2} when measured at 254 ± 10 nm.

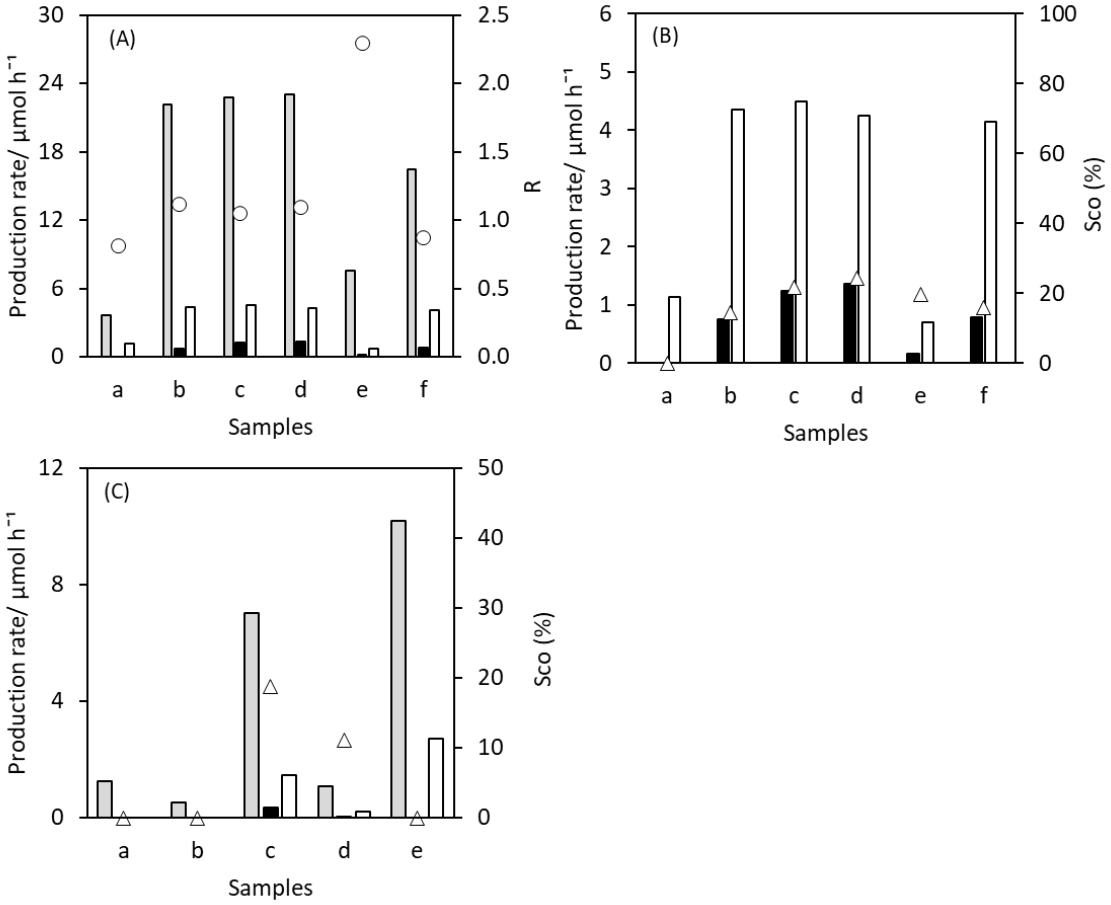

Figure 2.7 (A) Production rates of H_2 (gray bar), CO (black bar), and CO_2 (white bar) and the ratio of the consumed electrons and holes (white circle) in the various samples: (a) NTO, (b) NTO:La(0.5), (c) NTO:La(1), (d) NTO:La(2), (e) NTO:La(5), and (f) NTO:La(2) SS. (B) Enlarged graph showing the CO and CO_2 production rates and the CO selectivity, S_{CO} (white triangle). (C) Photocatalytic production rates and CO selectivity with another series of samples on which a La oxide species was loaded by the impregnation method: (a) NTO, (b) La(0.3)/NTO, (c) NTO:La(1), (d) La(0.3)/NTO:La(1), and (e) Pt(0.1)/NTO:La(1). Photocatalyst: 1.2 g. Photoirradiation area: 6 cm^2. The feed gas consists of 25% CH_4, 72.6% Ar, and 2.4% steam (total flow rate: 15 ml min^{-1}). Light intensity: 165 mW cm^{-2} for (A) and (B) and 27 mW cm^{-2} for (C). Sampling was carried out after 4 hours irradiation.

Figure 2.7 shows the photocatalytic activity of various samples. All the prepared La-doped $NaTaO_3$ samples without any cocataysts showed photocatalytic activity to produce CO in the PSRM. As shown in Figure 2.7A, the NTO:La(*x*) samples exhibited higher photocatalytic activities to produce H_2, CO_2, and CO than the non-doped NTO sample (Figure 2.7A a–e). It is confirmed that La doping could increase the photocatalytic activity of $NaTaO_3$.[12,33] Among them, the NTO:La(0.5), NTO:La(1), and NTO:La(2) samples gave the highest photocatalytic activity, e.g., the NTO:La(2) gave 23 μmol h^{-1} H_2, 1 μmol h^{-1} CO, and 4 μmol h^{-1} CO_2 (Figure 2.7Ad). The NTO:La(2)SS sample also showed high production rates (Figure 2.7Af) but lower than the NTO:La(2) sample (Figure 2.7Ad). This result reveal that sample prepared by the flux method had better photocatalytic activity in the PSRM, which is quite similar to the previous report.[13] The ratio of the electrons and holes consumed for entire samples were almost unity except the NTO:La(5) sample (Figure 2.7Ae). Unbalance of electron and hole consumption in the NTO:La(5) sample might be caused by production of some oxidative products undetected, such as coke.

To compare the CO production rate and selectivity, the enlarged graph is shown in Figure 2.7B. The NTO:La(x) and NTO:La(2)SS samples produce CO as a minor product. The La-doped samples showed higher CO production rate than the non-doped NTO sample although the NTO:La(5) sample gave low CO production rate among them. However, the CO selectivity with each photocatalyst was in range of 15% to 24%, meaning that the CO selectivity did not varied so much with the amount of La-doping. Although the non-doped NTO sample could not show the CO formation, this may originate from the low photocatalytic activity.

In order to investigate the role of La-doping in crystal, another series of samples were prepared, i.e., La oxide species was loaded on the surface of the non-doped NTO and NTO:La(1) samples, and examined for the photocatalytic reaction test (Figure 2.7C). Although the photocatalytic H_2 production rate over the NTO sample was 1.26 μmol h^{-1} (Figure 2.7Ca), that on the La(0.3)/NTO sample

was 0.53 μmol h^{-1} (Figure 2.7Cb), meaning that the La oxide species on the NTO surface decreased the photocatalytic activity to less than half. This negative effect was also observed on the NTO:La(1) sample (Figure 2.7C, c and d). These results suggested that the surface La oxide species would change the properties of the photocatalytic active sites to decrease photocatalytic activity. Thus, the La doping effect on the photocatalytic activity of the NTO:La photocatalysts should be generated by not the La oxide species located on the surface but the La^{3+} cations incorporated in the crystal structure. Onishi et al. reported that electron-hole recombination process was suppressed by La doping in $NaTaO_3$ host.[37,38] The gradient of electrostatic potential due to La doping promote more efficient change separation.[37] However, the photocatalytic activity of the NTO:La(5) sample was almost the same as that of the bare NTO sample (Figure 2.7A, a and e), which is also consistent with the literature.[37] The excess La doping in $NaTaO_3$ might produce the La oxide species on the surface to decrease the photocatalytic activity.

To know the effect of metal cocatalysts, various metal loaded NTO:La(1) samples were examined as listed in Table 2.2. These metal loaded samples exhibited lower photocatalytic activity for CO production than the bare NTO:La(1) sample. The addition of a Pt cocatalyst on the NTO:La(1) sample increased the hydrogen production rate but suppressed CO formation, which is consistent with the previous study. Loading a Pd cocatalyst also could change the photocatalyst selectivity. Since the NTO:La(1) sample without any loaded cocatalysts could produce H_2, CO, and CO_2, it is demonstrated that the surface sites of the bare NTO:La photocatalyst could originally produce H_2, CO, and CO_2 and Pt and Pd cocatalysts only promote the formation of H_2 and CO_2.[10–14,16,37] It is usually considered that Pt can function as a good cocatalyst to enhance the electron and hole separation and thus enhance the photocatalytic activity.[13–16,40,41] Thus, even if the photocatalyst produces CO, the Pt metal cocatalyst might promote successive conversion of CO with H_2O to form CO_2. On the other hand, the other

metal species such as Ag, Ni, Cu, and Zn show negative effects on both the photocatalytic activity and CO selectivity (Table 2.2). These cocatalysts would interact with the surface active sites of the bare photocatalyst and make them less reactive.

Table 2.2 Photocatalytic activity of various photocatalysts in the PSRM [a]

Entry	Sample	Metal loading amount (wt%)	Production rate / μmol h^{-1}			S_{CO} (%)	R
			H_2	CO	CO_2		
1	NTO:La(1)	-	8.0	0.4	1.6	20%	1.1
2	Pt(0.1)/NTO:La(1)	0.1	10.2	0.0	2.7	0%	1.0
3	Pd(0.1)/NTO:La(1)	0.1	9.1	0.0	0.2	0%	12.8
4	Au(0.1)/NTO:La(1)	0.1	7.7	0.3	1.4	17%	1.2
5	Ag(0.1)/NTO:La(1)	0.1	3.6	0.1	0.3	17%	2.4
6	NiO(0.7)/NTO:La(1)	0.7	5.5	0.0	0.4	0%	3.1
7	CuO(1)/NTO:La(1)	1	3.9	0.1	0.7	16%	1.3
8	ZnO(1)/NTO:La(1)	1	0.1	0.0	0.0	0%	-
9	non-doped NTO	-	1.3	0.0	0.0	0%	-
10	Ga_2O_3	-	2.2	0.1	0.4	19%	1.1
11	ZnO	-	0.3	0.0	0.0	0%	-
12	TiO_2	-	0.2	0.0	0.0	0%	-

[a] Reaction conditions: photoirradiation area, 6 cm^2; feed gas: 25% CH_4, 72.6% Ar, and 2.4% steam (total flow rate: 15 ml min^{-1}); light intensity: 27 mW cm^{-2}.

As a comparison, the author also checked the photocatalytic activity and CO selectivity of some other photocatalyst samples such as Ga_2O_3, TiO_2, and ZnO as listed in Table 2.2 entries 10–12. These samples were used directly without any additional pretreatment. As a result, NTO:La(1) exhibited the highest photocatalytic activity and CO selectivity among them. The Ga_2O_3 sample also showed photocatalytic activity to produce H_2, CO, and CO_2 with a high CO selectivity, 19%. In contrast, non-doped NTO, ZnO and TiO_2 showed low photocatalytic activities for H_2 and no CO or CO_2 formation.

2.3.3. Reaction scheme for CO production

To elucidate the possibilities of the successive reactions of produced CO_2 to give CO, such as photocatalytic dry reforming of methane (PDRM, eqn (6)) and photocatalytic reverse water gas shift (PRWGS, eqn (7)), the author performed photocatalytic reaction tests with the NTO:La(1) photocatalyst.

$$CO_2 + CH_4 \rightarrow 2CO + 2H_2 \qquad \Delta G^{\circ}_{298K} = 170.7\ \mathrm{kJ\ mol^{-1}} \quad (6)$$

$$CO_2 + H_2 \rightarrow CO + H_2O \qquad \Delta G^{\circ}_{298K} = \ \ 28.6\ \mathrm{kJ\ mol^{-1}} \quad (7)$$

In the PDRM experiment, the concentration of CO_2 in the feed gas mixture was 20%, CH_4 was 20% and the rest was Ar gas, while in the PRWGS experiment the composition of feed gas was 20% of CO_2, 20% of H_2, and 60% of Ar gas. Although this CO_2 concentration was much higher than that acheived in the PSRM reaction experiments in this study, there were no gasseous product in both reactions, meaning that these reactions did not take place successsively. Although CO_2 reduction using water as an electron source is another probable reaction, Nakanishi et al. already reported that La doped $NaTaO_3$ without cocatalyst was not active for producing CO through CO_2 reduction with water.[39]

On the other hand, to elucidate the successive reaction of produced CO with water, the tests for photocatalytic water-gas shift (PWGS, eq.2) were carried out with various NTO and NTO:La photocatalysts (Figure 2.8), where the feed gas mixture

consisted of 15% of CO, 2.7% of H_2O, and 82.3% of Ar. In the dark condition, there were no H_2 and CO_2 observed (not shown). However, upon the light irradiation, the gaseous products were clearly detected. It was found that the WGS can occur photocatalytically in the conditions with these photocatalysts. The ratio of products, $R_{WGS}(e^-/h^+)$, were estimated by using eq.8 which R_{H2} and R_{CO2} were production rates for H_2 and CO_2, respectively.

$$R_{WGS}(e^-/h^+)=R_{H2}/R_{CO2} \qquad (8)$$

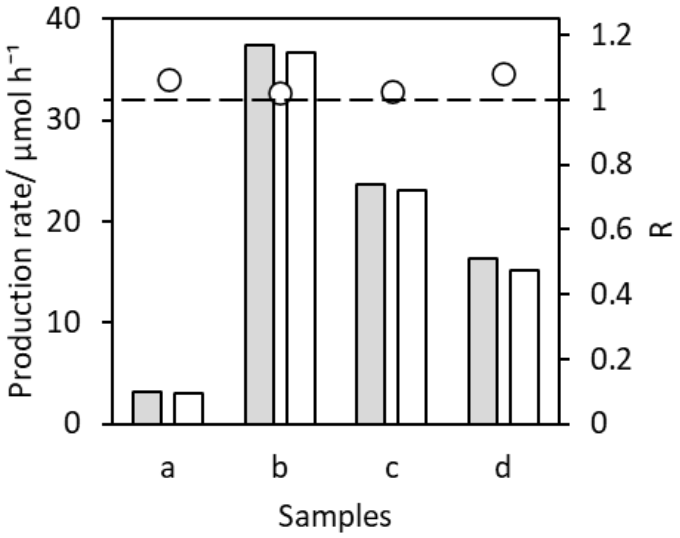

Figure 2.8 Production rate of H_2 (gray bar) and CO_2 (white) and $R_{WGS}(e^-/h^+)$ (open circle) in the photocatalytic water gas shift (PWGS) reaction test over the samples: (a) bare NTO, (b) NTO:La(1), (c) NTO:La(2), and (d) NTO:La(5). Photocatalyst: 1.2 g, photoirradiation area: 6 cm^2, reactant: 15% CO, 2.7% H_2O and Ar as the balance, flow rate: 15 ml min^{-1}. Sampling was carried out after 2 hours irradiation.

In the PWGS experiment, the ratio of electrons and holes consumption was unity with these samples, which is consistent with eq. 2. These photocatalysts, especially the NTO:La photocatalysts, was highly active for the photocatalytic WGS (PWGS). These high production rates would be related to the lower reaction Gibbs energy for the WGS. It is known that steam reforming of methane (SRM) is highly endogernic reaction while

water gas shift (WGS) is exothermic reaction as mentioned above (eq. 2 and 3). This result revealed that photocatalytic water gas shift can occur in the photocatalytic steam reforming of methane (PSRM) with the NTO and NTO:La photocatalysts and the latter is more active. This is the first report that a bare semiconductor photocatalyst without cocatalyst promotes water gas shift (WGS) with high selectivity.

These results suggest that CO was produced in the photocatalytic steam reforming (PSRM, eq. 1) and converted to CO_2 in the photocatalytic water gas shift reaction (PWGS, eq. 2). This provides a steady state for the CO production, which is the reason why the CO selectivity was low such as 15–24% in the present system. Further, the successive reaction of CO_2 with CH_4 (PDRM, eq. 6) and H_2 (PRWGS, eq.7) to produce CO could scarecely take place in the present conditions as mentioned. Thus, the proposed scheme for CO production is summarized in Scheme 1. If the successive PWGS can be controlled by the development of photocatalyst or reaction conditions, higher CO selectivity will be obtained.

$$CH_4 \xrightarrow{H_2O} \mathbf{CO} + 3H_2 \xrightarrow{H_2O} CO_2 + 4H_2$$
$$2\mathbf{CO} + 2H_2 \not\longleftarrow CO_2 + CH_4$$
$$\mathbf{CO} + H_2O \not\longleftarrow CO_2 + H_2$$

Scheme 1 Proposed reaction scheme for CO production in the photocatalytic steam reforming of methane over a $NaTaO_3$:La photocatalyst based on the experimental results.

2.3.4. Reaction conditions

The influence of the reaction conditions, such as the light intensity, the flow rate of reactants, and the CH_4 concentration, on the photocatalytic activity and the CO selectivity were also investigated. Figure 2.9A shows the effect of the irradiation light intensity on the photocatalytic performance of the NTO:La(2) photocatalyst, where the light intensities utilized were 27, 35, and 165 mW cm^{-2}

without using optical filter, which represent incident photon numbers, 1.1×10^{18}, 1.4×10^{18}, and 6.6×10^{18}, respectively. As mentioned, no reaction occurred in dark. The higher light intensity provide higher production rates, which is quite reasonable as photocatalysis. Interestingly, it was found that the CO selectivity also slightly increased with increasing the light intensity from 18% to 24%. It is suggested that the CO selectivity should be related to the difference of the reaction rates of the first PSRM (eq. 1) and the successive PWGS (eq. 2). As shown in eq. 1, it required 6 pairs of electrons and holes to promote CO generation in PSRM, while PWGS only needs 2 pairs of charge carriers. By increasing light intensity, more electrons and holes will be available for these photocatalytic reactions, which might be more critically beneficial to the first PSRM direction rather than the successive PWGS reaction, resulting the higher CO formation rate. Higher temperature originating from the high light intensity also might be another possibility of increasing CO selectivity since the PSRM is endothermic reaction while PWGS is exothermic.

Figure 2.9B shows the effect of the increasing total flow rate of the reaction mixture (15, 30, and 50 ml min^{-1}), giving a decrease of the contact time (2.4, 1.2, and 0.7 s, respectively), on the methane conversion and the CO selectivity over the NTO:La(2) photocatalyst. As expected, the methane conversion decreased with increasing the flow rate because of less contact time. The CO_2 production rate decreased with increasing the flow rate (Figure 2.10A), while the CO production rate of CO was observed to be almost the same in various flow rates, resulting a slightly higher CO selectivity at the highest flow rate. In principle, high flow rate with short contant time should lower the both reaction rates, the CH_4 conversion to CO (eq. 1) and the successive reaction of CO to CO_2 (eq. 2). In the present case, it was revealed that the short contact time can further limit the successive reaction of CO to CO_2 because of practically less contact time for the successive reaction. It is concluded here that contact time limitation can slightly increase the CO selectivity.

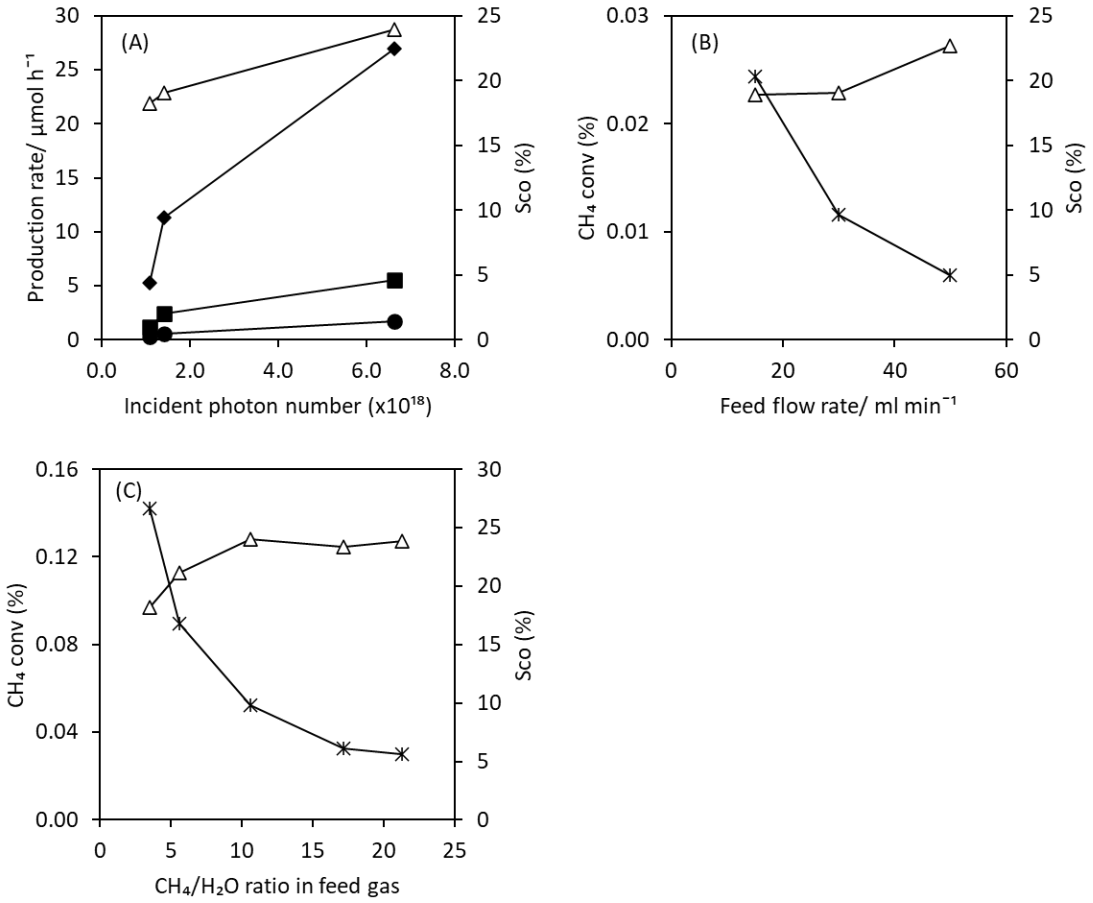

Figure 2.9 Formation rate of CO (circle), CO_2 (square), and H_2 (diamond) together with CO selectivity (triangle) and CH_4 conversion (asterisk) under different reaction conditions: (A) various incident photon numbers; flow rate, 30 ml min^{-1}; feed gas composition: CH_4 (35%), steam (2%), and Ar (balance); photocatalyst, the NTO:La(2) sample, (B) various flow rates of the feed gas mixture: 15, 30, and 50 ml min^{-1}; light intensity, 35 mW cm^{-2}; feed gas composition: CH_4 (35%), steam (2%), and Ar (balance); photocatalyst, the NTO:La(2) sample, and (C) various CH_4/H_2O ratios in the feed gas: CH_4 (10–40%), steam (1.9–2.8%), and Ar (balance); light intensity, 165 mW cm^{-2}; flow rate, 15 ml min^{-1}; photocatalyst, the NTO:La(1) sample. The mass of photocatalyst used was 1.2 g and the irradiation area was 6 cm^2 for each experiment. See also Figure 2.10

Figure 2.9C and Figure 2.10B show the effect of the composition in the feed gas mixture on the photocatalysis with the NTO:La(1) photocatalyst, where the CH_4 concentration was varied in the constant H_2O concentration to provide various ratio of CH_4 to H_2O. The ratios of CH_4/H_2O examined were from 3.5 to 21, much higher than CH_4/H_2O stoichiometric ratio, 0.5. The graph shows, by increasing CH_4/H_2O ratio, the CH_4 conversion decreased gradually and become stable. The CO selectivity increased in the range of the lower CH_4/H_2O ratio from 3.5 to 11 and became constant at the higher ratio range. Water would be strongly adsorbed on the photocatalyst surface like as a liquid film at this low temperature, so that excess amount of CH_4 is required to perform PSRM (eq. 1), but further increase does not influence so much. Moreover, one additional experiment was conducted in the flow of the gas mixture with very high CH_4/H_2O ratio (90% of CH_4 and 0.3% of H_2O in Ar) at the flow rate of 15 ml min^{-1} (Figure 2.11). The ratio of electron and hole consumption was not unity, $R(e^-/h^+)$ was around 2. Since CH_4 concentration was very high, it was suggested that methane decomposition occurs to form carbon although the reaction time was not enough to change the color of photocatalyst. However, these conditions gave a high CO selectivity such as 39%, which would originate from the further acceleration of the first PSRM (eq. 1) and limitation of the successive PWGS reaction (eq. 2).

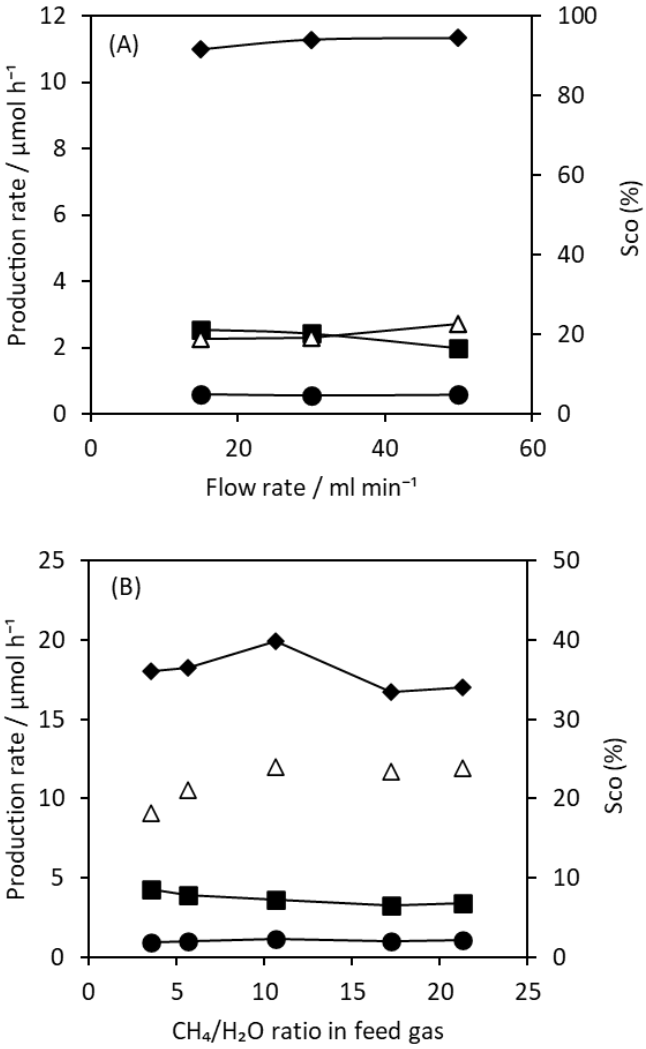

Figure 2.10 Photocatalytic production rates of CO (circle), CO_2 (square), and H_2 (diamond) equipped with the CO selectivity (triangle) in various reaction conditions, (A) various flow rates of the feed gas mixture: 15, 30, and 50 ml min^{-1} ; light intensity, 35 mW cm^{-2} ; feed gas composition: CH_4 (35%), steam (2%), and Ar (balance); the photocatalyst, the NTO:La(2) sample, and (B) various CH_4/H_2O ratio in the feed gas: CH_4 (10–40%), steam (1.9-2.8%), and Ar(balance); light intensity, 165 mW cm^{-2} ; flow rate, 15 ml min^{-1} ; the photocatalyst, the NTO:La(1) sample. The photocatalyst used was 1.2 g and the irradiation area was 6 cm^2 , in common.

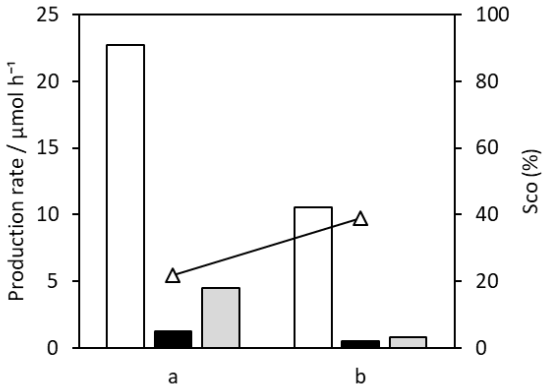

Figure 2.11 Photocatalytic production rates of H_2 (white bar), CO (black bar), CO_2 (gray bar) as well as S_{CO} (white triangle, the CO selectivity) in different CH_4 concentrations, (a) 25% of CH_4, 2.4% of steam, 72.6% of Ar and (b) 90% of CH_4, 0.3% of steam, 9.7% of Ar, over the NTO:La(1) photocatalyst. Photocatalyst: 1.2 g, photoirradiation area: 6 cm^2, and light intensity: 165 mW cm^{-2}. Sampling was carried out after 2 hours irradiation.

These results with various reaction conditions support the proposed scheme mentioned above (Scheme 1).

2.4. Conclusion

Photocatalytic steam reforming of methane (PSRM) to produce CO was successfully uncovered by employing a La-doped $NaTaO_3$ photocatalyst without a cocatalyst. This reaction produces CO and CO_2 simultaneously. The presence of water and CO also initiates the photocatalytic water gas shift reaction (PWGS), which decreases the CO production rate. The selectivity to CO in the PSRM was controlled by the photocatalyst properties and the reaction conditions such as the light intensity, the flow rate of the reactant, and the ratio of CH_4 to H_2O in the feed gas mixture to some extent. However, an excellent achievement is very difficult to be obtained by changing these parameters in the present ranges with the current photocatalyst and the reaction system. Thus, the development of the photocatalyst and the reactor would be desirable for further improvement.

References

1 J. R. Rostrup-Nielsen, *Catal. Today*, 1993, **18**, 305–324.

2 J. M. Cormier and I. Rusu, *J. Phys. Appl. Phys.*, 2001, **34**, 2798–2803.

3 T. V. Choudhary and V. R. Choudhary, *Angew. Chem. Int. Ed.*, 2008, **47**, 1828–1847.

4 X. Zhu, H. Wang, Y. Wei, K. Li and X. Cheng, *J. Rare Earths*, 2010, **28**, 907–913.

5 N. Salhi, A. Boulahouache, C. Petit, A. Kiennemann and C. Rabia, *Int. J. Hydrog. Energy*, 2011, **36**, 11433–11439.

6 K. Y. Koo, S. Lee, U. H. Jung, H.-S. Roh and W. L. Yoon, *Fuel Process. Technol.*, 2014, **119**, 151–157.

7 M. A. Nieva, M. M. Villaverde, A. Monzón, T. F. Garetto and A. J. Marchi, *Chem. Eng. J.*, 2014, **235**, 158–166.

8 L. Yuliati and H. Yoshida, *Chem. Soc. Rev.*, 2008, **37**, 1592.

9 K. Shimura and H. Yoshida, *Energy Environ. Sci.*, 2011, **4**, 2467.

10 H. Yoshida, S. Kato, K. Hirao, J. Nishimoto and T. Hattori, *Chem. Lett.*, 2007, **36**, 430–431.

11 H. Yoshida, K. Hirao, J. Nishimoto, K. Shimura, S. Kato, H. Itoh and T. Hattori, *J. Phys. Chem. C*, 2008, **112**, 5542–5551.

12 K. Shimura, S. Kato, T. Yoshida, H. Itoh, T. Hattori and H. Yoshida, *J. Phys. Chem. C*, 2010, **114**, 3493–3503.

13 A. Yamamoto, S. Mizuba, Y. Saeki and H. Yoshida, *Appl. Catal. Gen.*, 2016, **521**, 125–132.

14 K. Shimura, H. Miyanaga and H. Yoshida, in *Studies in Surface Science and Catalysis*, eds. E. M. Gaigneaux, M. Devillers, S. Hermans, P. A. Jacobs, J. A. Martens and P. Ruiz, Elsevier, 2010, vol. 175, pp. 85–92.

15 K. Shimura and H. Yoshida, *Energy Environ. Sci.*, 2010, **3**, 615–617.

16 A. Anzai, K. Fujiwara, A. Yamamoto and H. Yoshida, *Catal. Today*, 2020, **352**, 1–9.

17 K. Shimura, H. Kawai, T. Yoshida and H. Yoshida, *Chem. Commun.*, 2011, **47**, 8958–8960.

18 K. Shimura, H. Kawai, T. Yoshida and H. Yoshida, *ACS Catal.*, 2012, **2**, 2126–2134.

19 K. Shimura, T. Yoshida and H. Yoshida, *J. Phys. Chem. C*, 2010, **114**, 11466–11474.

20 K. Shimura, K. Maeda and H. Yoshida, *J. Phys. Chem. C*, 2011, **115**, 9041–9047.

21 K. Shimura and H. Yoshida, *Phys. Chem. Chem. Phys.*, 2012, **14**, 2678–2684.

22 C. E. Taylor and R. P. Noceti, *Catal. Today*, 2000, **55**, 259–267.

23 M. A. Gondal, A. Hameed, Z. H. Yamani and A. Arfaj, *Chem. Phys. Lett.*, 2004, **392**, 372–377.

24 S. Murcia-López, K. Villa, T. Andreu and J. R. Morante, *ACS Catal.*, 2014, **4**, 3013–3019.

25 K. Villa, S. Murcia-López, J. R. Morante and T. Andreu, *Appl. Catal. B Environ.*, 2016, **187**, 30–36.

26 S. Murcia-López, M. C. Bacariza, K. Villa, J. M. Lopes, C. Henriques, J. R. Morante and T. Andreu, *ACS Catal.*, 2017, **7**, 2878–2885.

27 J. Xie, R. Jin, A. Li, Y. Bi, Q. Ruan, Y. Deng, Y. Zhang, S. Yao, G. Sankar, D. Ma and J. Tang, *Nat. Catal.*, 2018, **1**, 889–896.

28 Y. Zhou, L. Zhang and W. Wang, *Nat. Commun.*, 2019, **10**, 506.

29 J. Du, W. Chen, G. Wu, Y. Song, X. Dong, G. Li, J. Fang, W. Wei and Y. Sun, *Catalysts*, 2020, **10**, 196.

30 H. Yoshida, S. Mizuba and A. Yamamoto, *Catal. Today*, 2019, **334**, 30–36.

31 F. Amano, C. Akamoto, M. Ishimaru, S. Inagaki and H. Yoshida, *Chem. Commun.*, 2020, **56**, 6348–6351.

32 J. Tauc, R. Grigorovici and A. Vancu, *Phys. Status Solidi B*, 1966, **15**, 627–637.

33 H. Kato, K. Asakura and A. Kudo, *J. Am. Chem. Soc.*, 2003, **125**, 3082–3089.

34 X. Li and J. Zang, *Catal. Commun.*, 2011, **12**, 1380–1383.

35 H. Sudrajat, S. Babel, I. Thushari and K. Laohhasurayotin, *J. Alloys Compd.*, 2019, **775**, 1277–1285.

36 J. Sun, G. Chen, J. Pei, R. Jin, Q. Wang and X. Guang, *J. Mater. Chem.*, 2012, **22**, 5609–5614.

37 A. Yamakata, T. Ishibashi, H. Kato, A. Kudo and H. Onishi, *J. Phys. Chem. B*, 2003, **107**, 14383–14387.

38 M. Maruyama, A. Iwase, H. Kato, A. Kudo and H. Onishi, *J. Phys. Chem. C*, 2009,

113, 13918–13923.

39 H. Nakanishi, K. Iizuka, T. Takayama, A. Iwase and A. Kudo, *ChemSusChem*, 2017, **10**, 112–118.

3. Granule of potassium hexatitanate fine crystals for photocatalytic steam reforming of methane

Abstract

Photocatalytic steam reforming of methane (PSRM) can produce hydrogen from methane even at room temperature and thus has been studied recently. In the present study, in order to know the structural aspects affecting the photocatalytic performance, many fine rod-like crystals of potassium hexatitanate ($K_2Ti_6O_{13}$, KTO) were synthesized by a flux method with varying the preparation conditions and examined their photocatalytic activities for the PSRM after loading Rh cocatalyst. It was found that a Rh/KTO fine crystal photocatalyst with larger surface area exhibited the highest hydrogen production rate (up to 30 μmol h^{-1}) with high selectivity. Further, the granulated crystals exhibited 2.1–2.6 times higher hydrogen production rate than the original powdery fine crystals, suggesting that the physical contact between the fine crystals contributes to the interparticle transfer of the photoexcited carriers and thus enhancing the photocatalytic activity.

3.1. Introduction

Hydrogen is one of the promising and important chemical compounds as a fuel and a chemical feedstock for useful chemicals such as methanol and ammonia. There are several method to produced hydrogen such as steam reforming of methane,[1–6] partial oxidation of methane,[7–9] coal gasification,[10,11] methane pyrolysis,[12–14] water electrolysis,[15–17] and so on. As the cheapest route to produce hydrogen, currently, steam reforming of methane (SRM) reaction has become an industrially established system, where the reactants are methane (CH_4), as a main component of natural gas and biogas, and water. The overall chemical equation for this reaction with the successive water gas shift is shown as follows:

$$CH_4 + 2\ H_2O \rightarrow CO_2 + 4\ H_2 \qquad \Delta G^{\circ}_{298K} = 113.5\ \text{kJ mol}^{-1} \qquad (1)$$

This reaction is highly endergonic which requires a tremendous amount of energy to take place, in other words, high reaction temperature is necessary, and thus practically heat from methane combustion is utilized for increasing the temperature in the current SRM, which needs considerable consumption of fossil resource as energy. Further, the high-temperature reaction requires an expensive heat-resistant reactor and careful operation to avoid catalyst deactivation due to coking. Thus, the development of the SRM reaction system that can work at low temperature has been desired.

Photocatalytic reaction system can utilize photoenergy to convert chemical substances. The free and abundance of solar light makes photocatalysis become an attractive method to be developed for many reaction systems. Especially, the use of photoenergy at low temperature for the endergonic SRM reaction is a fascinating combination. Recently, photocatalytic steam reforming of methane (PSRM) was discovered by employing Pt-loaded TiO_2,[18] and Pt-loaded La-doped $NaTaO_3$.[18,19] Afterward, other photocatalysts have been also developed for H_2 production in the PSRM, i.e., Pt-loaded $CaTiO_3$,[20] Rh-loaded $K_2Ti_6O_{13}$,[21,22] Pt-loaded β-Ga_2O_3,[23] Pt-loaded La-doped $CaTiO_3$,[24] Rh-loaded $Na_2Ti_6O_{13}$,[25] Rh-loaded TiO_2,[26] Pt-loaded black TiO_2,[27] La-loaded TiO_2,[28] Ag^0/Ag^+-loaded $SrTiO_3$,[29] and Pt-loaded YSZ (yttria stabilized zirconia).[30]

Most of the photocatalysts with cocatalyst can utilize light as an energy source and steam (H_2O) as an oxidant to convert methane (CH_4) to H_2 and CO_2 in a molar ratio of $H_2/CO_2 = 4$ even around room temperature although a few photocatalysts can produce CO as a minor product.[22,31] Among these photocatalysts, the Rh-loaded $K_2Ti_6O_{13}$ photocatalyst,[21,22] has been the most active photocatalyst in the room temperature PSRM system,[22] where the $K_2Ti_6O_{13}$ sample was prepared by a conventional solid-state reaction method.

In general, it has been considered that photocatalyst with less crystal defects provides less recombination of photoexcited electrons and holes to increase the photocatalytic performance, a large specific surface area can provide a large reaction field, and some crystal facets specialized for reductive and oxidative reactions are preferable for the high performance in the photocatalytic reactions. Based on these matters, a flux method has been considered as an advantageous method to obtain such photocatalyst fine crystals since the material can be synthesized in a molten salt to form microcrystals of unique morphology covered with facets with less defects. This method has been used for fabrication of various titanates-based crystals such as $Na_2Ti_6O_{13}$,[25,32,33] $K_2Ti_6O_{13}$,[34–38] and $KTi_8O_{16.5}$,[32] $Na_2Ti_3O_7$,[39] $Li_4Ti_5O_{12}$,[40] $ATiO_3$ (A= Ca, Sr, Ba, and Pb),[24,41–48] $La_2Ti_2O_7$,[49–52] etc. In particular, the fine $K_2Ti_6O_{13}$ crystal, which has some facets, has been reported as a photocatalyst for water splitting,[34,53,54] CO_2 reduction with water,[37,38,55] and degradation of various organic contaminants such as methyl orange [56] and amoxicillin.[57]

In the present study, the author prepared several $K_2Ti_6O_{13}$ crystals by a flux method in various conditions, loaded Rh cocatalyst on the crystals, and examined them for the PSRM reaction test. As a result, a Rh loaded $K_2Ti_6O_{13}$ photocatalyst consisting of smaller microcrystals with thinner short facet and higher surface area exhibited higher photocatalytic activity compared to the sample prepared by the conventional solid-state reaction method. In addition, it was found that the granulated photocatalyst exhibited higher activity than the powder sample.

3.2. Experimental method

3.2.1. Catalyst preparation

Potassium hexatitanate ($K_2Ti_6O_{13}$, referred to as KTO) was mainly synthesized by a flux method. The typical procedure was as follows. The starting materials, K_2CO_3 (Kishida, 99.9%) and rutile TiO_2 (Kojundo, 99.9%), and a flux such as KCl (Kishida, 99.5%), NaCl (Kishida, 99.5%), or $CaCl_2$ (Kishida, 95.0%), were physically mixed for 15 min in an alumina mortar. The molar ratio for K_2CO_3 and TiO_2 was always 1:6 while the solute concentration was varied from 10 to 90 mol%. The mixture in a platinum crucible was heated in an electrical furnace, where the temperature was elevated from room temperature to various destined temperature (from 973 K to 1473 K) with an increasing rate (200 K h^{-1}). After holding for 10 h in the temperature, the sample was cooled down at 100 K h^{-1} to 773 K. The cooling process continued to ambient temperature naturally in the furnace. The product was gently crashed in alumina mortar and washed three times to remove the flux by using hot deionized water (353 K, 500 ml). The filtered sample was then put in an oven at 353 K overnight to remove the remaining water. These samples were referred to as KTO(*flux*,*x*,*y*), where *flux* shows the used salt such as NaCl, *x* is the molar ratio of the solute (mol%), and *y* is the highest temperature (K). After KCl was found to be the most suitable flux, the KCl flux was not indicated in the sample name. A KTO sample was prepared with a short holding time, 1 h instead of 10 h, with a KCl flux at 1173 K (referred to as KTO(30,1173)1h). Another sample was prepared in the same way by using anatase TiO_2 (Ishihara Sangyo Kaisha, ST-01, 300 m^2 g^{-1}) as a start material instead of rutile TiO_2 with a KCl flux (KTO(30,1173)ana).

For comparison, a solid-state reaction (SSR) method was used for the preparation of two samples without using any flux, corresponding to *x* = 100%, at 1173 or 1373 K. The procedure was the same as mentioned above. These samples were referred to as KTO(SSR,100,*y*).

Rhodium cocatalyst was loaded on the KTO surface by an impregnation method.[22] Compared to photodeposition method that is often used for photocatalyst,

impregnation method would give the same state and the same content of the Rh cocatalyst on each KTO sample regardless the structure and photocatalytic activity, which would be helpful to discuss the differences of the KTO crystals themselves. The KTO samples (1.2 g) were dispersed in a $RhCl_3$ aqueous solution (Kishida, 99%) (100 ml, 0.03 wt%) and stirred magnetically at 353 K until whole water was evaporated, then dried in the oven at 353 K overnight. The obtained powder sample was mixed carefully for 10 minutes and heated at 773 K for 2 h. The samples are referred to as Rh/KTO(*x*,*y*) for example.

3.2.2. Characterization

Crystal structure of the KTO samples were evaluated by X-ray diffraction (XRD) pattern measured using a Shimadzu Lab X XRD-6000 at room temperature by using Cu Kα radiation (40 kV, 30 mA). Scanning electron microscope (SEM) images of the samples were captured by a JEOL JSM-890. Transmission electron microscopy (TEM) images were taken by a JEOL JEM-2100F at 200 kV. Diffuse reflectance (DR) UV-visible spectra of the samples were measured by a JASCO V-670 where $BaSO_4$ was utilized as the reference. The Tauc plot was employed to estimated the band gap value.[58] The BET specific surface area was recorded by a Quantachrome Monosorb MS-21 using the amount of N_2 adsorbed on the surface of the sample at 77 K. The Cl concentration remaining on the KTO surface were determined by X-ray fluorescence on an EDX-8000 (Shimadzu).

3.2.3. Photocatalytic activity tests

Examination of photocatalytic activity of the samples for the PSRM were performed in a fixed bed flow reactor as shown in Figure 3.1.[19] A certain amount of Rh/KTO powder was inserted to the Newton press and pressed to become a pellet. The pressure was set to be 40 MPa and held for 1 min before release the pressure. The obtained pellet then crushed by an alumina mortar. To obtained homogeneous granule size, the crashed pellet was screened using 25 and 50-mesh sieves and the granule over the 50-mesh (0.6 g) was introduced to the quartz reactor (60×20×1 mm^3) and half

occupied the reactor.

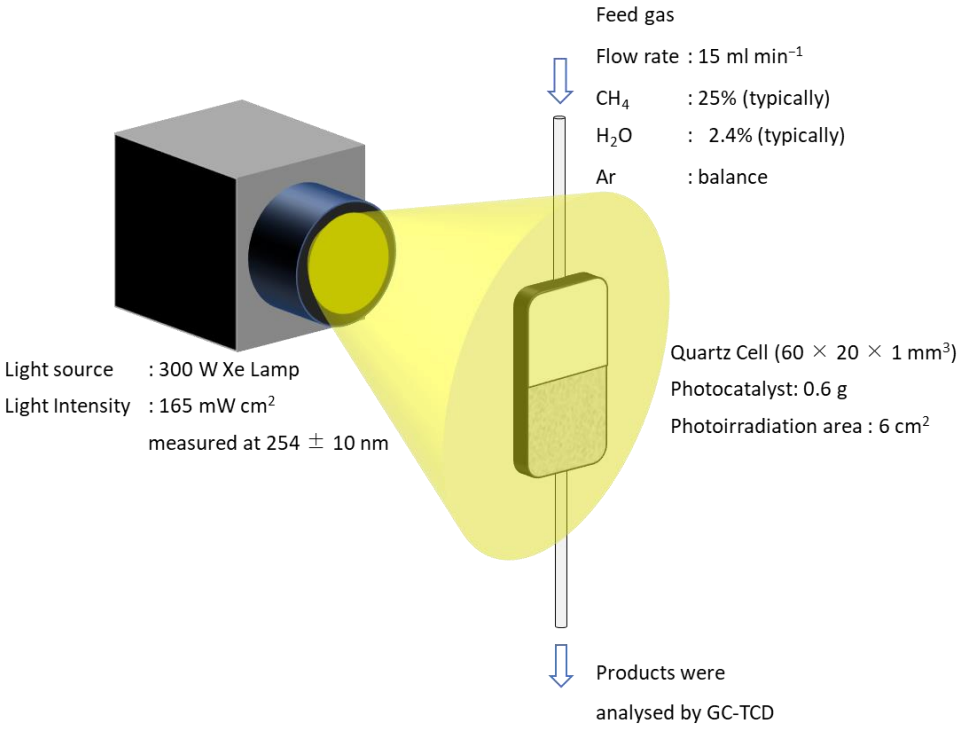

Figure 3.1 Scheme of the flow reactor employed in the photocatalytic reaction test for PSRM

To perform the reaction, the reactant gas which consisted of CH_4 (25%), H_2O (2.4 %), and argon as carrier were flown in 15 ml min^{-1}. The light was irradiated from a 300 W xenon lamp (PE300BUV) without additional optical filter. The area irradiated by the light was 6 cm^2. The light intensity used for the reaction was 165 mW cm^{-2} when measured in the UV range (254±10 nm). Due to photoirradiation, the temperature of the reactor surface was increased to 323 K. The gaseous products such as H_2 and CO_2 were collected in the sampling loop (18.5 mL) and analysed by an online gas chromatograph equipped with a thermal conductivity detector (Shimadzu, GC-8A, TCD). The interval of every sampling was ca. 30 min. Since the CO_2 sensitivity in the argon carrier gas was low, the experimental error for the determination of CO_2 was relatively large. In this reaction, the ratio of photoexcited electrons and holes consumed for the production, $R(e^-/h^+)$ was calculated according to eq. 2 from the production rates of H_2

and CO_2 as reductive and oxidative products, R_{H2} and R_{CO2}, respectively. The value of $R(e^-/h^+)$ should be 1.0 if the reaction take place in a good stoichiometric balance.

$$R(e^-/h^+) = R_{H2}/(4\times R_{CO2}) \qquad (2).$$

3.3. Result and discussion

3.3.1. Variously prepared KTO photocatalysts

According to the literature [55] but employing a little higher temperature (1373 K), some KTO samples were prepared by the flux method with several fluxes and also the SSR method. Figure 3.2 shows the XRD patterns of the KTO(*flux*,50,1373) samples prepared by a flux method with NaCl, KCl, and $CaCl_2$ fluxes and the KTO(SSR,100,1373) sample prepared by a solid-state reaction method as well as the references. Among them, the KTO(KCl,50,1373) and KTO(SSR,100,1373) samples (Figure 3.2b and d) exhibited the diffraction pattern of $K_2Ti_6O_{13}$ phase (Figure 3.2e) without any other impurity phase. However, XRD patterns of the other two prepared samples seems different from that of $K_2Ti_6O_{13}$ phase. The pattern of the KTO(NaCl,50,1373) sample is closer to $Na_2Ti_6O_{13}$ (NTO) or a mixture of NTO and KTO, which is consistent with the previous report.[55] For the KTO($CaCl_2$,50,1373) sample, no diffractions from $K_2Ti_6O_{13}$ phase were detected while TiO_2 rutile and $CaTiO_3$ were seen as major and minor patterns, respectively (Figure 3.2c). This fact revealed that NaCl and $CaCl_2$ were not suitable for preparing KTO crystals as reported in the previous work.[55]

These samples were loaded by 0.03 wt% of Rh-cocatalyst and tested in the PSRM reaction. Figure 3.3A representatively shows the time course of the H_2 and CO_2 production rates with the Rh/KTO(KCl,50,1373) sample in the photocatalytic reaction test for the PSRM reaction. The gas mixture (25% CH_4, 2.4% H_2O, and 72.6% Ar) was fed at the flow rate of 15 ml min^{-1} around atmospheric pressure and mild temperature. In the initial 1.5 h, the production rate of H_2 gradually increased and became constant to be 16 μmol h^{-1} while the production rate of CO_2 was steady in 4 μmol h^{-1}. The photocatalytic reaction continuously proceeded at least for 4 hours. Other gaseous oxidation products such as ethane and CO was not detected by the online GC−TCD and

the ratio of photoexcited electrons and holes consumed for the production was almost unity, $R(e^-/h^+)=1$, suggesting that the products were only H_2 and CO_2. As the blank tests, the experiments were carried out without light irradiation and without the photocatalyst, which provided no products. These results indicate that the reaction occurred photocatalytically.

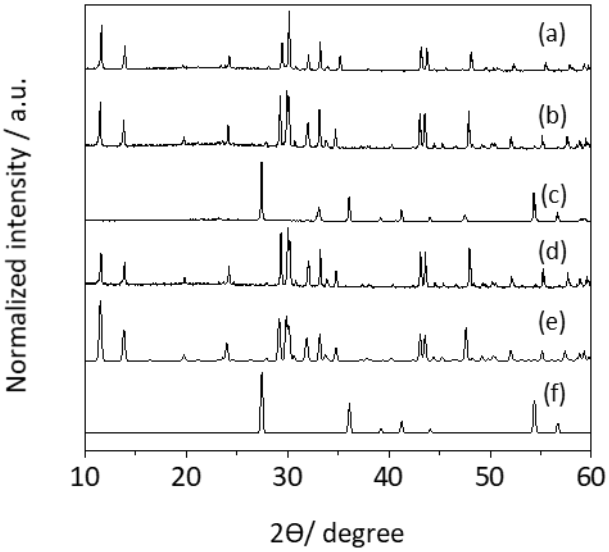

Figure 3.2 XRD pattern of the prepared KTO(*flux*,50,1373) and KTO(SSR,100, 1373) samples, (a) KTO(NaCl,50,1373), (b) KTO(KCl,50,1373), (c) KTO($CaCl_2$,50,1373), and (d) the KTO(SSR,100,1373) sample, and references, (e) $K_2Ti_6O_{13}$ (ICSD #25712) and (f) rutile-TiO_2 (ICSD#9161). The concentration of substrate in the molten mixture in the preparation by the flux method was 50%. The temperature applied for calcinating sample was set to be 1373 K with holding time was 10 hours. The intensity of the diffraction patterns was normalized by dividing with the highest peak of each sample.

Figure 3.3B shows the photocatalytic activity of the samples that were prepared by various flux and loaded by 0.03 wt% of Rh-cocatalyst. The highest photocatalytic activity was obtained by the KTO(KCl,50,1373) sample, indicating that the $K_2Ti_6O_{13}$ crystal without any impurity phases was better for the PSRM reaction. Moreover, the KTO(SSR,100,1373) sample, prepared by the solid-state reaction, exhibited a bit lower

photocatalytic activity in the PSRM reaction than the KTO(KCl,50,1373) sample, suggesting that the fabrication of the KTO crystal by the flux method contributed to the increase of the activity. On the other hand, the sample prepared by a NaCl flux exhibited lower photocatalytic activity, which would be due to its impurities. In addition, the sample prepared by a $CaCl_2$ flux, consisting of TiO_2 and $CaTiO_3$, performed the lowest activity suggesting the KTO phase would contribute to the high performance. For this reason, in the further investigation, only the KCl flux was used for the preparation in the flux method and the flux will be omitted from the sample name.

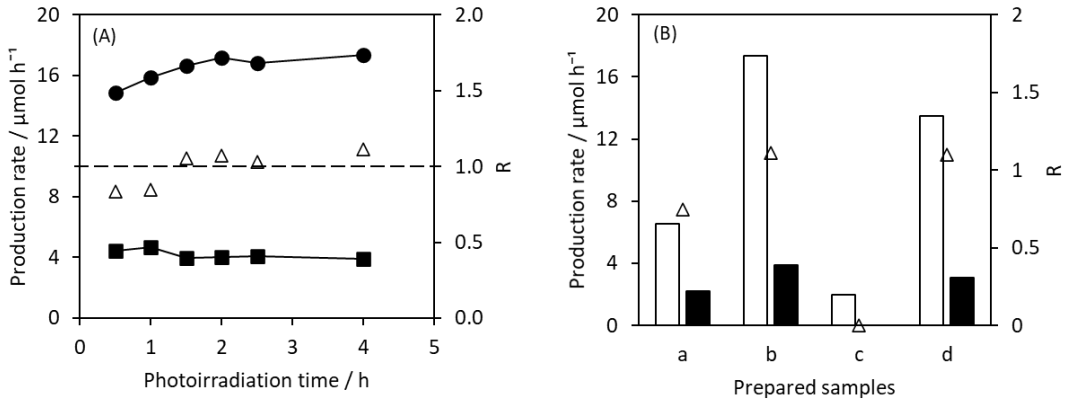

Figure 3.3 (A) Time course of the production rates of H_2 (filled cirle) and CO_2 (filled squares) over the Rh/KTO(KCl,50,1373) sample. (B) Production rates of H_2 (white bar) and CO_2 (black bar) in the PSRM, and the consumed electron/hole ratio calculated from the production rates, $R(e^-/h^+)$ (open triangle), over the prepared KTO(flux,50,1373) and KTO(SSR,100,1373) samples, (a) KTO(NaCl,50,1373), (b) KTO(KCl,50,1373), (c) KTO($CaCl_2$,50,1373), and (d) the KTO(SSR,100,1373) sample. The photocatalyst granule used was 0.6 g. The reactant gas mixture (25% CH_4, 2.4% H_2O, and 72.6% Ar) was introduced at the flow rate of 15 ml min^{-1}. The irradiation area was 6.0 cm^2. The light intensity used was 165 mW cm^{-2} when measured at 254±10 nm in wavelength. Products were sampled at 4 hours later after starting photoirradiation.

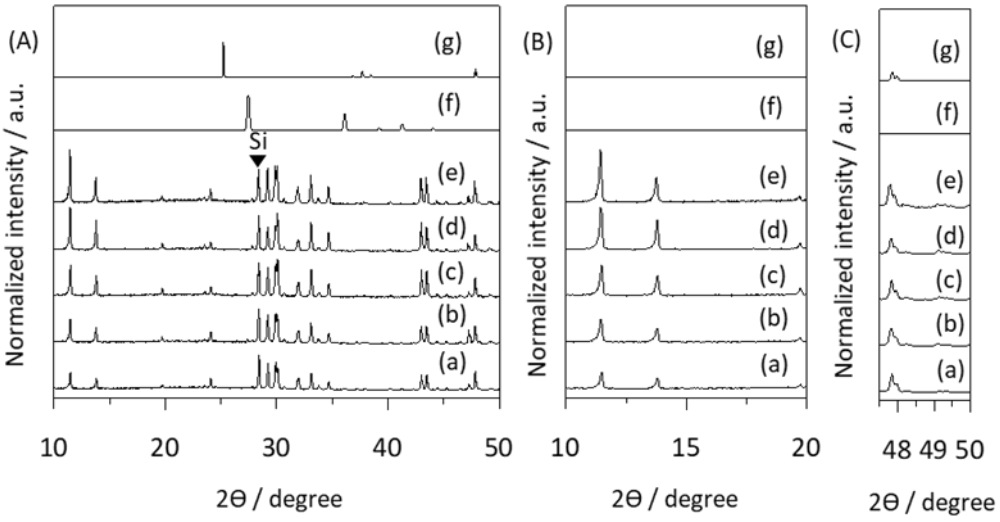

Figure 3.4 XRD patterns of various KTO(*x*,1373) samples prepared with the KCl flux and a sample prepared by SS method mixed with 10wt% of silicon powder, (A) the overview, (B) the low angle, and (C) the high angle. The samples are (a) KTO(SSR, 100,1373), (b) KTO(90,1373), (c) KTO(50,1373), (d) KTO(30,1373), and (e) KTO(10,1373). (f) TiO_2 rutile and (g) TiO_2 anatase are shown as references. The intensity of sample was normalized by dividing with the Si peak.

It is known that the solute concentration in the molten mixture can regulate the growth rate of KTO crystal and change its photocatalytic activity for water splitting, CO_2 reduction, and methane steam reforming.[19,24,25,34,55] Here, in the present work, the author prepared various solute concentrations in the KCl flux and investigated the structure and the photocatalytic activity in the PSRM reaction. As shown in Figure 3.4A, no impurities were detected in the XRD patterns, which also has been confirmed in the previous reports.[34,55] The difference of intensities in certain 2ϑ, i.e., 11.5° and 48° (Figure 3.4B and C), could be originated from the growth rate difference in the specific facet of the KTO crystal due to the difference of the solute concentration in the molten KCl flux. In contrast, the SEM images (Figure 3.5) show that the morphology of the samples was shifted gradually from granular polygonal-like particles to fine and straight long rod-like particles as the solute concentration changed from 100% (without a flux) to 10%. Lower

solute concentration provided more molten salt in the mixture which would ease the crystal nuclei to move and growth in the certain direction according to the crystal habit of $K_2Ti_6O_{13}$. As a result, the KTO crystal obtained in lower solute concentration has larger and longer particle as well as finer facets. By TEM measurement of the Rh/KTO(10,1373) sample, a rod-like particle was observed with a length of ca. 1 μm(Figure 3.6A), which is consistent with the SEM image (Figure 3.5e). The electron diffraction of the KTO particle provided a single diffraction pattern (Figure 3.6B) in several spots. This result indicates that the observed rod-like particle was a single crystal.

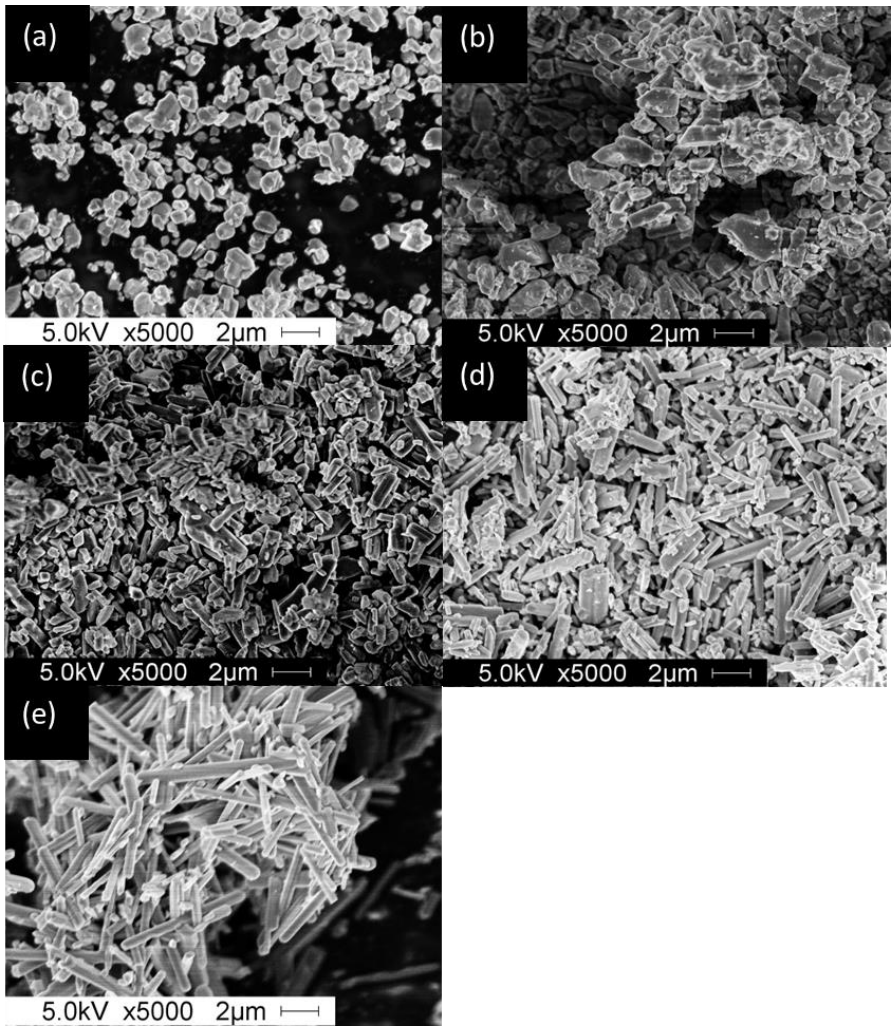

Figure 3.5 SEM images of various Rh/KTO(*x*,1373) samples, where *x* was the solute concentration in mol.%, (a) Rh/KTO(SSR,100,1373), (b) Rh/KTO(90,1373), (c) Rh/KTO(50,1373), (d) Rh/KTO(30,1373), and (e) Rh/KTO(10,1373).

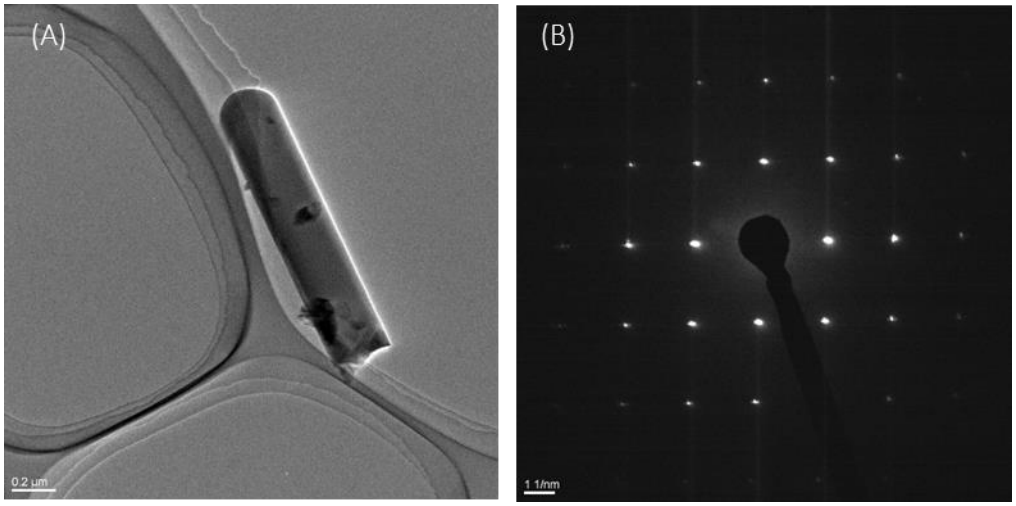

Figure 3.6 (A) TEM image and (B) electron diffraction pattern of the Rh/KTO(10,1373) sample.

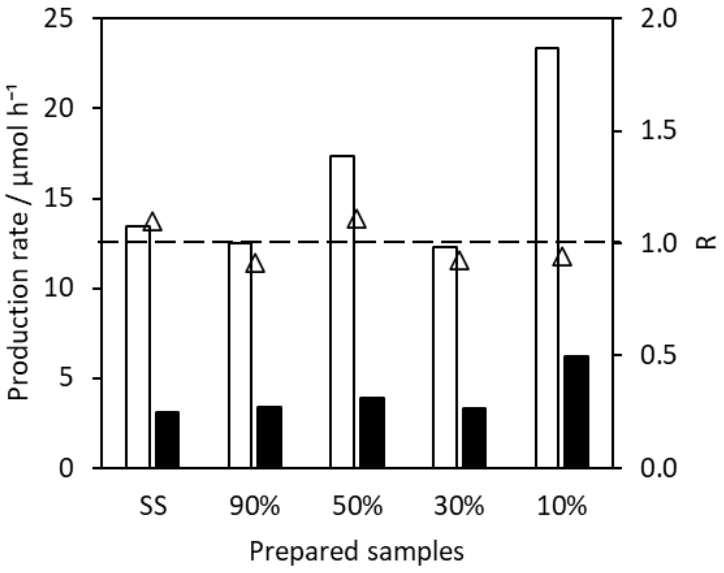

Figure 3.7 Production rates of H_2 (white bar) and CO_2 (black bar) in the photocatalytic reaction test for the PSRM reaction, and the consumed electron/hole ratio calculated from the production rates, $R(e^-/h^+)$ (open triangle), over the Rh/KTO(*x*,1373) samples. The reaction conditions are the same as those mentioned in the caption of Figure 3.3.

Figure 3.7 shows the photocatalytic activities of these samples. As shown, the photocatalytic activity was varied with the difference of the solute concentration and

the highest production rates of H_2 and CO_2 were obtained by the sample prepared with the lowest solute concentration, i.e., the Rh/KTO(10,1373) sample. These results indicates that the proper morphology was an essential factor in enhancing photocatalytic activity.

However, it is well known that the photocatalyst structural properties such as surface area, crystal size, and so on were also considered as the essential factors to affect the photocatalytic activity. Thus, to investigate more profound, the effects of the heating temperature and the solute concentration were investigated with the KTO(10,*y*) and KTO(*x*,1173) samples. No impurity phases in the XRD patterns were found for the entire KTO(10,*y*) and KTO(*x*,1173) samples (Figure 3.8). The morphology also did not change with variating the heating temperature (Figure 3.9). On the other hand, the crystal size and specific surface area changed (Table 3.1, entries 1,4,7,10–13).

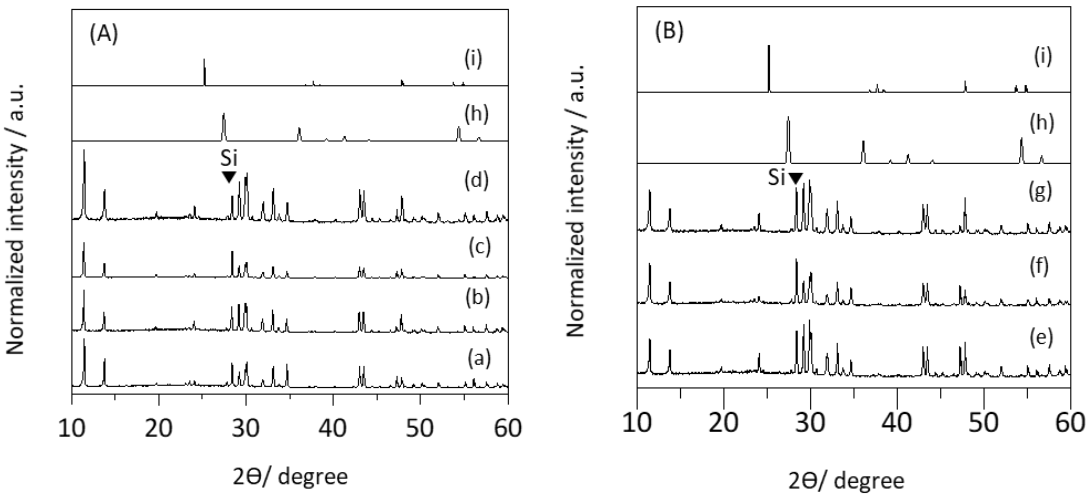

Figure 3.8 (A) XRD patterns of the samples prepared at various temperatures mixed with 10 wt% of Si as an internal standard, (a) KTO(10,1473), (b) KTO(10,1373), (c) KTO(10,1273), and (d) KTO(10,1173), and those of (h) TiO_2 rutile and (i) TiO_2 anatase as the reference, and (B) those of the samples prepared with various solute concentrations mixed with 10 wt% of Si as internal standard, (e) KTO(SSR,100,1173), (f) KTO(50,1173), and (g) KTO(30,1173), and those of (h) TiO_2 rutile and (i) TiO_2 anatase as a reference. The intensity of sample was normalized by dividing with the Si peak.

Table 3.1 Structural and optical properties of the prepared samples and their photocatalytic activity in the PSRM reaction.

Entry	Sample	Particle size (SEM)[a]/ μm		Aspect ratio[b]	S_{BET}[c] / m^2 h^{-1}	Band gap[d]/ eV	Production rate[e]/ μmol h^{-1}		$R(e^-/h^+)$[f]
		Length (long side)	Thickness (short side)				H_2	CO_2	
1	Rh/KTO(SSR,100,1173)	0.90	0.62	1.4	4.0	3.33	21	5.5	1.0
2	Rh/KTO(SSR,100,1373)	1.12	0.79	1.4	2.5	3.31	13	3.1	1.1
3	Rh/KTO(90,1373)	1.36	0.69	2.0	5.1	3.33	12	3.5	0.9
4	Rh/KTO(50,1173)	0.85	0.21	4.1	10.2	3.36	29	7.1	1.0
5	Rh/KTO(50,1373)	1.52	0.49	3.1	6.2	3.34	17	3.9	1.1
6	Rh/KTO(30,1073)	0.64	0.09	7.0	16.1	3.35	29	7.1	1.0
7	Rh/KTO(30,1173)	0.95	0.19	5.1	13.3	3.35	30	7.5	1.0
8	Rh/KTO(30,1273)	1.96	0.45	4.3	5.4	3.35	18	5.3	0.9
9	Rh/KTO(30,1373)	2.81	0.49	5.7	5.2	3.34	12	3.3	0.9
10	Rh/KTO(10,1173)	2.13	0.24	8.8	10.7	3.33	23	5.7	1.0
11	Rh/KTO(10,1273)	2.08	0.32	6.5	9.3	3.37	23	6.7	0.9
12	Rh/KTO(10,1373)	4.58	0.59	7.8	5.4	3.32	23	6.1	0.9
13	Rh/KTO(10,1473)	5.22	0.74	7.1	4.3	3.29	14	4.2	0.8
14	Rh/KTO(30,1173)1h	0.93	0.16	5.8	13.2	3.35	29	6.6	1.1
15	Rh/KTO(30,1173)ana	1.64	0.21	7.7	11.0	3.36	19	4.4	1.1
16	KTO(SSR,100,1373)	1.12	0.79	1.4	4.0	3.31	0.3	n.d	-

[a] Average particle size measured from the SEM images. [b]Aspect ratio calculated from dividing length/thickness. [c] Specific surface area measured by a BET method. [d] Band gap calculated from the DR UV-Vis spectra. [e]Sampling was carried out 4 hours later after starting irradiation. [f] Ratio of electrons and holes consumed for the products formation.

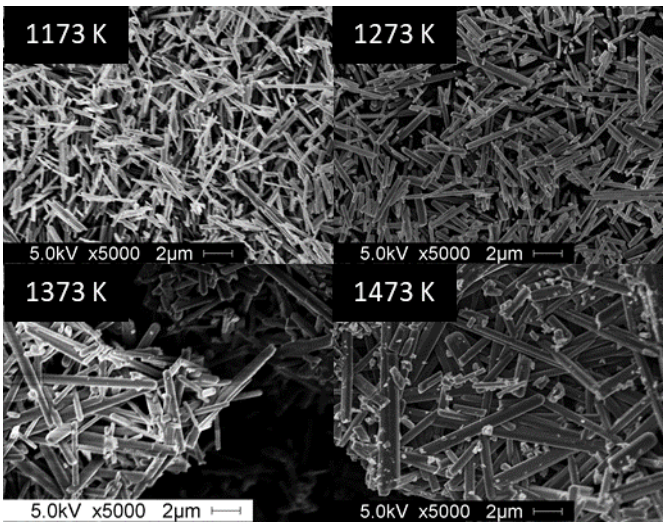

Figure 3.9 SEM images of the KTO(10,*y*) samples, where *y* was varied from 1173 K to 1473 K.

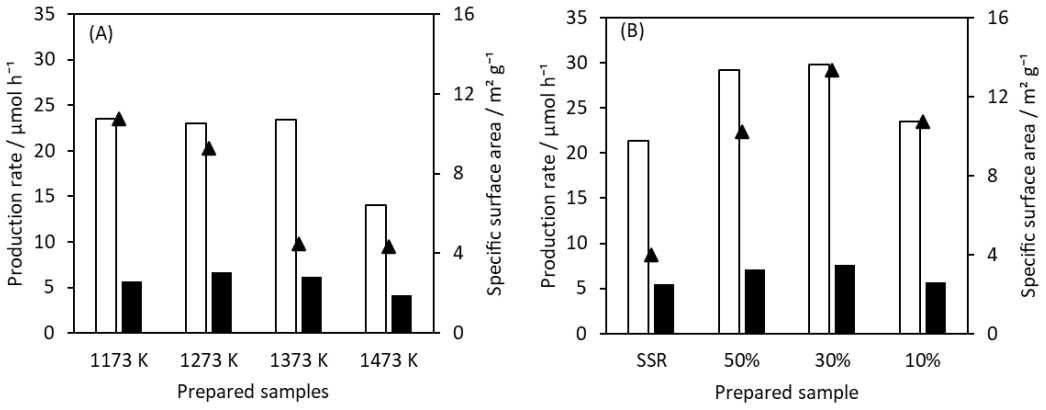

Figure 3.10 Production rates of H_2 (white bar) and CO_2 (black bar), and the specific surface area (filled triangle) of (A) various Rh/KTO(10,*y*) samples and (B) various Rh/KTO(*x*,1173) samples. The reaction conditions are the same as those mentioned in the caption of Figure 3.3.

Figure 3.10 shows the photocatalytic activities and the specific surface area of these samples. The photocatalytic activity of various Rh/KTO(10,*y*) samples were similar

except for the Rh/KTO(10,1473) sample (Figure 3.10A). The low activity of the Rh/KTO(10,1473) sample could be corresponded to the low specific surface area, i.e., a decrease of the active sites for the reaction, or the possible presence of small amount of TiO_2 or defects due to evaporation of potassium at high temperature.[55] However, the sample prepared in 1373 K performed similar activity with the higher surface area samples such as the Rh/KTO(10,1173) and Rh/KTO(10,1273) samples even the specific surface area was small. Other parameters compensating the low surface area, such as crystal growth, should also affect the photocatalytic activity since the surface area could not independently explain the phenomena. In the previous study, it was suggested that larger fine crystal size of the photocatalysts such as $NaTaO_3$ and $Na_2Ti_6O_{13}$ performed higher photocatalytic activity in the PSRM due to the well-grown crystals that would have less crystal defects and large photoabsoption area.[19,25] Thus, in the present study, even the surface area of the KTO(10,1373) sample was lower than the KTO(10,1173) and KTO(10,1273) samples, the well-grown crystals at moderate temperature compensated the decrease of the photocatalytic active sites. The result indicated that the completeness of crystals and high surface area can contribute to the photocatalytic activity.

On the other hand, when the solute concentration was varied in the lower heating temperature such as 1173 K, the trend of the photocatalytic activity was different from that over the samples prepared at higher heating temperature such as 1373 K, i.e., the highest H_2 and CO_2 production rates were obtained by the Rh/KTO(30,1173) sample as shown in Figure 3.10B. The surface area or the proper morphology could be considered as the vital factor for enhancing the photocatalytic activity in the samples prepared at lower temperature. Thus, another series of the KTO(30,*y*) samples were further prepared for searching the optimum photocatalytic activity of the Rh/KTO photocatalysts by variating the heating temperature, holding time, and different TiO_2 precursors.

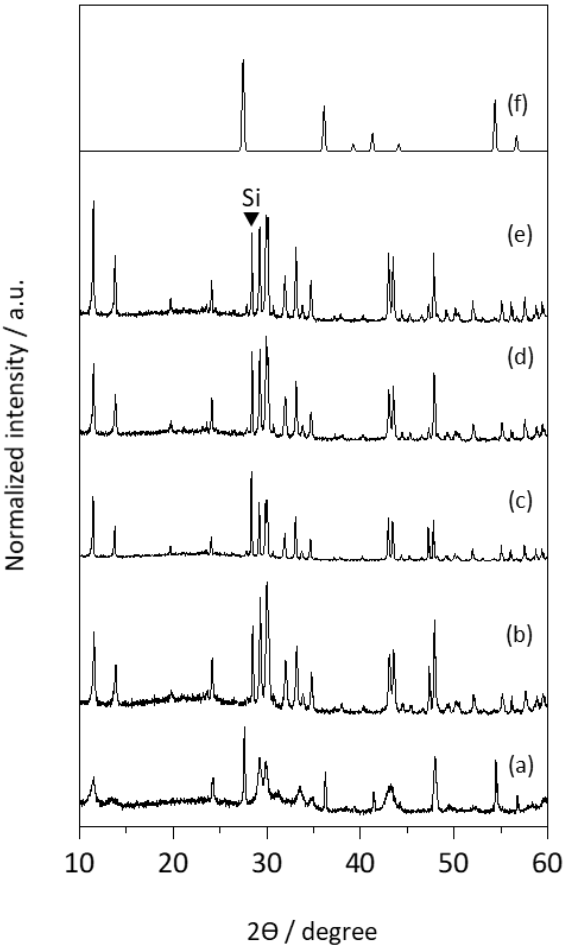

Figure 3.11 XRD patterns of the various KTO(30,*y*) samples mixed with 10 wt% of Si as internal standard, (a) KTO(30,973), (b) KTO(30,1073), (c) KTO(30,1273), (d) KTO(30,1173)1h, (e) KTO(30,1173)ana, and (f) TiO_2 rutile. The intensity of sample was normalized by dividing with the Si peak.

The Rh/KTO(30,*y*) samples were prepared at lower heating temperature such as 973–1273 K. As shown in Figure 3.11, except the KTO(30,973) sample, no other impurity phases were recorded in the diffractograms. Some TiO_2 rutile peaks were recorded for the KTO(30,973) sample. Since the melting point of pure KCl is 1043 K, the crystal growth of KTO was not completed at 973 K in the present conditions, consisting with literatures [34,59] while the precursors were wholly transformed to KTO at 1073 K. The structural

properties are listed in Table 3.1, entries 6–9. The photocatalytic activity and the specific surface area of these Rh/KTO(30,*y*) samples are depicted in Figure 3.12a–d. As shown, the photocatalytic activity of the Rh/KTO(30,1073) sample (Figure 3.12a) are similar to that of the Rh/KTO(30,1173) sample (Figure 3.12b) even the specific surface area was different. Higher surface area provided more active sites but at the same time smaller crystal size also would give more surface defect sites that reduce the photocatalytic activity. Moreover, the samples prepared at higher temperature such as the Rh/KTO(30,1273) and Rh/KTO(30,1373) samples (Figure 3.12c and d) exhibited lower activity probably due to their very low surface area.

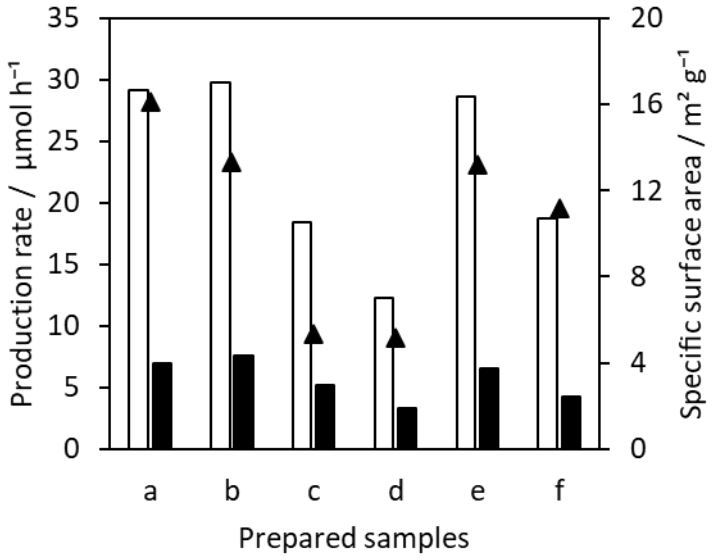

Figure 3.12 Production rates of H_2 (white bar) and CO_2 (black bar), and the specific surface area (filled triangle) of the Rh/KTO(30,*y*) samples, (a) Rh/KTO(30,1073), (b) Rh/KTO(30,1173), (c) Rh/KTO(30,1273), (d) Rh/KTO(30,1373), (e) Rh/KTO(30,1173)1h, and (f) Rh/KTO(30,1173)ana. The reaction conditions are the same as those mentioned in the caption of Figure 3.3.

In the previous report, it was suggested that the appropriate holding time could provide well formed KTO crystal and shorter heating time such as 1 h was not enough to synthesized the pure KTO.[55] However, in the present experiment, the result seems to

be different probably due to the detailed conditions such as different crucible used and mixing preparation as mentioned before. For the sample with a short time holding temperature, i.e, the KTO(30,1173)1h sample, the KTO crystal still also formed well (Figure 3.11d), which was the similar crystal size to the KTO(30,1173) sample in the standard conditions (10 h holding at 1173 K) as shown in the Table 3.1, entries 7 and 14. The photocatalytic performance of the KTO(30,1173)1h sample was also similar to the KTO(30,1173) sample (Figure 3.12 b and e). These facts indicate that such a short holding time was enough to synthesize potassium hexatitanate even at lower temperature, i.e., 1173 K. This result also revealed that the heating duration more than 1 h in the molten flux was not an essential factor for nucleation and crystal growth of KTO. The crystal size should be determined by the other variables such as the cooling rate.

As shown in Table 3.1, entries 7 and 15, the KTO(30,1173) samples prepared from different TiO_2 polymorphs, it was obvious that the crystal size of the sample prepared from TiO_2 anatase was bigger than that from rutile even though the anatase precursor has much smaller particles; the specific surface area of anatase and rutile samples used here were 300 and 2.5 $m^2 g^{-1}$, respectively. Since TiO_2 anatase in the KCl flux might be more reactive than rutile one, the crystal growth with the anatase precursor would be well enhanced, resulting a bigger crystal size. Wang et al. reported that potassium hexatitanate whisker could be perfectly produced through a hydrothermal method in the lower temperatures around 523 K by utilizing TiO_2 anatase as starting material while from TiO_2 rutile it was only partially produced.[60] Fujiki and Izumi reported that KTO fiber which was synthesized in tungsten flux method using smaller anatase particles as the precursor, was longer than that prepared from the rutile-TiO_2 precursor of larger particle size.[61] The same effect might occur in the present case using the KCl flux. The present result was opposite to the case of the previous study on sodium titanate,[33] i.e., smaller rod sodium titanate crystal was produced by utilizing TiO_2 anatase (300 $m^2 g^{-1}$) compared to rutile (2.5 $m^2 g^{-1}$) precursor. This crystallization chemistry requires more systematic study. As for the photocatalytic activity (Figure 3.12 b and f), the sample prepared from anatase exhibited lower activity, which would be

originated from larger crystal size and lower specific surface area.

The effect of the rhodium cocatalyst loading was also confirmed by using the KTO(SSR,100,1373) sample. The production rates of H_2 and CO_2 with the bare KTO(SSR,100,1373) sample was 0.3 and 0 μmol h^{-1}, respectively (Table 3.1 entry 16). As shown, the Rh/KTO(SSR,100,1373) sample produced H_2 with the production rate of 13 μmol h^{-1} (Table 3.1 entry 2), which is more than 40 times higher than the bare KTO(SSR,100,1373) sample. The presence of Rh cocatalyst on the surface is considered to enhance the charge separation thus increase photocatalytic activity.[22,25]

In the present study, chloride salt and $RhCl_3$ were used for the sample preparation. Since residual Cl anion may affect the photocatalytic activity, the author measured the Cl content in the representative samples by using XRF measurement and the results are shown in the Table 3.2. The presence of Cl anion was elucidated on some of the samples although the concentrations were very low. As a result, no clear relationship between the Cl content and the photocatalytic activity was noticed, suggesting that the influence of the residual Cl anions on the photocatalytic activity should be very limited.

Table 3.2 Amount of Cl anion residue in the sample determined by XRF measurement.

Entry	Sample	Cl content (%wt)
1	KTO(SSR,100,1173)	0.00
2	Rh/KTO(30,1173)	0.01
3	Rh/KTO(30,1373)	0.01
4	Rh/KTO(10,1173)	0.00
5	Rh/KTO(10,1373)	0.00

Among the Rh/KTO(*x*,*y*) samples listed in Table 3.1, the samples, Rh/KTO(50,1173), Rh/KTO(30,1173), Rh/KTO(30,1173)1h, and Rh/KTO(30,1073), showed almost similar

photocatalytic activity with the highest H_2 production rate such as 29, 30, 29, and 29 μmol h^{-1}, respectively. Among them, the Rh/KTO(30,1173) sample gave the highest activity, i.e., the methane conversion was 0.081% and the apparent quantum efficiency was 0.15%.

3.3.2. Relation between structure and photocatalytic activity

Here, the photocatalytic activity of the two series of the prepared samples will be discussed, i.e., the Rh/KTO(*x*,1173) and Rh/KTO(*x*,1373) samples, which were prepared with various solute concentrations in the molten mixture with a KCl flux. As shown in Figure 3.13, among the Rh/KTO(*x*,1173) samples the suitable solute concentration was 30–50%; the Rh/KTO(30,1173) and Rh/KTO(50,1173) samples exhibited the highest photocatalytic activities. On the other hand, in the higher heating temperature at 1373 K, the most active sample was the Rh/KTO(10,1373) sample prepared with the low solute concentration. These results indicate that the solute concentration could affect the photocatalytic activity of KTO samples. When high heating temperature (1373 K) was applied, the lower solute concentration produced finer KTO crystals thus enhance the photocatalytic activity. In contrast, when the low heating temperature utilized, the other structural properties such as surface area and the crystal thickness gave more impact to control the photocatalytic activity compared to the fine crystals. Thus, it is proposed that the solute concentration could regulate the photocatalytic activity of the sample by control the structural properties of KTO, but the other factors also must be considered.

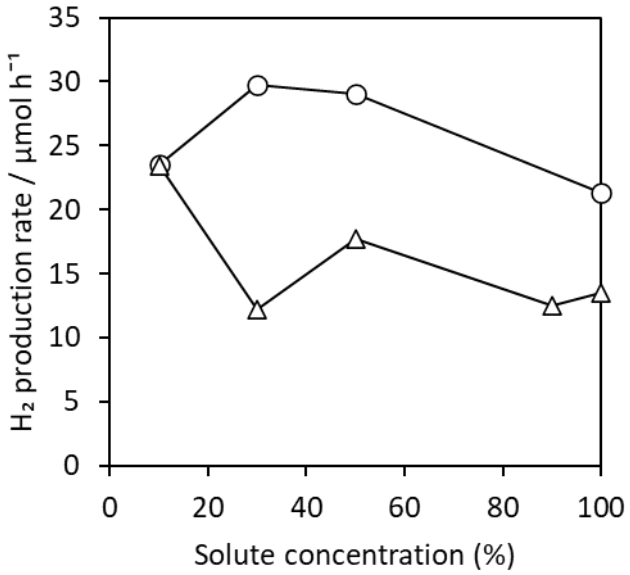

Figure 3.13 Hydrogen production rate over various Rh/KTO samples prepared by flux method in various solute concentrations and different heating temperatures of 1173 K (open circle) and 1373K (open triangle). The reaction conditions are the same as those mentioned in the caption of Figure 3.3.

Furthermore, the heating temperature also seems to have a critical effect on enhancement of photocatalytic activity. As shown in Table 3.1, the Rh/KTO(30,*y*) samples prepared at lower temperatures, i.e., Rh/KTO(30,1073) and Rh/KTO(30,1173), exhibited better photocatalytic activity compared to the others such as Rh/KTO(30,1273) and Rh/KTO(30,1373). The lower heating temperature produced smaller crystal size, shorter rod crystal, thinner short facet, and thus higher specific surface area. To further investigate the critical parameters in the PSRM, the H_2 formation rate was plotted against some parameters (Figure 3.14). The specific surface area had a moderately positive correlation to photocatalytic activity, while crystal thickness had a negative one. Since the increase in thickness would lead to a decrease in the specific surface area, it would be reasonable to consider that a larger surface area gives the larger adsorption of substrates and thus increases the rate of H_2 production. Yoshida's group previously reported that smaller potassium hexatitanate crystals could

produce more H_2 in overall water splitting by UV-light, which is a similar trend to the present work.[34] On the other hand, in the present reaction system, the H_2 production rates differed by a factor of up to two for the samples with similar specific surface areas, strongly suggesting that other parameters such as crystal length and crystal thickness also affect catalytic performance (Figure 3.14) since the long and short facets contribute to the reductive and oxidative reactions, respectively.[38]

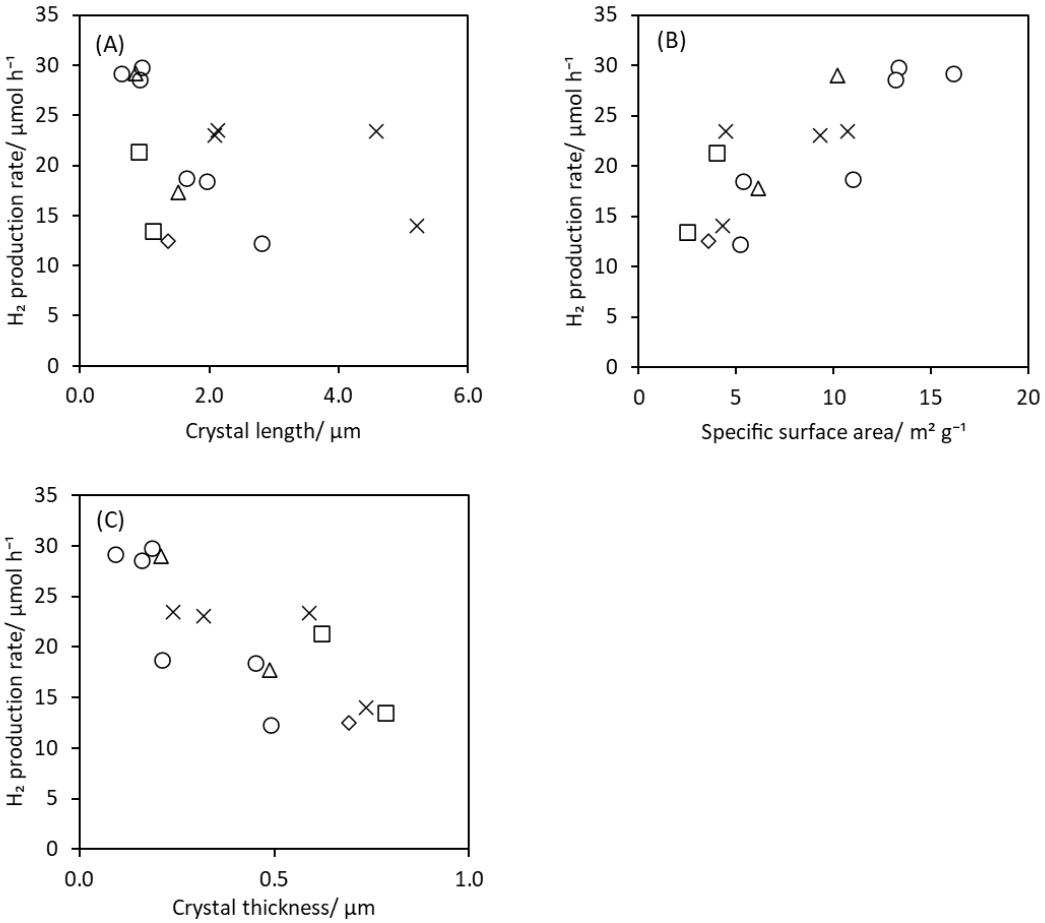

Figure 3.14 Correlation between H_2 production rates with (A) crystal length, (B) specific surface area, and (C) the crystal thickness of entire Rh/KTO(*x*,*y*) samples. Square: Rh/KTO(SSR,100,*y*), diamond: Rh/KTO(90,*y*), triangle: Rh/KTO(50,*y*), circle: Rh/KTO(30,*y*), and cross: Rh/KTO(10,*y*). The hydrogen production rate was evaluated after 4 hours later from the start of photoirradiation.

3.3.3. Effect of granulation

In the present system using a fixed bed reactor, first a powdery photocatalyst sample consisting of micrometer-sized fine crystals was conventionally pressed under 40 MPa and then crashed into millimetres-sized granules (25–50 mesh) before introducing it to the reactor. The granule form can help us to introduce the photocatalyst into the thin reaction cell and realize the smooth gas flow in the reaction cell. However, one may consider that the pressing and crashing might make some damages on the KTO fine crystals, which might produce many cracks and defects and enhance the recombination of the photoexcited electrons and holes. Thus, in the present study, the Rh/KTO granule samples prepared by pressing at various pressures from 20–60 MPa were compared with the original powder sample. Although the required weight to fill the reactor was different between the granule and powder samples, the photo-irradiated area was arranged to be the same as the usual conditions to be 6 cm^2.

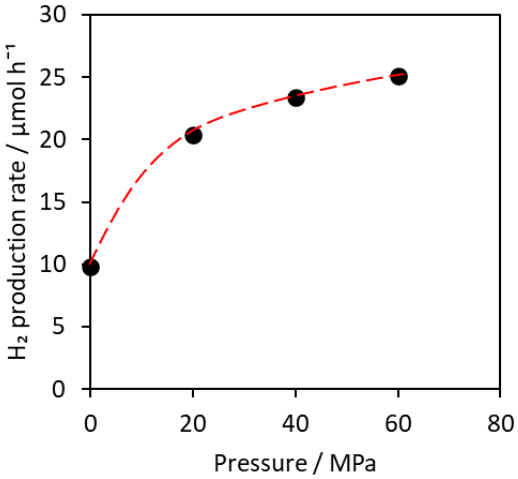

Figure 3.15 H_2 production rate of the powder (0 MPa) and granule (20-40 MPa) Rh/KTO(10,1373) samples, where the catalyst weights were 0.34, 0.45, 0.62, and 0.67 g, respectively to regulate the photoirradiation area as 6 cm^2. The reactant gas mixture (25% CH_4, 2.4% H_2O, and 72.6% Ar) was introduced at the flow rate of 15 ml min^{-1}. The light intensity used was 165 mW cm^{-2} when measured at 254 ± 10 nm in wavelength. Products were sampled at 3 hours later after starting photoirradiation.

Figure 3.15 shows the relationship between pressures to prepare the granules and the H_2 formation rate. In powder form, the H_2 production rate was relatively low (9.2 μmol h^{-1}). On the other hand, the photocatalytic performance increased significantly by 2.1–2.6 times by making the granules at a pressure of 20–60 MPa compared to the original powder sample. By pressing at higher pressures, the amount of the KTO photocatalyst in the reactor increased (Table 3.3).

Table 3.3 H_2 production rate of the powder (0 MPa) and granules (20-60 MPa) of the Rh/KTO(10,1373) sample

Entry	Pressing pressure[a] / MPa	Weight[b] / g	SSA[c] / m^2 g^{-1}	H_2 production rate[d] / μmol h^{-1}
1	0	0.34	5.2	9
2	20	0.45	6.5	19
3	40	0.62	6.6	22
4	60	0.67	6.8	24

[a] The pressure used for making the granules. [b] Amount of photocatalyst inserted to the cell to occupy the same area (6 cm^2). [c] Specific surface area measured by a BET method. [d] The production rates at 3 hours after starting irradiation.

To investigate the effect of the sample amount on the photocatalytic activity, the H_2 formation rate was divided by the sample weight and plotted with the pressure (Figure 3.16). The H_2 formation rate per weight on the granule sample were higher than that on the original powder one by 1.3–1.5 times. The advantage of the granule sample was also confirmed even when the activity was divided by the sample amount. Note that there would be no large difference in the number of the absorbed photons between the powder and granule KTO samples because KTO samples had similar absorption properties and no light was transmitted through the sample due to the absorption and scattering by the samples. To investigate the effect of the sample amount in detail, the photocatalytic activity of the KTO samples diluted by quartz sands was investigated,

where the quart sands were selected as a diluent because it is transparent to UV light and inactive for the PSRM reaction. In this experiment, the irradiation area was arranged to be 6.0 cm^2 as in the above case. The photocatalytic activity was almost the same as the original one, even by decreasing the amount of KTO to 35wt% (Table 3.4). This result suggested that the number of absorbed photons is not changed largely by the dilution of the quarts and the irradiated photon number almost determined the H_2 formation rate. More importantly, the amount of the photocatalysts has no significant effect on the photocatalytic activity in the present conditions, also suggesting that the sample amount would not affect the photocatalytic activity largely in the comparison between powder and granule samples. Pressing would increase the contact between the KTO crystals based on the SEM images of the granule sample (Figure 3.17). The increased contact might have a positive effect on the photocatalytic activity possibly due to the improved interparticle electron transfer as illustrated in Figure 3.18.

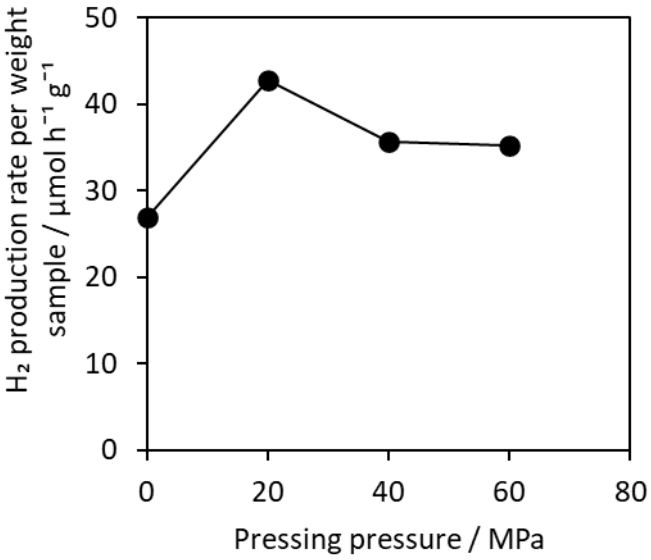

Figure 3.16 H_2 production rate per sample weight of the powder (0 MPa) and granules (20-60 MPa) Rh/KTO(10,1373) sample. The reactant gas mixture (25% CH_4, 2.4% H_2O, and 72.6% Ar) was introduced at the flow rate of 15 ml min^{-1}. The irradiation area was 6.0 cm^2. The light intensity used was 165 mW cm^{-2} when measured at 254±10 nm in wavelength. Products were sampled at 3 hours later after starting photoirradiation.

Table 3.4 H_2 production rate over the Rh/KTO(10,1373) powder sample in different weight[a]

Entry	Sample	Amount of photocatalysts[b]/ g	Production rate[c] / μmol h^{-1}	
			H_2	CO_2
1	Rh/KTO(10,1373) diluted by quartz granules	0.13	9.0	2.32
2	Rh/KTO(10,1373)	0.38	9.8	2.35

[a] The photocatalysts powder was inserted to the cell to occupy the same area (6 cm^2). [b]Amount of photocatalyst used for the reaction. [c] The production rates at 3 hours after starting irradiation.

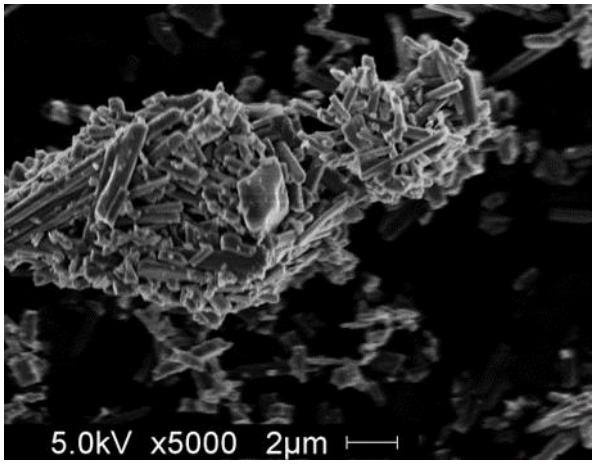

Figure 3.17 SEM images of the granule Rh/KTO(10,1373) sample.

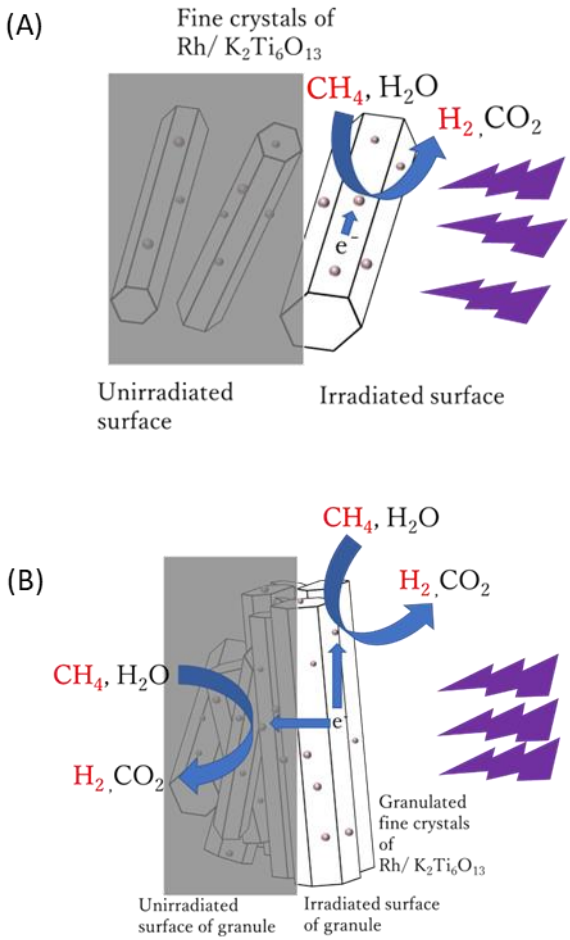

Figure 3.18 Illustrations of the Rh/KTO samples consisting of (a) the powdery fine crystals, and (b) the granulated fine crystals for the PSRM.

3.3.4. Reaction mechanism

Here is the proposed reaction mechanism of the PSRM over the Rh/KTO photocatalyst. First, the light is absorbed by the KTO crystals and photoexcited electrons and holes are produced. Then, the charge carriers migrated to the photocatalyst surface. Although the charge carriers recombined during transportation to the crystal surface in large portion, some of them can reach the surface and react with the reactants. The water and methane on the Rh/KTO surface would be activated by the holes to produce protons and radical surface intermediates such as methyl radicals and OH radicals.[62] The methyl radicals

would successively react with water or OH radicals to produce CO_2 while electrons would reduce the protons to H_2. In the case of the granule sample of Rh/KTO, the electrons can transport more easily between the particles than the powder sample, which might contribute to the effective charge separation and high photocatalytic activity.

3.4. Conclusion

Many rod-like fine KTO crystals covered with facets having various structural aspects were successfully synthesized by employing the flux method. The photocatalytic activity of the Rh/KTO samples varied with the KTO structure. The KTO crystals with larger surface area exhibited higher photocatalytic activity for the PSRM in the present conditions. Other factors such as crystal thickness also influenced on the photocatalytic activity. Among them the KTO(30,1173) sample prepared by rutile-TiO_2 precursor and KCl flux at 1173 K exhibited the highest photocatalytic activity after loading Rh cocatalyst. Furthermore, it was found that the granule of the Rh/KTO fine crystal sample showed 2.1-2.6 times higher activity than the original powdery fine crystals, which would result from the better intraparticle contact due to the pressing the fine crystals to get the granule form. Further optimization on the cocatalyst and the loading method would contribute to further development of the KTO photocatalyst.

References

1 E. Kikuchi, S. Uemiya and T. Matsuda, in *Studies in Surface Science and Catalysis*, eds. A. Holmen, K.-J. Jens and S. Kolboe, Elsevier, 1991, vol. 61, pp. 509–515.

2 E. Kikuchi, *Catal. Today*, 2000, **56**, 97–101.

3 J. Tong, Y. Matsumura, H. Suda and K. Haraya, *Ind. Eng. Chem. Res.*, 2005, **44**, 1454–1465.

4 C. S. Martavaltzi, E. P. Pampaka, E. S. Korkakaki and A. A. Lemonidou, *Energy Fuels*,

2010, **24**, 2589–2595.

5 X. Zhu, H. Wang, Y. Wei, K. Li and X. Cheng, *J. Rare Earths*, 2010, **28**, 907–913.

6 M. Dan, M. Mihet and M. D. Lazar, *Int. J. Hydrog. Energy*, 2020, **45**, 26254–26264.

7 K. Otsuka, Y. Wang, E. Sunada and I. Yamanaka, *J. Catal.*, 1998, **175**, 152–160.

8 Q. G. Yan, T. H. Wu, W. Z. Weng, H. Toghiani, R. K. Toghiani, H. L. Wan and C. U. Pittman, *J. Catal.*, 2004, **226**, 247–259.

9 L. Song, Y. Kong and X. Li, *Int. J. Hydrog. Energy*, 2017, **42**, 19869–19876.

10 C.-C. Cormos, F. Starr, E. Tzimas and S. Peteves, *Int. J. Hydrog. Energy*, 2008, **33**, 1286–1294.

11 F. Yilmaz, M. Ozturk and R. Selbas, *Energy Convers. Manag.*, 2019, **186**, 229–240.

12 D. P. Serrano, J. A. Botas and R. Guil-Lopez, *Int. J. Hydrog. Energy*, 2009, **34**, 4488–4494.

13 T. Geißler, A. Abánades, A. Heinzel, K. Mehravaran, G. Müller, R. K. Rathnam, C. Rubbia, D. Salmieri, L. Stoppel, S. Stückrad, A. Weisenburger, H. Wenninger and Th. Wetzel, *Chem. Eng. J.*, 2016, **299**, 192–200.

14 C. Palmer, M. Tarazkar, H. H. Kristoffersen, J. Gelinas, M. J. Gordon, E. W. McFarland and H. Metiu, *ACS Catal.*, 2019, **9**, 8337–8345.

15 F. ezzahra Chakik, M. Kaddami and M. Mikou, *Int. J. Hydrog. Energy*, 2017, **42**, 25550–25557.

16 T. Nguyen, Z. Abdin, T. Holm and W. Mérida, *Energy Convers. Manag.*, 2019, **200**, 112108.

17 K. Bareiß, C. de la Rua, M. Möckl and T. Hamacher, *Appl. Energy*, 2019, **237**, 862–872.

18 H. Yoshida, S. Kato, K. Hirao, J. Nishimoto and T. Hattori, *Chem. Lett.*, 2007, **36**, 430–431.

19 A. Yamamoto, S. Mizuba, Y. Saeki and H. Yoshida, *Appl. Catal. Gen.*, 2016, **521**, 125–132.

20 K. Shimura and H. Yoshida, *Energy Environ. Sci.*, 2010, **3**, 615–617.

21 K. Shimura and H. Yoshida, *Energy Environ. Sci.*, 2011, **4**, 2467.

22 K. Shimura, H. Kawai, T. Yoshida and H. Yoshida, *ACS Catal.*, 2012, **2**, 2126–2134.

23 K. Shimura, T. Yoshida and H. Yoshida, *J. Phys. Chem. C*, 2010, **114**, 11466–11474.

24 A. Anzai, K. Fujiwara, A. Yamamoto and H. Yoshida, *Catal. Today*, 2020, **352**, 1–9.

25 H. Yoshida, S. Mizuba and A. Yamamoto, *Catal. Today*, 2019, **334**, 30–36.

26 H. Song, X. Meng, Z. Wang, Z. Wang, H. Chen, Y. Weng, F. Ichihara, M. Oshikiri, T. Kako and J. Ye, *ACS Catal.*, 2018, **8**, 7556–7565.

27 B. Han, W. Wei, M. Li, K. Sun and Y. H. Hu, *Chem. Commun.*, 2019, **55**, 7816–7819.

28 B. V. Ayodele, A. A. Ghazali, M. Y. Mohd Yassin and S. Abdullah, *Int. J. Hydrog. Energy*, 2019, **44**, 20700–20710.

29 B. Tan, Y. Ye, Z. Huang, L. Ye, M. Ma and Y. Zhou, *Chin. Chem. Lett.*, 2020, **31**, 1530–1534.

30 T. Kujirai, A. Yamaguchi, T. Fujita, H. Abe and M. Miyauchi, *Chem. Commun.*, 2021, **57**, 8007–8010.

31 W. Sarwana, A. Anzai, D. Takami, A. Yamamoto and H. Yoshida, *Catal. Sci. Technol.*, 2021, **11**, 5534–5542.

32 C.-Y. Xu, Q. Zhang, H. Zhang, L. Zhen, J. Tang and L.-C. Qin, *J. Am. Chem. Soc.*, 2005, **127**, 11584–11585.

33 H. Yoshida, M. Sato, N. Fukuo, L. Zhang, T. Yoshida, Y. Yamamoto, T. Morikawa, T. Kajino, M. Sakano, T. Sekito, S. Matsumoto and H. Hirata, *Catal. Today*, 2018, **303**, 296–304.

34 H. Yoshida, M. Takeuchi, M. Sato, L. Zhang, T. Teshima and M. G. Chaskar, *Catal. Today*, 2014, **232**, 158–164.

35 T. Zaremba, *Mater. Sci.-Pol.*, 2012, **30**, 180–188.

36 P. Ponce-Peña, M. A. González-Lozano, M. A. Escobedo-Bretado, P. de Lira-Gómez, E. García-Sánchez, E. Rivera and L. Alexandrova, *Ceram. Int.*, 2015, **41**, 10051–10056.

37 X. Zhu, A. Yamamoto, S. Imai, A. Tanaka, H. Kominami and H. Yoshida, *Chem. Commun.*, 2019, **55**, 13514–13517.

38 X. Zhu, A. Yamamoto, S. Imai, A. Tanaka, H. Kominami and H. Yoshida, *Appl. Catal. B Environ.*, 2020, **274**, 119085.

39 C.-Y. Xu, J. Wu, P. Zhang, S.-P. Hu, J.-X. Cui, Z.-Q. Wang, Y.-D. Huang and L. Zhen,

CrystEngComm, 2013, **15**, 3448–3454.

40 L. Cheng, H.-J. Liu, J.-J. Zhang, H.-M. Xiong and Y.-Y. Xia, *J. Electrochem. Soc.*, 6.

41 T. Sugai, S. Hasegawa and G. Ohara, *Jpn. J. Appl. Phys.*, 1968, **7**, 358.

42 H. Yu, Y. Zhao, S. Yan and P. Zhou, *J. Am. Ceram. Soc.*, 2019, **102**, 4325–4332.

43 H. Kato, M. Kobayashi, M. Hara and M. Kakihana, *Catal. Sci. Technol.*, 2013, **3**, 1733–1738.

44 H. Zhao, G. Yang, Z. Wang, X. Cao, L. Gu and N. Zhao, *J. Exp. Nanosci.*, 2015, **10**, 1126–1136.

45 P. Xue, Y. Hu, W. Xia, H. Wu and X. Zhu, *J. Alloys Compd.*, 2017, **695**, 2870–2877.

46 H. Idrissi, A. Aboujalil, J. P. Deloume, G. Fantozzi and B. Durand, *J. Eur. Ceram. Soc.*, 1999, **19**, 1997–2004.

47 A. Aboujalil, J. Deloume, F. Chassagneux, J. Scharff and B. Durand, *J. Mater. Chem.*, 1998, **8**, 1601–1606.

48 Z. Cai, X. Xing, R. Yu, X. Sun and G. Liu, *Inorg. Chem.*, 2007, **46**, 7423–7427.

49 P. A. Fuierer and R. E. Newnham, *J. Am. Ceram. Soc.*, 1991, **74**, 2876–2881.

50 D. Arney, B. Porter, B. Greve and P. A. Maggard, *J. Photochem. Photobiol. Chem.*, 2008, **199**, 230–235.

51 Q. Wang, T. Hisatomi, Y. Moriya, K. Maeda and K. Domen, *Catal. Sci. Technol.*, 2013, **3**, 2098–2103.

52 Z. Huang, J. Liu, L. Huang, L. Tian, Sen Wang, G. Zhang, J. Li, F. Liang, H. Zhang, Q. Jia and S. Zhang, *NPG Asia Mater.*, 2020, **12**, 1–12.

53 R. B. Yahya, H. Hayashi, T. Nagase, T. Ebina, Y. Onodera and N. Saitoh, *Chem. Mater.*, 2001, **13**, 842–847.

54 M. A. Escobedo Bretado, M. A. González Lozano, V. Collins Martínez, A. López Ortiz, M. Meléndez Zaragoza, R. H. Lara and C. U. Moreno Medina, *Int. J. Hydrog. Energy*, 2019, **44**, 12470–12476.

55 X. Zhu, A. Yamamoto and H. Yoshida, *Dalton Trans.*, 2021, **50**, 7976–7983.

56 M. A. Siddiqui, V. S. Chandel and A. Azam, *Appl. Surf. Sci.*, 2012, **258**, 7354–7358.

57 Q. Chen, L. Chen, J. Qi, Y. Tong, Y. Lv, C. Xu, J. Ni and W. Liu, *Chin. Chem. Lett.*, 2019, **30**, 1214–1218.

58 J. Tauc, R. Grigorovici and A. Vancu, *Phys. Status Solidi B*, 1966, **15**, 627–637.

59 J. Wang, L. Shen and N. Bao, *J. Mater. Sci.*, 2019, **54**, 10620–10631.

60 J. Wang, C. Li, B. Liang and X. Wang, *Rare Met.*, 2009, **28**, 24.

61 Y. Fujiki and F. Izumi, *J. Ceram. Assoc. Jpn.*, 1977, **85**, 155–162.

62 H. Yoshida, K. Hirao, J. Nishimoto, K. Shimura, S. Kato, H. Itoh and T. Hattori, *J. Phys. Chem. C*, 2008, **112**, 5542–5551.

4. Temperature-Graduated Nickel-Silica Catalysts for Photothermal Steam Reforming of Methane

Abstract

Photothermal steam reforming of methane (PTSRM) is a promising catalytic technology for converting stable methane and water into hydrogen utilizing solar energy. In the present study, the photothermal catalytic activity of silica-supported nickel (Ni/SiO_2) catalysts was investigated using a gas-flow reactor under concentrated visible/near-infrared light irradiation at various experimental parameters to obtain insight into factors affecting the activity and selectivity. In the thermal SRM at 773 K in dark, the CH_4 conversion reached near-equilibrium in all four Ni/SiO_2 catalysts, while there was a significant difference in activity between the catalysts in the PTSRM reaction under light irradiation. These results indicate that PTSRM activity was affected by both thermodynamic and kinetic aspects. The conversion–selectivity relationship revealed that the product selectivity in PTSRM was different from the values in thermal SRM in dark and calculated thermodynamic equilibrium. The author proposed that concentrated light irradiation created the highest temperature zone in the center of the reactor and the lower temperature zone downstream, and the consecutive water gas shift reaction and CO hydrogenation occur in the lower temperature zone, thus resulting in the characteristic product selectivity. This study shows a possibility for PTSRM systems with a controllable selectivity by the temperature gradient formed under concentrated sunlight irradiation.

4.1. Introduction

Steam reforming of methane (SRM, eq. 1) is one of the most established catalytic technology in the industry for the production of hydrogen and/or carbon monoxide from methane and water.[1–6] In the commercial process, the obtained CO gas can be converted into CO_2 via a water gas shift (WGS, eq. 2) reaction to obtain a high H_2 yield.

$CH_4 + H_2O \rightarrow CO + 3\ H_2$ $\quad \Delta H^{\circ}_{298K} = 206\ \mathrm{kJ\ mol^{-1}}$ (1)

$CO + H_2O \rightarrow CO_2 + H_2$ $\quad \Delta H^{\circ}_{298K} = -41\ \mathrm{kJ\ mol^{-1}}$ (2)

The overall chemical equation for producing a mixture of H_2 and CO_2 is as follows:

$CH_4 + 2\ H_2O \rightarrow CO_2 + 4\ H_2$ $\quad \Delta H^{\circ}_{298K} = 165\ \mathrm{kJ\ mol^{-1}}$ (3)

SRM is a highly endothermic reaction; thus, it needs high temperatures (>973 K) to obtain sufficient conversion due to the thermodynamic limit.[7–10] To gain such high temperatures, tremendous input heat energy is supplied typically by methane combustion.[11,12] Considering methane as the hydrogen source, utilizing some parts of methane as the heat source lowers the H_2 yield, which is unfavourable energetically and economically. Therefore, a renewable energy source that does not consume the reactant is highly desirable for performing the SRM reaction.

Solar energy is one of the promising alternatives to perform SRM reactions as an abundant and environmentally friendly energy source. For the utilization of solar energy for catalytic reaction systems, approaches are divided into three categories: photothermal[13–18] and photocatalytic systems[19–32] and their combination.[25,33] The systems using photocatalysts have been investigated extensively and attract attention now; however, it is still a significant challenge to improve the quantum efficiency and develop a system that works under visible and near-infrared (vis/NIR) light, a large portion of sunlight. In contrast, the photothermal SRM (PTSRM) using concentrated solar light is an effective way,

where the photothermal conversion induces high temperatures in the catalytic part using vis/NIR light.[17,18]

For the photothermal conversion catalysts, both the light absorption and catalytic properties are essential to achieve a highly-active system. It is known that the incorporation of metal nanoparticles into support materials without having light absorption increased the vis/NIR absorption drastically,[34–36] and the metal nanoparticles also function as a catalytic active site. Among various metals, Ni is one of the most active components for SRM, used for the industrial process. Recently, it has been reported that the fabrication of small and uniform Ni nanoparticles via the decomposition of Ni phyllosilicates (Ni PS) for the enhancement of catalytic activity in thermal SRM (TSRM).[37–39] Thus, this catalyst preparation technique would be effective in developing the highly-active catalysts for PTSRM. Moreover, the photothermal catalytic system provides inhomogeneous temperature distribution under concentrated light irradiation, and the temperature gradient affects the catalytic activity. Recently, Mao et al. reported that the different temperature zone on the Fe catalyst and $TiO_{2-x}H_y$ under light irradiation enhanced ammonia production rates beyond the equilibrium conversion.[40] Li et al. reported that the thermal gradients in Ru−Cs/MgO catalysts improved the reaction rates and conversion of ammonia production under solar light irradiation.[41] Nevertheless, to the best of the author's knowledge, the effect of the temperature gradient in the catalyst on the catalytic performance in PTSRM has not been investigated so far.

In the present study, the author fabricated four Ni/SiO_2 catalysts by decomposition of Ni PS and impregnation with three Ni precursors, and compared their catalytic performance in PTSRM. Moreover, the author investigated the effect of light conditions (i.e., the power and spot size) on the catalytic performance. By comparison of the product selectivity in PTSRM with the experimental and theoretical values in TSRM, the author proposed that the observed temperature gradient under the catalytic reaction condition contributes to changing the product selectivity.

4.2. Experimental method

4.2.1. Catalyst preparation

The 20wt% Ni/SiO_2 sample via Ni PS decomposition was prepared by an impregnation method using an ammonia solution.[42–45] The SiO_2 powder (Sciqas, 0.05 μm, Sakai Chemical, 2 g) was dispersed in a 28% ammonia solution (100 ml) containing nickel basic carbonate tetrahydrate ($NiCO_3{\cdot}2Ni(OH)_2{\cdot}4H_2O$, Wako, 98%) and the suspension was magnetically stirred in the water bath at 353 K until dried. The mixture was then kept in the oven at 353 K overnight. The obtained powder was mixed by an alumina mortar for 10 min and calcined at 723 K for 2 h. Before the characterizations, the sample was reduced by a 10% H_2/Ar gas for 30 min (referred to as Ni-Car). The other three 20wt% Ni/SiO_2 samples were prepared by a typical impregnation method with nickel precursors of nickel acetate tetrahydrate ($Ni(CH_3CO_2)_2{\cdot}4H_2O$, Wako, 98%), nickel nitrate hexahydrate ($Ni(NO_3)_2{\cdot}6H_2O$, Wako, 98%), and nickel lactate tetrahydrate ($Ni(C_3H_5O_3)_2{\cdot}4H_2O$, Wako, 99%) using deionized water as a solvent. These samples are referred to as Ni-Ace, Ni-Nit, and Ni-Lac, respectively.

4.2.2. Characterization

The X-ray diffraction (XRD) patterns were recorded on a Shimadzu Lab X XRD-6000 at room temperature using Cu Kα radiation (40 kV, 30 mA). The Ni crystallite size (d_{XRD}) was estimated from a full width at half maximum (FWHM) of the diffraction line at 2θ = 44° in the XRD pattern by the Scherrer equation. The transmission electron microscopy (TEM) images were captured by a JEOL JEM-2100F at 200 kV. The dispersion of Ni (D) was calculated from the distributions of Ni particle size by TEM using cubic-octahedral-shaped nanoparticles as a model. Ni K-edge XAFS measurements were performed at BL12C of the Photon Factory (KEK-PF, Tsukuba, Japan). The samples after the reduction treatment by a 10% H_2/Ar gas were packed using a polyethene bag without exposure to air and measured in a transmission mode. The diffuse reflectance (DR) UV/vis/NIR spectra of the samples were measured by a JASCO V-570 equipped with an integrating sphere, where $BaSO_4$ was used as a reference. The specific surface area

(S_a) was measured by N_2 adsorption at 77 K (BET method) with a Quantachrome Monosorb MS-21.

4.2.3. Catalytic activity test in PTSRM and TSRM

Catalytic activity tests in PTSRM and TSRM were performed using a continuous flow fixed bed reactor, as depicted in Figure 4.1. The sample powder was pressed into a pellet under 40 MPa for 1 min using a Newton press and then pulverised by an alumina mortar. The obtained granules (50–100 mesh) were added to a quartz reactor (20 × 20 × 1 mm^3). Before the activity test, the sample was pretreated by a 10% H_2/Ar gas at 873 K for 30 min using an electrical muffle furnace. Then, the reaction gas, 8%CH_4/12%H_2O/6%N_2/Ar(balance), was fed into the reactor, where the N_2 gas was used as the internal standard for quantifying the reactants and products. The partial pressure of steam was controlled by changing the temperature in the water supply. For the photothermal catalytic activity test, a 300 W Xe lamp (PE300BUV, Excelitas technologies) equipped with a cut-off filter (λ > 420 nm, W-Y435, HOYA) and a convex lens was used as the light source. The diameter of the irradiation area (Ø) was varied from 2.0 to 1.4 cm (typically 2.0 cm) by changing the position between the Xe lamp and reactor. The light power (*P,* typically 23.8 W, which correspond to 5.95 W cm^{-2}) was controlled by changing the current values of the power supply. The maximum surface temperatures on the front ($T_{max,f}$) and back ($T_{max,b}$) sides of the reactor were measured by a radiative thermometer (TMHX-CGE2400-0150H2.2, Japan Sensor, detection wavelength: 5.0–5.6 μm, spot size: 2.2 mm). The gaseous products (5 mL) were analysed by online gas chromatography equipped with a thermal conductivity detector (GC-8A, Shimadzu) at 20 minutes intervals. The CH_4 conversion, carbon balance, and CO_2 selectivity were calculated based on the following equations:

$$CH_4 \text{ conversion } (\%) = ([CH_4]_{in} - [CH_4]_{out})/[CH_4]_{in} \times 100 \quad (4)$$

$$\text{Carbon balance} = ([CO]_{out} + [CO_2]_{out} + [CH_4]_{out}) / [CH_4]_{in} \quad (5)$$

$$CO_2 \text{ selectivity } (\%) = [CO_2]_{out} / ([CO_2]_{out} + [CO]_{out}) \times 100 \quad (6)$$

where $[X]_{in}$ and $[X]_{out}$ are concentrations of X (X = CH_4, CO, or CO_2) in the inlet and outlet gases, respectively. The light to chemical conversion efficiency (η) was calculated by the following equations:[35,46]

$$\eta\ (\%) = (r_{H_2} \Delta H^{o}_{c\,H_2} + r_{CO}\ \Delta H^{o}_{c\,CO} - r_{CH_4} \Delta H^{o}_{c\,CH_4}) / P \times 100 \quad (7)$$

where, $\Delta H^{o}_{c\,X}$ and r_X are enthalpy of combustion, production rate and conversion rate of X, respectively. The thermodynamic equilibrium conversion was calculated using the NASA-CEA program.[47]

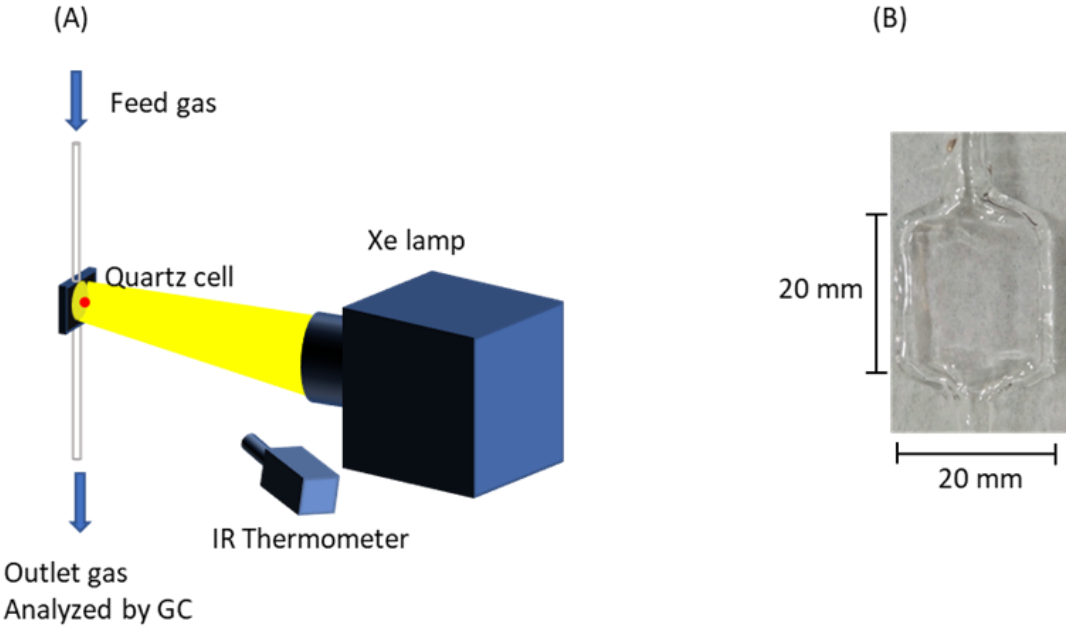

Figure 4.1 (A) Experimental set-up of the flow reactor in the photothermal reaction test for PTSRM and (B) digital photograph of the reactor.

4.3. Result and discussion

4.3.1. Characterization of the catalysts

In the Ni-Car sample, Ni PS and Ni hydroxide were formed after the impregnation using an aqueous ammonia solution, and the Ni hydroxide was converted to Ni oxide after the calcination treatment at 723 K based on the TEM images and XRD patterns

(Figure 4.2). After the H_2 reduction at 873 K, the Ni species were reduced to Ni metal, as shown in Figure 4.3A, which was consistent with the previous reports.[42–45] In all the Ni samples prepared with different Ni precursors using water as a solvent, metallic Ni were observed, and there was no diffraction peak derived from impurities. Figure 4.3B shows the Ni K-edge XANES spectra of the Ni/SiO_2 samples reduced at 873 K for 30 min. The shapes of the XANES spectra of the reduced Ni samples were almost identical to that of Ni foil, which indicates that all the Ni species were reduced to Ni metal after the reduction pretreatment.

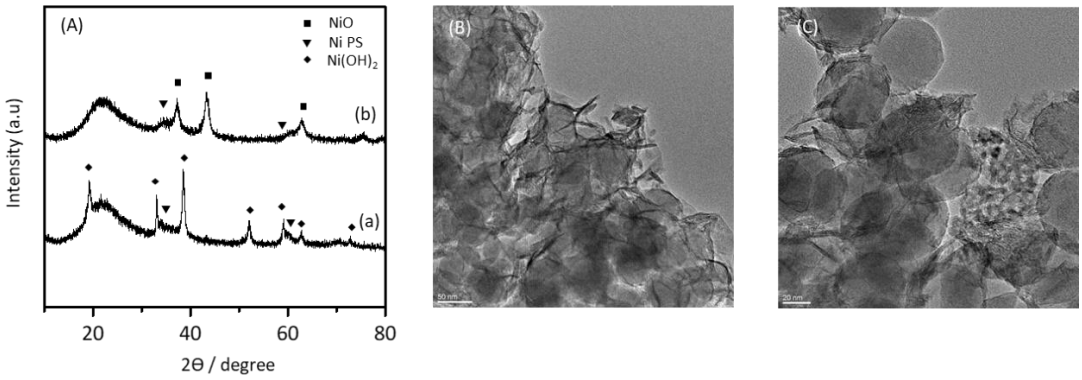

Figure 4.2 (A) XRD patterns of the Ni-Car sample after (a) impregnation and (b) calcination at 723 K for 2 hours and TEM images of the Ni-Car sample after (B) impregnation and (C) calcination at 723 K for 2 hours.

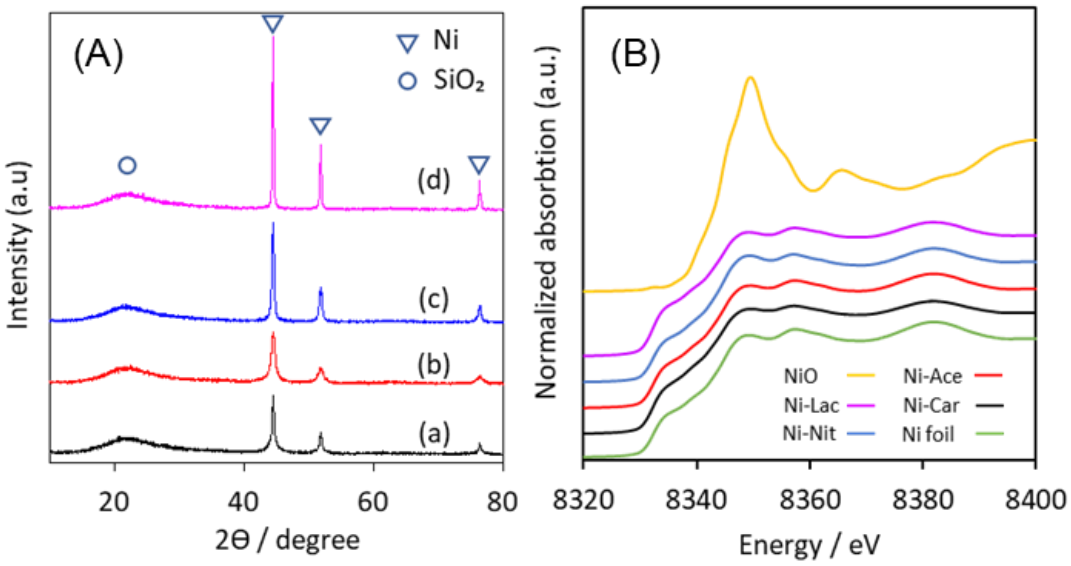

Figure 4.3 (A) XRD patterns and (B) XANES spectra of the Ni/SiO_2 samples after the reduction pretreatment at 873 K. (a): Ni-Car, (b): Ni-Ace, (c): Ni-Nit, and (d): Ni-Lac.

Table 4.1 Structural properties of the Ni/SiO_2 samples.

Entry	Sample	d_{XRD} [a] / nm	d_{TEM} [b] / nm	D [c] (%)	S_a [d] / $m^2\ g^{-1}$
1	Ni-Car	18.9	7.8	5.5	88.9
2	Ni-Ace	11.0	10.0	9.5	61.0
3	Ni-Nit	24.9	14.6	3.9	61.5
4	Ni-Lac	43.2	8.5	3.1	52.5
5	SiO_2	-	-	-	57.1

[a] Crystallite size calculated from a line width of the Ni (111) peak in the XRD patterns. [b] Mean particle size (number-averaged) of Ni particles estimated from the TEM images. [c] Ni dispersion, [number of surface Ni atoms]/[number of total Ni atoms], calculated from the particle size distributions by TEM (Figure 4.4). [d] Specific surface area measured by N_2 adsorption experiments.

The size and morphology of Ni particles in the Ni/SiO_2 samples were confirmed by TEM (Figure 4.4). In the Ni-Car sample (Figure 4.4A), aggregated small Ni particles were observed in a high magnification image (Figure 4.5), which was completely different from the other Ni/SiO_2 samples prepared by the conventional impregnation method. In the HAADF-STEM image of the Ni-Car sample, a contrast was observed between bright nanoparticles and a thin layer surrounding the particle (Figure 4.6), which indicates that Ni nanoparticles are partially covered by a silica shell.[42,43] Besides, the Ni-Car sample exhibited the highest S_a, followed by Ni-Nit, Ni-Ace and Ni-Lac samples (Table 4.1). The increased S_a in Ni-Car would be originated from the formation and decomposition of Ni PS and Ni nanoparticles partially covered by the SiO_2 layer.

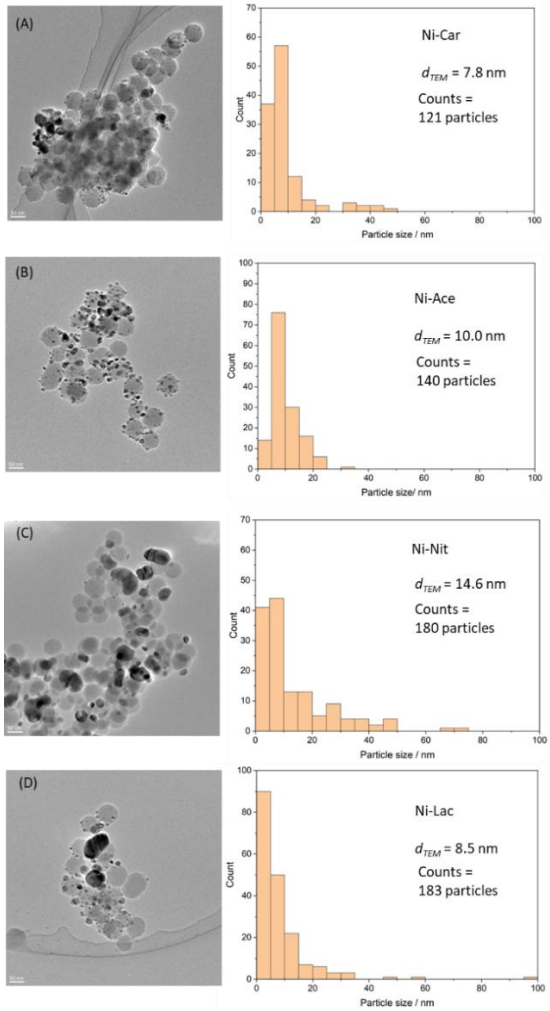

Figure 4.4 TEM images and particle size distributions of the Ni/SiO_2 samples after the reduction at 873 K. (A) Ni-Car, (B) Ni-Ace, (C) Ni-Nit, and (D) Ni-Lac.

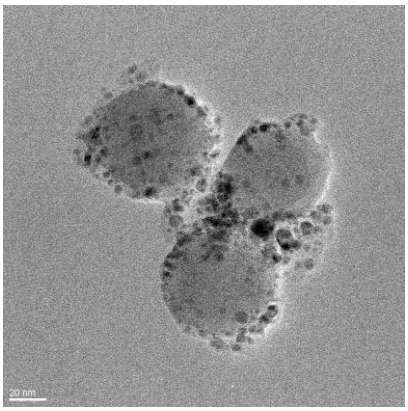

Figure 4.5 TEM image of the Ni-Car sample after the reduction treatment in high magnification.

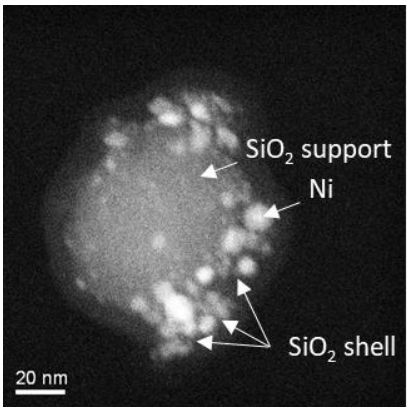

Figure 4.6 STEM image of the Ni-Car sample after the reduction treatment.

The mean Ni particle size (d_{TEM}) by TEM in the Ni-Car sample was the smallest (7.8 nm) among the four Ni/SiO_2 samples (Ni-Ace 10.0 nm; Ni-Nit: 14.6 nm; Ni-Lac: 8.5 nm), as shown in Table 4.1. The crystallite size estimated from the XRD peaks using the Scherrer equation showed different values from d_{TEM}. The crystallite size obtained by the Scherrer equation is volume-weighted average particle size (d_V).[48] The d_V value is different from the number-averaged value for typical TEM analysis when the particle size has distribution. To investigate the consistency between the Ni particle size by TEM and the crystalline size by XRD, the author calculated d_V from the particle size distributions by TEM using the following equation.[48]

$$d_V = \frac{\sum n_i d_i^4}{\sum n_i d_i^3} \quad (8)$$

where n_i is the number of the Ni particles with a diameter of d_i.

The order of the d_V values was consistent with the Ni crystalline size by XRD although the absolute values did not coincide. Based on the data, the author concluded that the data of Ni particle size by TEM were consistent with the crystalline size by XRD (Table 4.2) and the difference between them would be due to the relatively large particle size distribution of the Ni particles.

Table 4.2 Volume-weighted particle size (d_V) of the Ni samples

Entry	Sample	d_{XRD} / nm	d_V / nm
1	Ni-Car	18.9	33.1
2	Ni-Ace	11.0	18.1
3	Ni-Nit	24.9	45.5
4	Ni-Lac	43.2	72.3

The Ni dispersion was calculated from the particle size distributions by TEM (Table 4.1), and the order was consistent with the crystallite size by XRD.

Figure 4.7 shows the DR UV/vis/NIR absorption spectra of the pristine SiO_2 and reduced Ni/SiO_2 samples after the reduction pre-treatment at 873 K. The small peaks at 1390, 1900 and 2210 nm in wavelength were observed in all the samples, which can be assignable to surface hydroxyl groups and adsorbed water.[49] The bare SiO_2 sample exhibited high diffuse reflectance (> 80%), while intense absorption in the visible and near-infrared range (less reflectance < 15%, 400–2400 nm) was recorded in all the Ni/SiO_2 samples. These results indicate that the metallic Ni particles function as the light-harvesting site.[50–52]

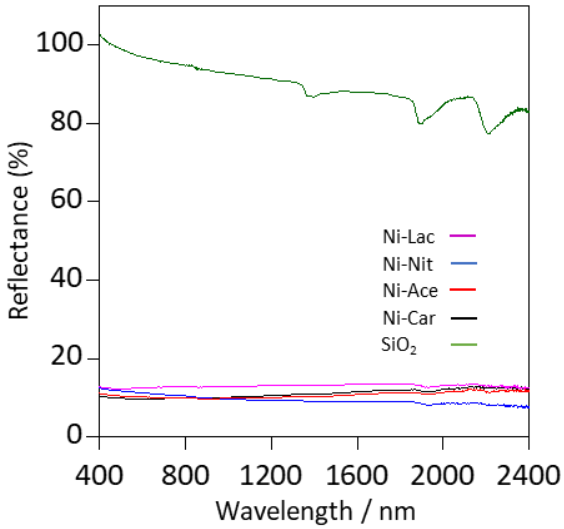

Figure 4.7 DR UV/vis/NIR reflectance spectra of the Ni/SiO_2 samples after the reduction pretreatment at 873 K.

4.3.2. Catalytic activity in PTSRM

The time course of the PTSRM reaction was first investigated over the four Ni samples (Figure 4.8) for 120 min. The catalytic activities on Ni-Car, Ni-Ace and Ni-Nit were stable but decreased with time on Ni-Lac. The TG-DTA measurement was carried out to investigate the coke formation on the spent Ni/SiO_2 catalysts. The measurement was performed under an air atmosphere, and the heating rate was 10 K min^{-1} from room temperature to 1273 K. No clear weight loss and exothermic peak due to the oxidation of carbon was recorded in all the Ni/SiO_2 samples used in the PTSRM reaction test (Figure 4.8). Separately, a Ni-Lac reduced sample was mixed with 10 wt% of carbon active, and the TG-DTA measurement was performed as a reference. The weight loss (~10%) was observed at around 800–900 K due to the oxidation of carbon. These results indicate that an observable amount of coke was not formed during the PTSRM reaction (Figure 4.9).

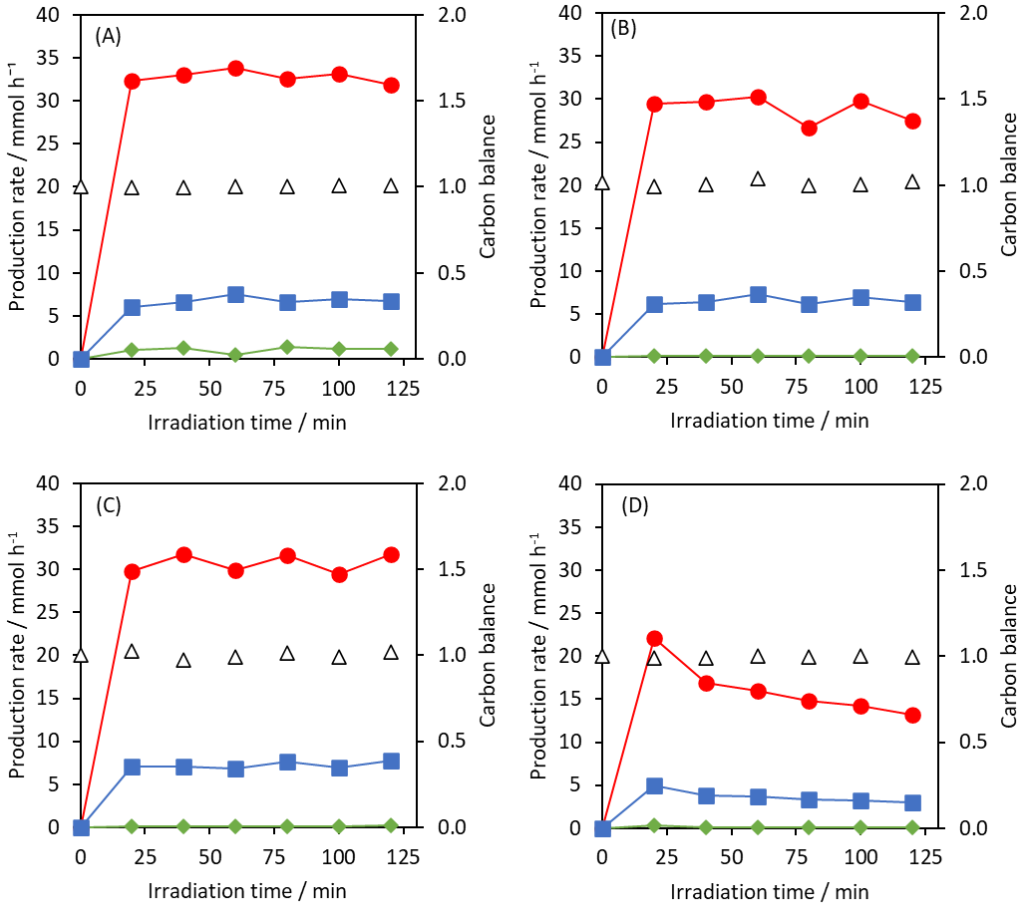

Figure 4.8 Time courses of the production rates of H_2 (circles), CO_2 (squares), and CO (diamonds) and carbon balance (triangles) in PTSRM. (A): Ni-Car, (B): Ni-Ace, (C): Ni-Nit, and (D): Ni-Lac. Reaction conditions; catalyst weight: 0.5 g, the total gas flow rate: 100 ml min^{-1}, reactant gas concentrations: 8%CH_4/12%H_2O/6%N_2/Ar(balance), light power: 23.8 W, wavelength of light: λ > 420 nm.

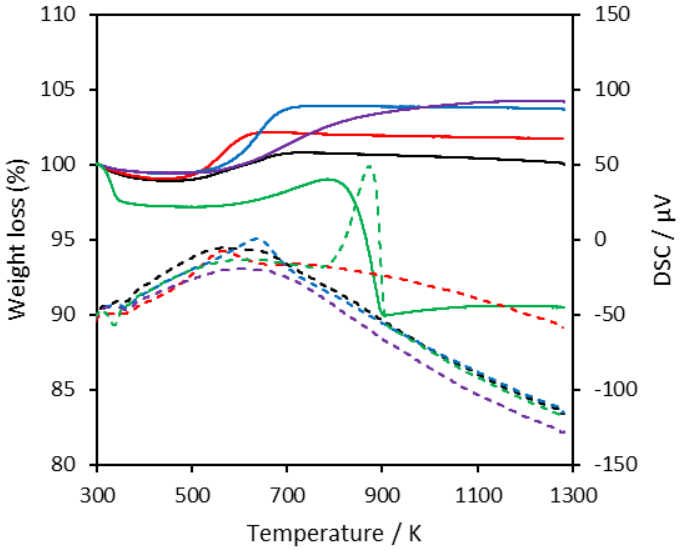

Figure 4.9 TG (solid lines) and DTA (dash lines) profiles of the various Ni/SiO_2 samples after the PTSRM reaction for 120 min. Ni-Car: black, Ni-Ace: red, Ni-Nit: blue, and Ni-Lac: violet. Green: reduced Ni-Lac sample mixed with the 10 wt% active carbon as a comparison.

Based on the TEM images (Figure 4.10) and XRD patterns (Figure 4.11), the particle size of Ni increased after the reaction, suggesting the deactivation in Ni-Lac results from the aggregation of Ni particles. Figure 4.12 shows the comparison of the production rates of H_2, CO_2 and CO after 120 min of the reactions. The Ni-Car, Ni-Ace, and Ni-Nit samples showed similar activity, and Ni-Lac showed the lowest one among the samples, where there was no significant difference in the $T_{max,f}$ values between the samples (Figure 4.12). Moreover, the CO formation was clearly observed only in the case of Ni-Car (1.2 mmol h^{-1}), while tiny amounts of CO was detected in the other samples (0.1–0.2 mmol h^{-1}). The light to chemical conversion efficiency (Eq. 7) was also plotted in Figure. 4.12 and the highest value was 2.6% in the Ni-Car sample. Separately, the author confirmed that a bare SiO_2 sample did not show activity for PTSRM, which indicates that the Ni particles work as the catalytic active site.

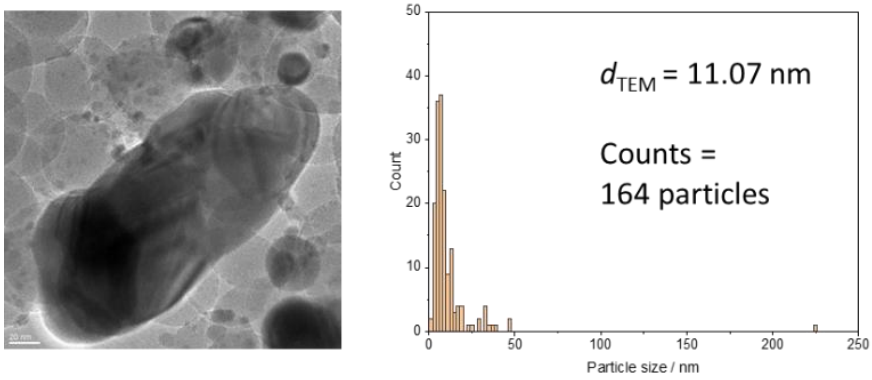

Figure 4.10 TEM image and particle size distribution of the Ni-Lac sample after the PTSRM reaction for 120 min.

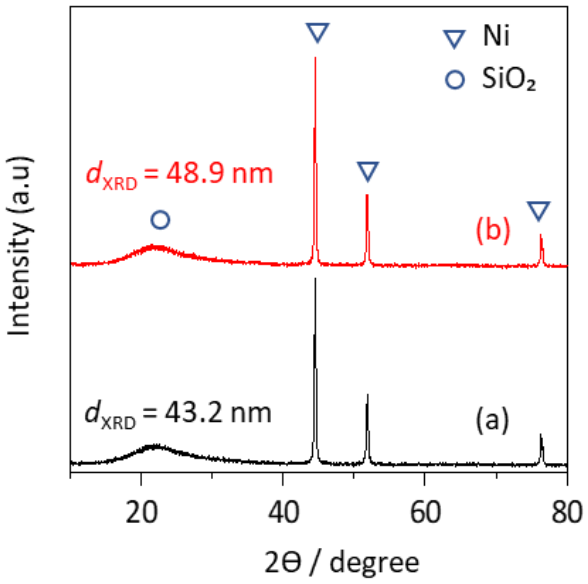

Figure 4.11 XRD patterns of the Ni-Lac samples (a) before and (b) after the PTSRM reaction for 120 min

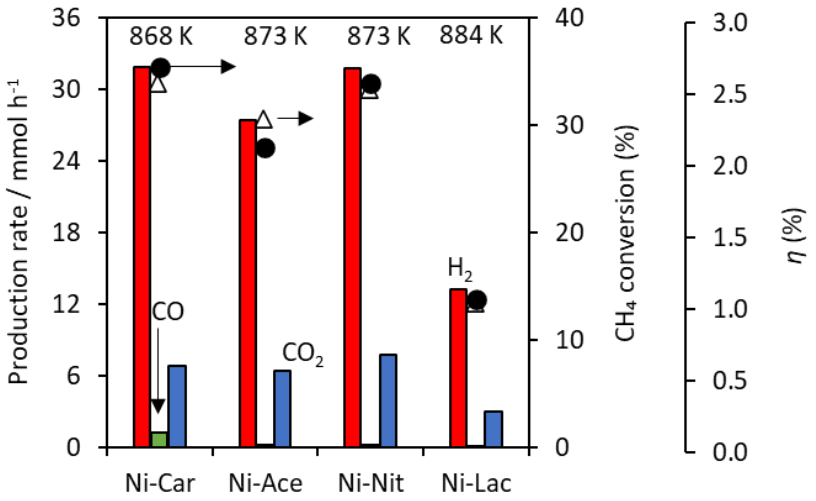

Figure 4.12 Production rates of H_2 (red), CO_2 (blue), and CO (green), CH_4 conversion (black circles), and light to chemical conversion efficiency (η, Eq. 7) (open triangle) in PTSRM over the Ni/SiO_2 samples. The outlet gas was sampled 120 min after starting photoirradiation. The temperatures at the top of the bars were highest front-side temperatures of the reactor ($T_{max,f}$). The reaction conditions are the same as those mentioned in the caption of Figure 4.8.

For the comparison, a thermocatalytic steam reforming of methane (TSRM) reaction was performed with an electric heater in dark (Figure 4.13) at 773 and 723 K. In these experiments, the reaction temperatures were set to be comparable to the catalytic activity in PTSRM. At 773 K, the production rates of H_2 and CH_4 conversion were 36–38 mmol h^{-1} and 44–46 %, respectively, in all the samples, and there was no significant difference in the activity. The obtained CH_4 conversion was close to the calculated equilibrium conversion (CH_4 conversion = 45.7%) (Table 4.3). These catalytic activities reached near equilibrium, which would cause no significant difference in the activity between the samples at 773 K. Contrary, the Ni-Lac sample did not reach the equilibrium (CH_4 conversion = 32.2%) at the lower temperature of 723 K, while the other sample reached it. The lower activity of Ni-Lac would be due to the fewest surface Ni sites (i.e., lowest dispersion, Table 4.1) in TSRM. These results mean that, at high temperatures, thermodynamic constraints dominate the activity, while the kinetic

factor also affects the reaction rate at the lower temperature (723 K) in the present conditions of TSRM.

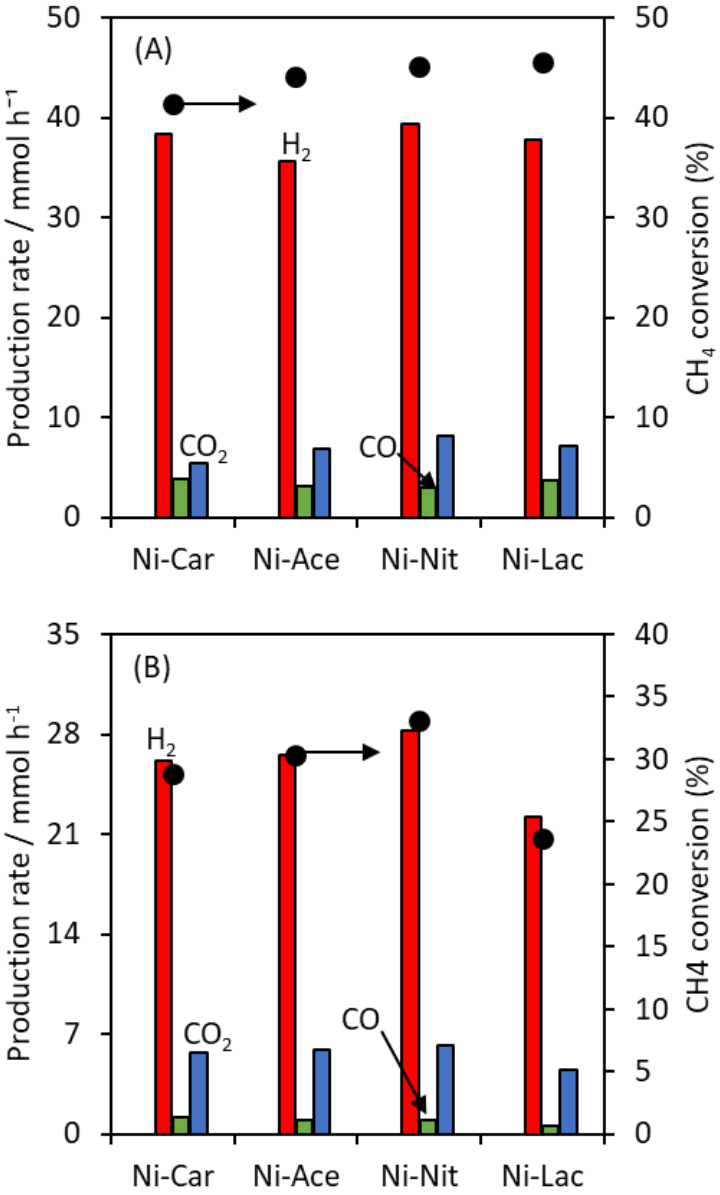

Figure 4.13 Production rates of H_2 (red), CO_2 (blue), and CO (green), and CH_4 conversion (black circles) in TSRM over the Ni/SiO_2 samples at (A) 773 K and (B) 723 K. The outlet gas was sampled 60 min after starting the reaction. The catalyst amount, reactant gas concentrations, total flow rate were the same as those of Figure 4.8.

Table 4.3 Thermodynamic equilibrium conversion in steam reforming of methane.[a]

T / K	CH_4 conversion (%)	CO selectivity[b] (%)	CO_2 selectivity[c] (%)
573	7.7	0.5	99.5
673	21.7	6.1	93.9
723	32.2	15.2	84.8
773	45.7	31.2	68.8
823	62.1	51.1	48.9
873	79.0	68.2	31.8
973	97.4	83.8	16.2

[a] The calculation was performed at the total pressure of 1 atm using the same concentrations of the reactant gases as the experimental condition. [b] CO selectivity (%) = $[CO]_{eq}$ / ($[CO_2]_{eq}$ + $[CO]_{eq}$) × 100. [c] CO_2 selectivity (%) = $[CO_2]_{eq}$ / ($[CO_2]_{eq}$ + $[CO]_{eq}$) × 100. $[X]_{eq}$ is concentration of *X* in equblium at the temperatures.

The influence of the light power on the PTSRM activity on the Ni-Car sample was investigated (Figure 4.14) by changing the current values of the power supply. No reaction proceeded in dark (i.e., 0 W), and both the temperature and activity increased with increasing the light power from 8.4 to 23.8 W. In the moderate light powers of 8.4 and 15.8 W, only H_2 and CO_2 were produced, and CO was formed only at the highest light power of 23.8 W. The CO formation is thermodynamically preferable in higher temperature regions,[53,54] which would result in an increased amount of CO at the high light power in PTSRM.

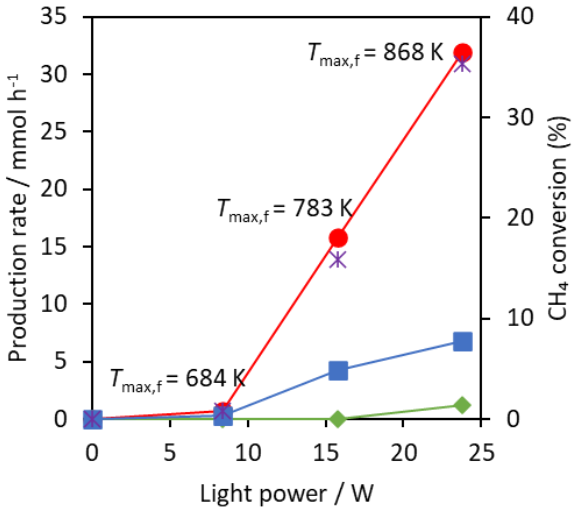

Figure 4.14 Production rates of H_2 (circles), CO_2 (squares), CO (diamonds), and CH_4 conversion (asterisk) at various light powers. Catalyst: Ni-Car. The reaction conditions are the same as those mentioned in the caption of Figure 4.8.

The stability of Ni-Car in the PTSRM reaction was further evaluated for 30 h (Figure 4.15) in the same reaction condition as mentioned in Figure 4.8. The production rates of H_2, CO and CO_2 were not changed even during 30 h. The XRD pattern of the used Ni-Car sample confirmed no obvious change in the Ni particle size before and after a long-time reaction (Figure 4.16).

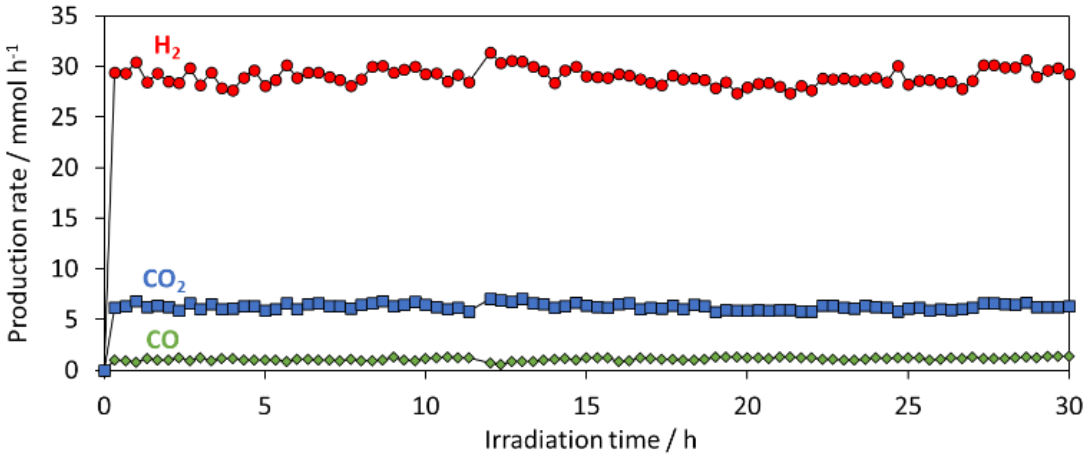

Figure 4.15 Long-time reaction test in PTSRM on Ni-Car. The reaction conditions are the same as those mentioned in the caption of Figure 4.8.

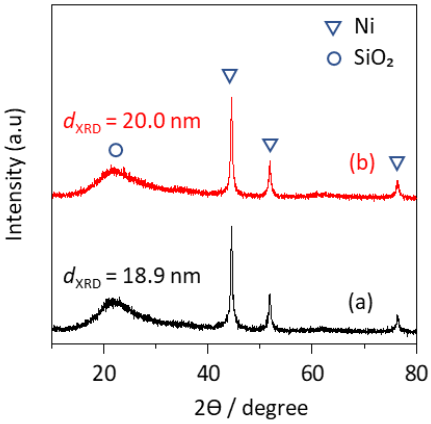

Figure 4.16 XRD patterns of the Ni-Car samples (a) before and (b) after the PTSRM reaction for 30 h.

Furthermore, 5 cyclic reaction tests (one cycle: 4 h) were performed and the reduction pretreatment at 873 K was carried out between the cycles. No obvious change in the PTSRM activity was observed (Figure 4.17). These results evidenced the high stability of the Ni-Car sample in the current PTSRM reaction.

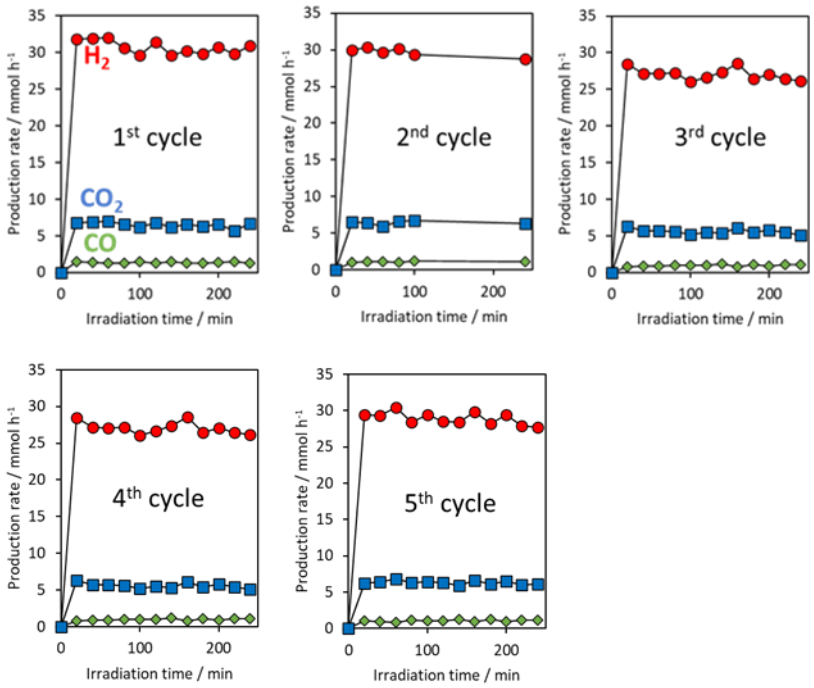

Figure 4.17 Cyclic reaction tests of the Ni-Car sample in PTSRM reaction. The reaction conditions were the same as those of Figure 4.8.

The spot size of the concentrated light changes the intensity of light. To investigate the effect of the spot size on the catalytic performance, the author performed PTSRM on the Ni-Car sample with various spot sizes, where the spot size was controlled by changing the distance between the reactor and the light source. By decreasing the spot diameter from 2.0 cm to 1.4 cm (Figure 4.18A), the H_2 production rate and CH_4 conversion increased (Figure 4.18B). At the smallest spot size of 1.4 cm, the CH_4 conversion was 46.0%, and the light-to-chemical conversion efficiency was calculated to be 3.1% based on Eq. 7. Then, the author measured the surface temperatures of the irradiated side of the reactor at the spot size of 2.0 cm in PTSRM on Ni-Car (i.e., the same conditions as those of Figure 4.8) as shown in Figure 4.18A. In these measurements, the two-dimensional temperature image was measured by changing the temperature measurement positions for the IR thermometer. The surface temperature concentrically decreased with the highest temperature at the center. Next, the author measured

the surface temperatures at different measurement positions moved vertically below the maximum temperature point (Figure 4.18A) at various light spot sizes (Ø = 2.0–1.4 cm). The temperature decreased by moving the measurement point to the lower side at all the spot sizes (Figure 4.18C). With increasing the spot size, $T_{max,f}$ tended to monotonically decrease (Figure 4.18D, i.e., 0 mm in Figure 4.18C), while the surface temperature at 8 mm below ($T_{8mm,f}$) had a minimum value. Note that the largest spot size in the current study (2.0 cm) was inscribed in a square reactor (Figure 4.18A), and in the smaller spot sizes (< 2.0 cm), the outer part of the light spot is not directly heated by light. Thus, the different trends could be explained by the balance of the heat generation by light and heat transfer from the centre side of the light spot. More importantly, the temperature gradient on the irradiated reactor surface becomes larger in smaller spot sizes (Figure 4.18C). In addition, $T_{max,b}$ also decreased monotonically with increasing the spot size (Figure 4.18D), and the difference between $T_{max,f}$ and $T_{max,b}$ increased by decreasing the spot size, possibly due to the higher heat transfer in the larger temperature difference. Thus, the temperature gradient was formed in all the spot size conditions and became larger using the smaller spot size in both horizontal (from the front to the back) and vertical (from the centre to below) directions to light irradiation. The PTSRM activity increased by decreasing the spot size to 1.7 cm, which would be due to the temperature increase derived from the high light intensity. But, surprisingly, the PTSRM activity became stable less than 1.7 cm despite the significant increase of $T_{max,f}$. This trend could be explained by the reverse reaction of Eqs. 1 and 3 at the lower temperature zone below the centre of the light spot with maximum temperature; even though a high conversion is obtained upstream at the high-temperature zone, the reverse reaction could proceed downstream up to the thermodynamic equilibrium at that low-temperature condition.

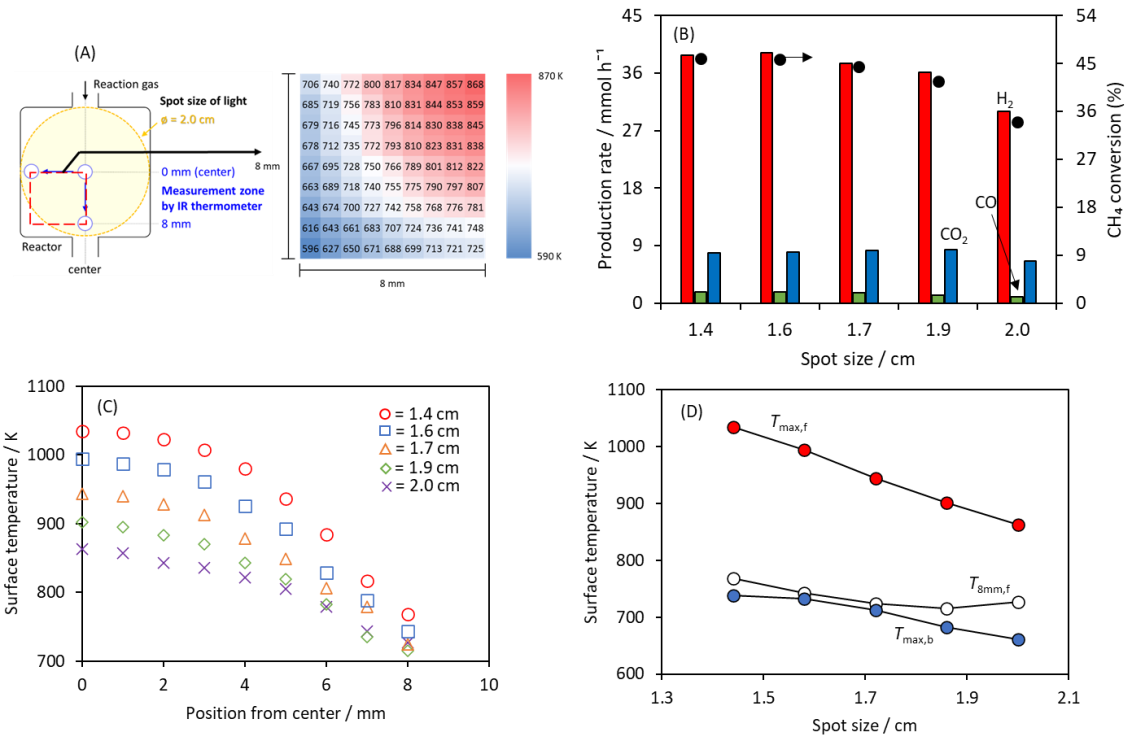

Figure 4.18 (A) Schematic illustration for the temperature measurements and a 2-dimensional temperature image of reactor in PTSRM on Ni-Car. The reaction conditions are the same as those of Figure 4.8. (B) Production rates of H_2 (red), CO_2 (blue), and CO (green), and CH_4 conversion (black circles) in PTSRM on Ni-Car in various spot sizes of light (Ø = 2.0–1.4 cm). The product was sampled 60 min after starting photoirradiation. (C) Surface temperatures of the reactor at different measurement positions at various spot sizes. The horizontal axis is the distance between the point of maximum temperature. (D) Surface temperatures of the reactor at different positions. Red: $T_{max,f}$, blue: $T_{max,b}$, and white: temperature at the point below 8 mm from the maximum temperature point ($T_{8mm,f}$).

4.3.3. Comparison between PTSRM and TSRM

At Ø = 2.0 cm, the CH_4 conversion in PTSRM was 34.1% (Figure 4.12, $T_{max,f}$ = 868 K), which was lower than that of TSRM at 773 K (44.0%, Figure 4.13A). In PTSRM, the surface temperature of the reactor decreased by moving away from

the centre of the light spot by ca. 140 K (Figure 4.18B), which indicates that the low-temperature zone in the reactor would cause the lower catalytic activity in PTSRM than TSRM. The reverse reaction of Eqs. 1 and 3 (i.e., CO hydrogenation and Sabatier reaction) would proceed at the lower temperature zone downstream of the highest temperature point because it is thermodynamically favourable and can proceed at around 523–823K on Ni catalysts.[55–58] Moreover, the Ni-Lac sample showed lower catalytic activity than the other Ni samples in PTSRM despite the similar $T_{max.f}$ values (868–884 K, Figure 4.12). Based on the contribution of the kinetic factor to the reaction rate in TSRM at the low temperature of 723 K (Figure 4.13B), the low PTSRM activity of Ni-Lac would be due to the lowest Ni dispersion among the Ni/SiO_2 samples (Table 4.1).

The conversion-selectivity relationship (Figure 4.19) provided evidence of a side reaction in the lower temperature zone in PTSRM. Here, the author plotted the CO_2 selectivity (Eq. 6) against the CH_4 conversion with different spot sizes. In TSRM at various temperatures, CO_2 selectivity was almost on the line of the calculated results of the thermodynamic equilibrium. But, in the 2.0 cm spot size, the CO_2 selectivity for PTSRM was 87.3%, which is slightly higher than the line of the equilibrium. Moreover, the smaller spot sizes (i.e., Ø < 2.0 cm) at the high conversion ranges showed higher CO_2 selectivity than the results of activity tests in TSRM and thermodynamic calculations. The high CO_2 selectivity suggests that the WGS reaction (Eq. 2) and CO hydrogenation (reverse reaction of Eq. 1) occurred because these reactions increase CO_2 gas or decreases CO gas. It is known that both reactions are favoured thermodynamically at lower temperatures[55,59,60] and can proceed at lower temperatures (573–673 K)[55,61,62] on Ni/SiO_2 than those for SRM (Eq. 1)[7,8]. To confirm the effect, the author performed the thermal WGS and CO hydrogenation reactions on the Ni-Car sample (Figures 4.20 and 4.21) using conventional heating in the same experimental conditions as in the cases of the TSRM reaction except for the reactant gas. For WGS and CO hydrogenation, the reactant gases were 5%CO/12%H_2O/10%N_2/Ar(balance) and 5%CO/15%H_2/5%N_2/Ar(balance), respectively, and the total flow rate was fixed

to be 100 ml min^{-1}. After the hydrogen pretreatment at 873 K, the reactant gas was introduced to the reactor (the catalyst amount: 0.05 g) and the reaction temperature was increased from 473 K to 773 K. The outlet gas was analyzed 1 h after the objective temperatures were obtained. As the result, both reactions occurred at a low temperature of 573 K. Consequently, it is reasonable that the WGS reaction and/or CO hydrogenation in the lower temperature zone downstream (Figure 4.18C) contributes to the increased CO_2 selectivity in PTSRM. In the Ni/SiO_2 samples other than Ni-Car, the CO_2 selectivity in PTSRM at Ø = 2.0 cm was close to 100% (Ni-Ace: 97.4%, Ni-Nit: 97.8 %, Ni-Lac: 97.5%, after 120 min), which was much higher than that in Ni-Car (87.3%). In the thermal WGS and CO hydrogenation reactions at 573 K, Ni-Car showed the highest activity for WGS but showed the lower activity than Ni-Ace and Ni-Nit for CO hydrogenation (Figures 4.20 and 4.21). Thus, it is reasonable that CO was formed only on Ni-Car in PTSRM (Figure 4.12) because of the low CO consumption rate on Ni-Car by CO hydrogenation at the lower temperature zone below the center of the reactor. Note that the Ni-Lac sample showed lower CO hydrogenation rate than Ni-Car, but it has also lower activity for PTSRM. This might explain the no CO production on Ni-Lac in PTSRM. Furthermore, the author separately confirmed that WGS reaction is promoted by light irradiation under photothermal conditions at various light intensity i.e. 6.6–16 W and the spot size was 2 cm (Figure 4.22). Based on these results, the obtained insight shows that the product selectivity is controllable outside the steady-state thermodynamic values using the temperature gradient created by light in a single reactor system.

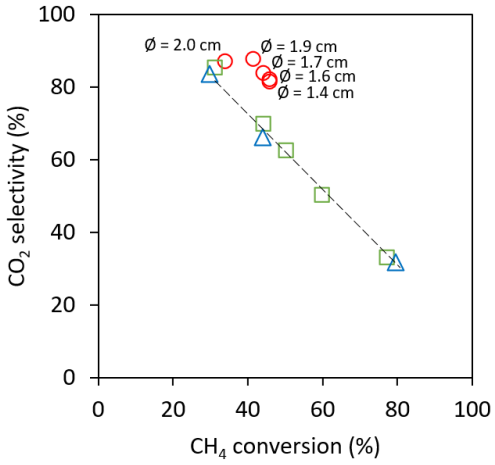

Figure 4.19 Relationship between the CH_4 conversion and CO_2 selectivity in PTSRM on the Ni-Car sample. Circles: PTSRM in various spot sizes; triangles: TSRM; squares: equilibrium.

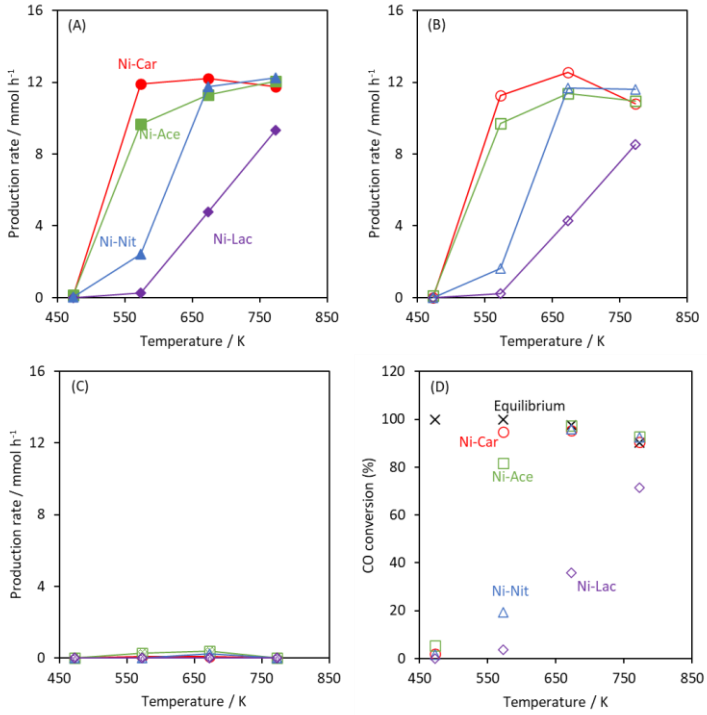

Figure 4.20 Production rates of H_2 (A), CO_2 (B), and CH_4 (C), and CO conversion (D) of the thermal WGS reaction over the Ni/SiO_2 samples at various temperatures. Reaction conditions; catalyst weight: 0.05 g, the total gas flow rate: 100 ml min^{-1}, reactant gas concentrations: 5%CO/15%H_2/5%N_2/Ar(balance).

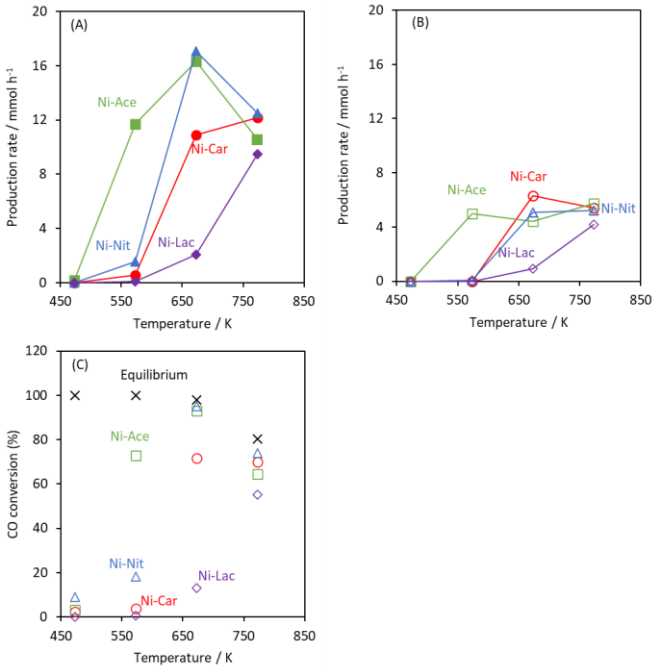

Figure 4.21 Production rates of CH_4 (A) and CO_2 (B) and CO conversion (C) of the thermal CO hydrogenation reaction over the Ni/SiO_2 samples at various temperatures. Reaction conditions; catalyst weight: 0.05 g, the total gas flow rate: 100 ml min^{-1}, reactant gas concentrations: 5%CO/15%H_2/5%N_2/Ar(balance).

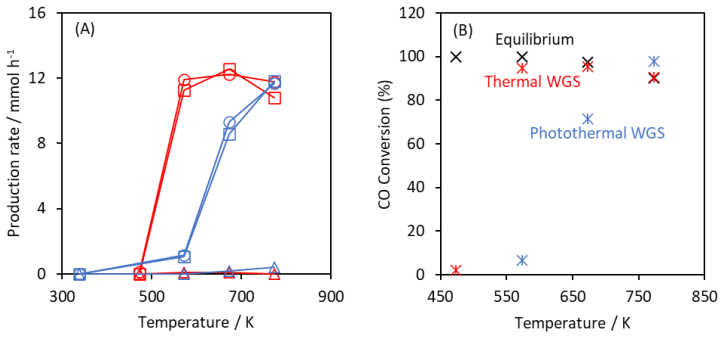

Figure 4.22 (A) Production rates of H_2 (open circle), CO_2 (open square), and CH_4 (open triangle), and (B) CO conversion in the thermal WGS (red) and photothermal WGS (blue) reactions over Ni-Car at various temperatures. Reaction conditions; catalyst weight: 0.05 g (thermal WGS) or 0.5 g (photothermal WGS), the total gas flow rate: 100 ml min^{-1}, reactant gas concentrations: 5%CO/12%H_2O/10%N_2/Ar(balance).

4.4. Conclusion

The author investigated the catalytic activity in PTSRM on four 20wt% Ni/SiO_2 catalysts with different sizes and morphologies of Ni particles, which were prepared by the decomposition of Ni PS and the impregnation method using different Ni precursors. In TSRM at 773 K in dark, the CH_4 conversion reached near-equilibrium in all the catalysts, meaning that the prepared catalysts have a sufficient reaction rate in dark condition to reach the thermodynamic equilibrium at that temperature. Under the light irradiation (23.8 W), there was no significant difference in the PTSRM activity for the Ni-Car, Ni-Nit, and Ni-Ace samples, while Ni-Lac showed the lowest activity due to the low Ni dispersion. Moreover, the power and spot size of light affected the reaction rate of PTSRM; as a tendency, higher $T_{max,f}$ contributed to the higher reaction rate in PTSRM. The author found that the CO_2 selectivity in PTSRM were affected by both WGS and CO hydrogenation and overcomes the values of experimental TSRM governed by thermodynamics. Based on these results of the activity test and temperature measurement, the author concluded that the significant temperature gradient (>240 K, Ø = 1.4 cm) formed by concentrated light irradiation is the origin of the characteristic selectivity that cannot be explained by steady-state thermodynamics. This work shows the possibility of controlling the product selectivity by the photo-formed temperature gradients for solar energy conversion to chemical energy.

References

1 S. Uemiya, N. Sato, H. Ando, T. Matsuda and E. Kikuchi, *Appl. Catal.*, 1990, **67**, 223–230.

2 E. Kikuchi, *Catal. Today*, 2000, **56**, 97–101.

3 J. Tong, Y. Matsumura, H. Suda and K. Haraya, *Ind. Eng. Chem. Res.*, 2005, **44**, 1454–1465.

4 C. S. Martavaltzi, E. P. Pampaka, E. S. Korkakaki and A. A. Lemonidou, *Energy Fuels*,

2010, **24**, 2589–2595.

5 X. Zhu, H. Wang, Y. Wei, K. Li and X. Cheng, *J. Rare Earths*, 2010, **28**, 907–913.

6 M. Dan, M. Mihet and M. D. Lazar, *Int. J. Hydrog. Energy*, 2020, **45**, 26254–26264.

7 J. R. Rostrup-Nielsen, L. J. Christiansen and J.-H. Bak Hansen, *Appl. Catal.*, 1988, **43**, 287–303.

8 Y. Matsumura and T. Nakamori, *Appl. Catal. Gen.*, 2004, **258**, 107–114.

9 F. Che, J. T. Gray, S. Ha and J.-S. McEwen, *ACS Catal.*, 2017, **7**, 551–562.

10 H. Song, X. Meng, Z. Wang, H. Liu and J. Ye, *Joule*, 2019, **3**, 1606–1636.

11 A. Giaconia, M. de Falco, G. Caputo, R. Grena, P. Tarquini and L. Marrelli, *AIChE J.*, 2008, **54**, 1932–1944.

12 M. Tutar, C. E. Üstün, J. M. Campillo-Robles, R. Fuente, S. Cibrián, I. Arzua, A. Fernández and G. A. López, *Comput. Chem. Eng.*, 2021, **155**, 107504.

13 R. D. Skocypec, R. E. Hogan and J. F. Muir, *Sol. Energy*, 1994, **52**, 479–490.

14 T. Shimizu, K. Shimizu, Y. Kitayama and T. Kodama, *Sol. Energy*, 2001, **71**, 315–324.

15 A. Berman, R. K. Karn and M. Epstein, *Green Chem.*, 2007, **9**, 626–631.

16 H. B. Do, J. T. Jang and G. Y. Han, *J. Sol. Energy Eng.*, 2012, **134**, 1–4.

17 T. Li, L. Tan, Y. Zhao and Y.-F. Song, *Chem. Eng. Sci.*, 2021, **245**, 116839.

18 P. Wang, X. Zhang, R. Shi, J. Zhao, Z. Yuan and T. Zhang, *Energy Fuels*, 2022, in press.

19 H. Yoshida, S. Kato, K. Hirao, J. Nishimoto and T. Hattori, *Chem. Lett.*, 2007, **36**, 430–431.

20 H. Yoshida, K. Hirao, J. Nishimoto, K. Shimura, S. Kato, H. Itoh and T. Hattori, *J. Phys. Chem. C*, 2008, **112**, 5542–5551.

21 K. Shimura, S. Kato, T. Yoshida, H. Itoh, T. Hattori and H. Yoshida, *J. Phys. Chem. C*, 2010, **114**, 3493–3503.

22 K. Shimura and H. Yoshida, *Energy Environ. Sci.*, 2010, **3**, 615–617.

23 K. Shimura, H. Kawai, T. Yoshida and H. Yoshida, *ACS Catal.*, 2012, **2**, 2126–2134.

24 A. Yamamoto, S. Mizuba, Y. Saeki and H. Yoshida, *Appl. Catal. Gen.*, 2016, **521**, 125–132.

25 H. Song, X. Meng, Z. Wang, Z. Wang, H. Chen, Y. Weng, F. Ichihara, M. Oshikiri, T. Kako and J. Ye, *ACS Catal.*, 2018, **8**, 7556–7565.

26 H. Yoshida, S. Mizuba and A. Yamamoto, *Catal. Today*, 2019, **334**, 30–36.

27 B. V. Ayodele, A. A. Ghazali, M. Y. Mohd Yassin and S. Abdullah, *Int. J. Hydrog. Energy*, 2019, **44**, 20700–20710.

28 B. Tan, Y. Ye, Z. Huang, L. Ye, M. Ma and Y. Zhou, *Chin. Chem. Lett.*, 2020, **31**, 1530–1534.

29 A. Anzai, K. Fujiwara, A. Yamamoto and H. Yoshida, *Catal. Today*, 2020, **352**, 1–9.

30 T. Kujirai, A. Yamaguchi, T. Fujita, H. Abe and M. Miyauchi, *Chem. Commun.*, 2021, **57**, 8007–8010.

31 W. Sarwana, A. Anzai, D. Takami, A. Yamamoto and H. Yoshida, *Catal. Sci. Technol.*, 2021, **11**, 5534–5542.

32 W. Sarwana, A. Yamamoto and H. Yoshida, *Catal. Today*, 2022, in press.

33 B. Han, W. Wei, M. Li, K. Sun and Y. H. Hu, *Chem. Commun.*, 2019, **55**, 7816–7819.

34 A. O. Govorov and H. H. Richardson, *Nano Today*, 2007, **2**, 30–38.

35 H. Huang, M. Mao, Q. Zhang, Y. Li, J. Bai, Y. Yang, M. Zeng and X. Zhao, *Adv. Energy Mater.*, 2018, **8**, 1702472.

36 D. Mateo, J. Luis Cerrillo, S. Durini and J. Gascon, *Chem. Soc. Rev.*, 2021, **50**, 2173–2210.

37 A. Loaiza-Gil, M. Villarroel, J. F. Balbuena, M. A. Lacruz and S. Gonzalez-Cortés, *J. Mol. Catal. Chem.*, 2008, **281**, 207–213.

38 A. J. Majewski, J. Wood and W. Bujalski, *Int. J. Hydrog. Energy*, 2013, **38**, 14531–14541.

39 C. Suo, Y. Liu, X. Zhang, H. Wang, B. Chen, J. Fang, Z. Zhang, R. Chen, R. Chen and C. Shi, *Eur. J. Inorg. Chem.*, 2022, **2022**, e202200182.

40 C. Mao, H. Li, H. Gu, J. Wang, Y. Zou, G. Qi, J. Xu, F. Deng, W. Shen, J. Li, S. Liu, J. Zhao and L. Zhang, *Chem*, 2019, **5**, 2702–2717.

41 X. Li, X. Zhang, H. O. Everitt and J. Liu, *Nano Lett.*, 2019, **19**, 1706–1711.

42 C. Zhang, H. Yue, Z. Huang, S. Li, G. Wu, X. Ma and J. Gong, *ACS Sustain. Chem. Eng.*, 2013, **1**, 161–173.

43 M. Yang, P. Jin, Y. Fan, C. Huang, N. Zhang, W. Weng, M. Chen and H. Wan, *Catal. Sci. Technol.*, 2015, **5**, 5095–5099.

44 R.-P. Ye, W. Gong, Z. Sun, Q. Sheng, X. Shi, T. Wang, Y. Yao, J. J. Razink, L. Lin, Z. Zhou, H. Adidharma, J. Tang, M. Fan and Y.-G. Yao, *Energy*, 2019, **188**, 116059.

45 H. Du, X. Ma, M. Jiang, P. Yan, Y. Zhao and Z. Conrad Zhang, *Catal. Today*, 2021, **365**, 265–273.

46 M. Mao, Q. Zhang, Y. Yang, Y. Li, H. Huang, Z. Jiang, Q. Hu and X. Zhao, *Green Chem.*, 2018, **20**, 2857–2869.

47 S. Gordon and B. J. Mcbride, 1994.

48 R. J. Matyi, L. H. Schwartz and J. B. Butt, *Catal. Rev.*, 1987, **29**, 41–99.

49 M. Takeuchi, G. Martra, S. Coluccia and M. Anpo, *J. Phys. Chem. B*, 2005, **109**, 7387–7391.

50 S. M. Williams, A. D. Stafford, K. R. Rodriguez, T. M. Rogers and J. V. Coe, *J. Phys. Chem. B*, 2003, **107**, 11871–11879.

51 D. A. Perry, R. L. Borchers, J. W. Golden, A. R. Owen, A. S. Price, W. A. Henry, F. Watanabe and A. S. Biris, *J. Phys. Chem. Lett.*, 2013, **4**, 3945–3949.

52 D. Takami, Y. Ito, S. Kawaharasaki, A. Yamamoto and H. Yoshida, *Sustain. Energy Fuels*, 2019, **3**, 2968–2971.

53 M. A. Rosen, *Int. J. Hydrog. Energy*, 1991, **16**, 207–217.

54 A. E. Lutz, R. W. Bradshaw, J. O. Keller and D. E. Witmer, *Int. J. Hydrog. Energy*, 2003, **28**, 159–167.

55 L. Xu, F. Wang, M. Chen, D. Nie, X. Lian, Z. Lu, H. Chen, K. Zhang and P. Ge, *Int. J. Hydrog. Energy*, 2017, **42**, 15523–15539.

56 D. Takami, A. Yamamoto and H. Yoshida, *Catal. Sci. Technol.*, 2020, **10**, 5811–5814.

57 Y. Chen, W. Bi, L. Chen and Q. Liu, *Int. J. Hydrog. Energy*, 2021, **46**, 27567–27575.

58 X. Cao, Y.-F. Han, C. Peng and M. Zhu, *ChemCatChem*, 2022, **14**, e202200190.

59 J. Ashok, M. L. Ang, P. Z. L. Terence and S. Kawi, *ChemCatChem*, 2016, **8**, 1308–1318.

5. General Conclusion

In this dissertation, the author has developed the reaction systems of the photocatalytic steam reforming of methane (PSRM) and the photothermal steam reforming of methane (PTSRM). By utilizing the UV irradiation under the mild conditions, the author attempted to obtain the different CO selectivity in the PSRM system and enhance the photocatalytic efficiency by using $NaTaO_3$:La and $Rh/K_2Ti_6O_{13}$ photocatalysts prepared by a flux method. Further, the catalytic activity of Ni/SiO_2 catalyst in the PTSRM system was investigated under a focused light irradiation including visible and near-infrared light.

In chapter 2, production of CO in the PSRM system was successfully achieved by employing a La-doped $NaTaO_3$ photocatalyst without a cocatalyst, where CO was a minor intermediate product with 24% selectivity. The produced CO was converted by water, that is the successive photocatalytic water gas shift reaction (PWGS), decreasing the CO production rate. The selectivity of CO in the PSRM system was controlled by the photocatalyst property and the reaction conditions such as the light intensity, the flow rate of the reactant, and the ratio of CH_4 to H_2O in the feed gas mixture to some extent. It was, however, realized that an excellent CO selectivity was not achieved by changing these parameters in the present ranges with the current photocatalyst and the reaction system. Thus, further investigation of the photocatalyst and the reactor would be desired for further improvement.

In chapter 3, many rod-like fine $K_2Ti_6O_{13}$ (KTO) crystals covered with facets having various structural aspects were successfully synthesized by employing a flux method. The photocatalytic activity of the Rh/KTO samples varied with the KTO structure. The KTO crystals with larger surface area exhibited higher photocatalytic activity for the PSRM in the present conditions. Other factors, such as crystal thickness, also influenced photocatalytic activity. Among them, the KTO(30,1173) sample prepared by rutile-TiO_2 precursor and KCl flux at 1173 K exhibited the highest photocatalytic activity after loading Rh cocatalyst. Furthermore, it was found that the granule of the Rh/KTO fine

crystal sample showed 2.1–2.6 times higher activity than the original powdery fine crystals, which would result from electron transfer between the KTO crystals with better intraparticle contact due to the pressing of the fine crystals to get the granule form. Further optimization of the cocatalyst and the loading method would contribute to the further development of the KTO photocatalyst.

In chapter 4, The author investigated the catalytic activity in PTSRM on four 20wt% Ni/SiO_2 catalysts with different sizes and morphologies of Ni particles, which were prepared by the decomposition of Ni PS and the impregnation method using different Ni precursors. In TSRM at 773 K in dark, the CH_4 conversion reached near-equilibrium in all the catalysts, meaning that the prepared catalysts have a sufficient reaction rate in dark condition to reach the thermodynamic equilibrium at that temperature. Under the light irradiation (23.8 W), there was no significant difference in the PTSRM activity for the Ni-Car, Ni-Nit, and Ni-Ace samples, while Ni-Lac showed the lowest activity due to the low Ni dispersion. Moreover, the power and spot size of light affected the reaction rate of PTSRM; as a tendency, higher $T_{max,f}$ contributed to the higher reaction rate in PTSRM. The author found that the CO_2 selectivity in PTSRM were affected by both WGS and CO hydrogenation and overcomes the values of experimental TSRM governed by thermodynamics. Based on these results of the activity test and temperature measurement, the author concluded that the significant temperature gradient (>240 K, Ø = 1.4 cm) formed by concentrated light irradiation is the origin of the characteristic selectivity that cannot be explained by steady-state thermodynamics. This work shows the possibility of controlling the product selectivity by the photo-formed temperature gradients for solar energy conversion to chemical energy.

In summary, the utilization of solar light to perform SRM reactions has been successfully developed in two ways, PSRM and PTSRM. In the former, the reaction selectivity was successfully controlled in a certain range and the effect of the crystal aspects of the photocatalyst was evaluated. The granulation effect was also revealed. In the latter, the attractive property of concentrated irradiation to change product selectivity was uncovered. Comparing these two systems, the current PSRM system is

obviously inferior to the present PTSRM system in product yield and selectivity. Insufficient production rates due to low photon absorption and high electron–hole recombination rates still become a barrier to developing the PSRM systems.

In current PSRM with powder photocatalyst, only the photocatalyst microcrystals located at the surface of the photocatalyst cell can receive the photoenergy and function as photocatalyst while the crystals at the back side of cell can not contribute to the SRM reaction. It was, however, revealed in this dissertation that the granulation of photocatalyst can provide the photoexcited carriers generated at the sunny side to the unirradiated dark side to increase the entire photocatalytic performance. This presents the possibility of further development of the PSRM with powdery photocatalyst. In another way, in the view of the efficient photoenergy utilization, the use of thin film the photocatalysts is considered alternative way for further development of the PSRM system.

On the other hand, in the PTSRM system, although the first photoactivation is also limited at the front catalysts at the irradiation surface, the thermal energy converted from the photoenergy can be easily transferred to all the catalysts in the inside parts. However, the higher temperature at the irradiated catalyst much contribute the entire conversion efficiency, which motivates the use of the concentrated light irradiation. The low concentration of photons in the sunlight must be considered. When compared in the same photoenergy from sunlight, the concentration limits the usable catalyst weight in the simple PTSRM system used in this dissertation. It was, however, found that the temperature graduation from the irradiated center in the concentrated light spot to the surrounds can contribute the change the reaction selectivity, which would open a new technology in the photothermal reaction systems.

If the serious barriers in the PSRM system mentioned above have been overcome, the room-temperature PSRM system would be a better system than the high-temperature PTSRM system. In the current state, however, the development of the photocatalytic system is still on the way. As a conclusion in this dissertation, the PTSRM system would be a better system to be further investigated intensely as a solar-light-

driven SRM system.

The author hope that these findings and suggestions obtained in this dissertation will significantly contribute to the development of both photocatalytic and photothermal systems for the steam reforming of methane reactions.

List of Publications

Chapter 2

Carbon monoxide as an intermediate product in the photocatalytic steam reforming of methane with lanthanum-doped sodium tantalate

Wirya Sarwana, Akihiko Anzai, Daichi Takami, Akira Yamamoto, and Hisao Yoshida

Catalysis Science & Technology, **2021**, *11*, 5534–5542.

Chapter 3

Granule of potassium hexatitanate fine crystals for photocatalytic steam reforming of methane

Wirya Sarwana, Akira Yamamoto, and Hisao Yoshida

Catalysis Today, **2022**, *in press*

DOI:10.1016/j.cattod.2022.07.026.

Chapter 4

Temperature-Graduated Nickel-Silica Catalysts for Photothermal Steam Reforming of Methane

Wirya Sarwana, Daichi Takami, Akira Yamamoto, and Hisao Yoshida

Catalysis Science & Technology, **2023**, DOI: 10.1039/D2CY01721K.